Angle-Resolved Photoemission Studies on Ruthenates and Iron-Based Superconductors

Author: Madhab Neupane

Boston College

The Graduate School of Arts and Sciences

Department of Physics

Angle-Resolved Photoemission Studies on Ruthenates and Iron-Based Superconductors

a dissertation

by

Madhab Neupane

submitted in partial fulfillment of the requirements

for the degree of

Doctor of Philosophy

December 15, 2010

Angle-Resolved Photoemission Studies on Ruthenates and Iron-Based Superconductors

Madhab Neupane

Dissertation advisors: Profs. Hong Ding and Ziqiang Wang

Abstract

Angle-resloved photoemission spectroscopy (ARPES) is a powerful technique to study the electronic structure in solids. Its unique ability of resolving the energy and momentum information of electrons inside a solid provides an essential tool in measuring the electronic structure of solids. ARPES has made great contributions in the understanding of correlated system such as high-T_c superconductors and ruthenates.

The Metal-insulator transition is a fundamental problem in condensed matter physics. The calcium substituted strontium ruthenate, $Ca_{2-x}Sr_xRuO_4$, provides a good platform to study the metal-insulator transition in multi-orbital systems. This system has a complex phase diagram that evolves from a p-wave superconductor to a Mott insulator. One of important projects of this thesis focuses on $Ca_{2-x}Sr_xRuO_4$.

The growing evidence for coexistence of itinerant electrons and local moments in transition metals with nearly degenerate d orbitals suggests that one or more electron orbitals undergo a Mott transition while the others remain itinerant. We have observed a novel orbital selective Mott transition (OSMT) in $Ca_{1.8}Sr_{0.2}RuO_4$ by ARPES. While we observed two sets of dispersing bands and Fermi surfaces (FSs) associated

with the doubly-degenerate d_{yz} and d_{zx} orbitals, the Fermi surface associated with the d_{xy} orbital which has a wider bandwidth is missing as a consequence of selective Mott localization. Our theoretical calculations have demonstrated that this unusual OSMT is mainly driven by the combined effects of inter-orbital carrier transfer, superlattice potentials and orbital degeneracy, whereas the bandwidth difference plays a less important role.

Another important project of this thesis focuses on the recently discovered iron-pnictides superconductors. The idea of inter-FS scattering associated with the near-nesting condition has been proposed to explain the superconductivity in the pnictides. The near-nesting condition varies upon the carrier doping which shifts the chemical potential. We have performed a systematic photoemission study of the chemical potential shift as a function of doping in a pnictide system based on $BaFe_2As_2$. The experimentally determined chemical potential shift is consistent with the prediction of a rigid band shift picture by the renormalized first-principle band calculations. This leads to an electron-hole asymmetry (EHA) due to different Fermi velocities for different FS sheets, which can be calculated from the Lindhard function of susceptibility. This built-in EHA from the band structure, which is fully consistent with the experimental phase diagram, strongly supports that inter-FS scattering over the near-nesting Fermi surfaces plays a vital role in the superconductivity of the iron pnictides.

To my wife Rusha Khanal and my daughter Melina Neupane.

Acknowledgments

First, I would like to thank Professor Hong Ding who has been my thesis supervisor and friend for the last six years. He has taught many experimental skills together with concepts of physics. With his enthusiasm, his inspiration, and his great efforts to explain things clearly and simply, he has made physics fun for me.

I would also like to thank Professor Ziqiang Wang who has been my thesis co-advisor over the last two years. His suggestions and theoretical guidance were always inspiring. Working under his advice is always efficient and productive.

I thank Dr. Peter Johnson for support, guidance and help during my stay at the National Synchrotron Light Source (NSLS), Brookhaven National Laboratory for one year. It was a great experience working with him and his group on an excellent APRES system at NSLS.

I also thank Professor Vidya Madhavan for many of her beneficial discussions and academic advices. The collaborations with her group have been very helpful.

I would like to thank Dr. Alexei V. Fedorov for his guidance and experimental assistances at the Advanced Light Source (ALS), Lawrence Berkeley National Labo-

ratory. I enjoyed very much working with him on his superior beamline at ALS.

I want to thank A. K. P. Shekaran, Hongbo Yang and Zhihui Pan, who have showed me how to conduct ARPES experiments and perform data analysis when I entered the group. I want to express my special thanka to Dr. Pierre Richard for his support and guidance on experiment and data analysis. I also want to thank my labmates Jihua Ma, Yiming Xu and Philopater Bishay for their supports and helps during experiments.

I want to thank many other faculty members and staffs in the Physics department. Their kindness to me has made my stay in Boston College a very pleasant and unforgettable experience.

I would like to thank Hongbo Yang, Tonica Valla, Tim Kidd and Jon Rameau for the warmhearted help during experiments at NSLS.

I thank R.Y. Jin and D. Mandrus from Oak Ridge National Laboratory for providing many excellent ruthenate samples, Haihu Wen and his group from the Institute of Physics (IOP) in China for proving many cuprate and pnictide samples, and Nanlin Wang and his group from IOP for their high-quality pnictide samples.

I thank all my friends here at Boston who are the sunshine of my life.

I thank my wife Rusha Khanal for the strength she gave to me, and my daughter Melina Neupane since she is a gift of love. To them I dedicate this thesis. At last, I want to thank my parents. They have encouraged and supported me throughout all stages of my life, and for that I am forever grateful.

Contents

Chapter 1

Introduction of ruthenates and iron-based superconductors

The most important advances in superconductivity research over the past two decades have been the discovery and study of superconductors in which strong electron interactions or electron correlations are important to their superconductivity. Examples includes heavy-fermion intermetallic compounds, organics, copper oxides (cuprates), ruthenates, cobaltes and iron-pnictides. Superconductivity research has thus become intimately related with the field of strongly correlated physics, and unconventional superconductivity has become one of the most actively studied topics of modern-day condensed-matter physics [1].

Supercondictivity involves the formation of a quantum condensate state by pairing conduction electrons. The condensation may be considered as a kind of Bose-Einstein

condensation because the pair of electrons are bosons. These boson are called as Cooper pairs and can be in the state of either total spin S =0 (spin singlet) or 1 (spin triplet). Because of the anticommuting properties of the electron as a fermion, the antisymmetric spin-singlet state is accompanied by a symmetric orbital wave function (even parity) with orbital angular momentum L =0 (s wave), 2 (d wave), etc. The symmetric spin-triplet state is accompanied by an antisymmetric orbital wave function (odd parity) with orbital angular momentum L =1 (p wave), 3 (f wave) etc.

This chapter presents an introduction of unconventional p-wave superconductor (Sr_2RuO_4) and newly discovered iron-based superconductors.

1.1 Sr_2RuO_4

Sr_2RuO_4 is believed to be a p-wave superconductor with spin triplet superconductivity. The following gives a brief introduction of Sr_2RuO_4.

1.1.1 Discovery and crystal structure

Discovery of Sr_2RuO_4 The discovery by Bednorz and Muller (1986) of high-temperature (high-T_c) superconductivity in copper oxides (cuprates) had a huge impact on the research of superconductivity. An important ingredient for a high-T_c is the existence of quasi-two dimensional electronic states arising from the planar CuO_2 network of the layered perovskite structure. A non-cuprate perovskite superconductor

is a good system to compare with cuprates to understand the mechanism of high T_c superconductivity. It is interesting to note that it took eight years until the first such noncuprate superconductor was finally found in a ruthenium oxides [2]. The superconducting transition temperature ($\sim$1.5 K) is much lower than that of cuprates. The parent compound of high-T_c cuprates are Mott insulators while Sr_2RuO_4 is metallic although isovalent compound Ca_2RuO_4 is a Mott insulator.

Structure of Sr_2RuO_4 Sr_2RuO_4 has the K_2NiF_4 structure, with $I4/mmm$ body-centered tetragonal space-group symmetry which is shown in Fig. 1.1. It is isotructure with the high-T_c $La_{2-x}Ba_xCuO_4$. The superconductivity is believed to occur in the metallic RuO_2 layer. A Ru ion with six neighboring oxygen form a RuO_6 octahedron. There is very little evidence for structural distortion in Sr_2RuO_4, and none for structural phase transitions between room temperature and 100 mK. The lattice parameters are $a = 0.3862$ and $c =$1.2722 nm.

Superconductivity of Sr_2RuO_4 The superconductivity of Sr_2RuO_4 was first discovered by resistivity and susceptibility measurement in 1994 [2]. Figure. 2 shows that $T_c = 0.9$ K from both resistivity and susceptibility measurements. The low value of T_c is due to impurities and defects of samples in early stage. High quality samples have T_c values around 1.5 K.

Evidence for p-wave superconductor There is increasing evidence that Sr_2RuO_4 is a p-wave superconductor. Both NMR Knight shift and spin polarized neutron scat-

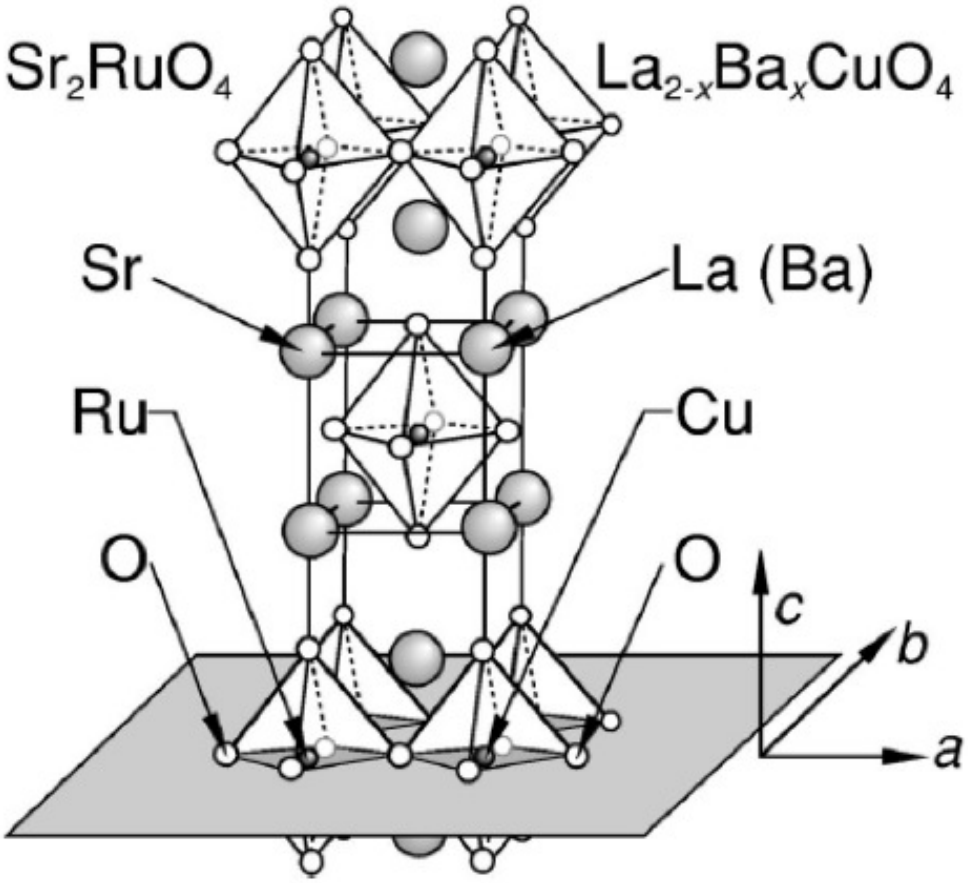

Figure 1.1: The layered perovskite structure common to ruthenate and cuprate superconductor [1].

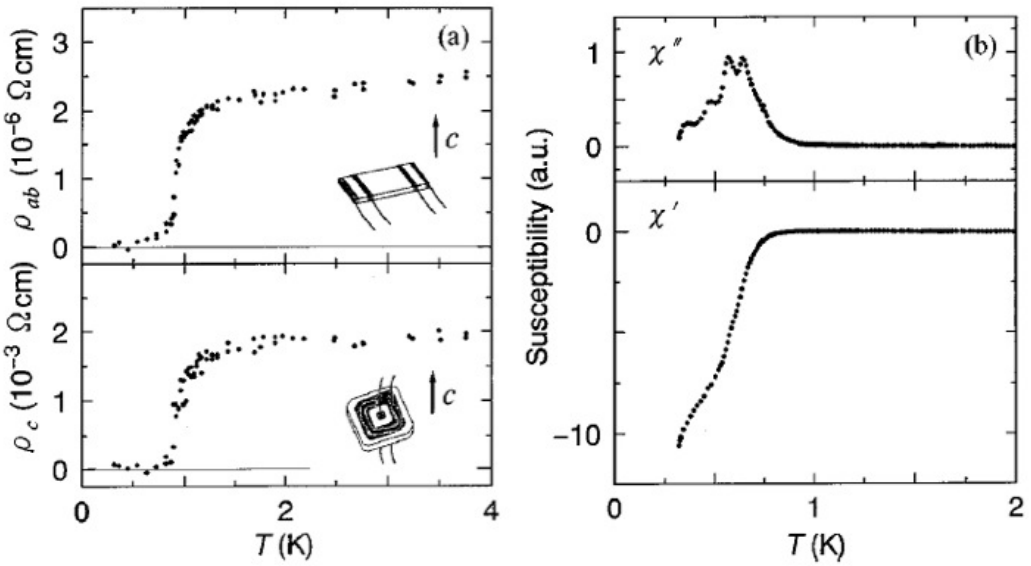

Figure 1.2: Resistivity and ac susceptibility of early crystals of Sr_2RuO_4. This data clearly show the superconducting transition [1].

tering experiment give experimental evidence for spin triplet pairing. In principle, the spin susceptibility can be measured without the influence of Meissner effect by NMR Knight shift. The Knight shift is the difference of the NMR frequency of a nucleus between normal and superconducting states. The Knight shift has been measured with dc field applied in the ab-plane by Ishida *et al.* [3] in high quality sample with T_c >1.4 K. The results of Knight shift measurement are shown in Fig. 1.3(c). It is well known that in a spin-singlet superconductor, there is a change of the Knight shift across T_c, while in a spin-triplet superconductor, the Knight shift does not change through T_c. The data shows that the Knight shift is temperature independent across T_c indicating strongly spin triplet pairing.

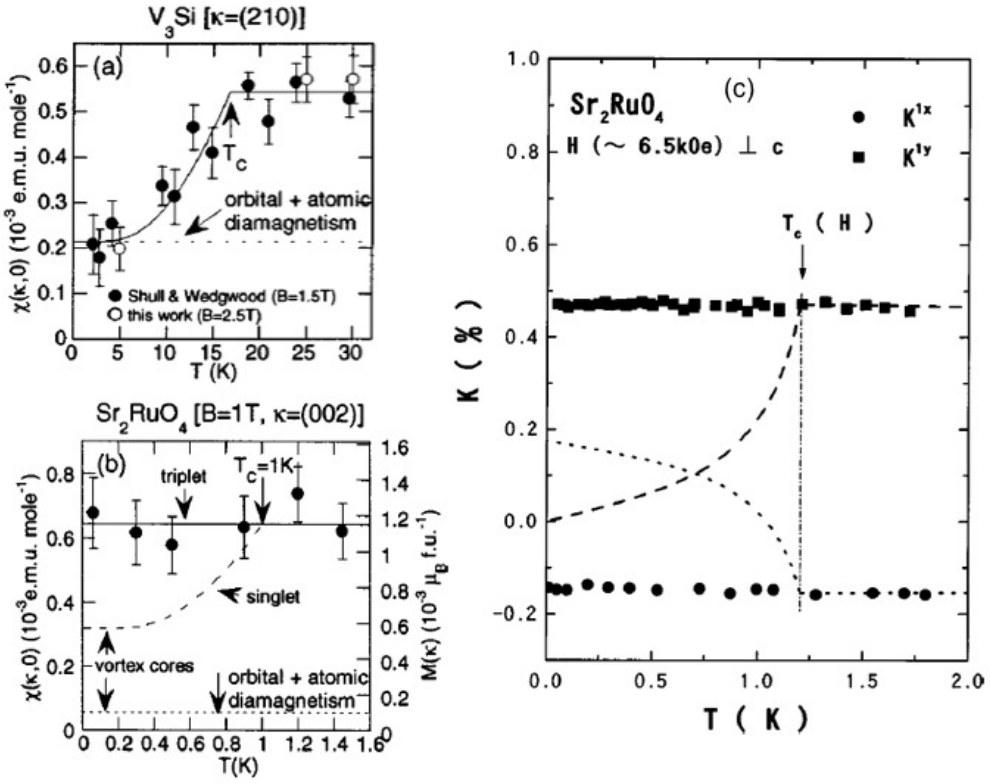

Figure 1.3: (a) Spin-polarized neutron-scattering results from an s-wave superconductor and (b) for Sr_2RuO_4 (c) The temperature dependence of Knight Shift (K) data [1].

Spin triplet can be also measured from spin polarized neutron scattering by measuring the spin susceptibility. The results are shown in Fig. 1.3(a) and 1.3(b). The s-wave spin-singlet superconductor V_3Si has a clear change of the spin susceptibility while no change of spin susceptibility has been observed in Sr_2RuO_4. This clearly indicates the presence of spin-triplet pairing in Sr_2RuO_4.

1.1.2 Normal-state properties of Sr_2RuO_4

The normal state properties of Sr_2RuO_4 are very interesting which shows the Fermi liquid behavior at low temperature. Both quantum oscillation and ARPES observe three Fermi surface sheets whose total volume is consistent with Luttinger theorem. The effective mass of the quasi-particle is highly enhanced compared to other metals, indicating strong interactions.

The resistivity is strongly anisotropic(as shown in Fig. 1.4), with low-temperature ratios varying between 400 and 4000. At high temperature, ρ_c (the interplane resistivity) decreases with increasing temperature, characteristic of an incoherent conduction mechanism. As the temperature is lowered, however, ρ_c goes through a broad maximum at approximately 130 K and then follows a metallic temperature dependence down to T_c. The in-plane resistivity, ρ_{ab}, is metallic from 300 K to low temperatures, and below approximately 20 K, both ρ_{ab} and ρ_c have an approximate T^2 dependence at low temperatures which is consistence with the predictions of the Fermi-liquid theory of metals.

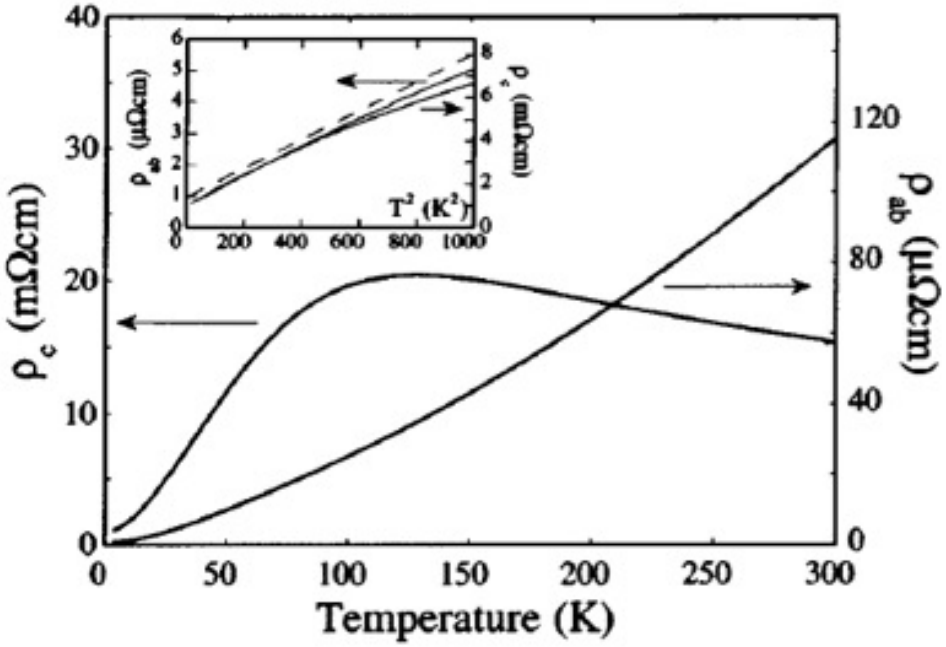

Figure 1.4: Anisotropic resistivity in Sr_2RuO_4 [4]. The dotted line in the inset shows the low-temperature T^2 dependence which is expected for a Fermi liquid behavior.

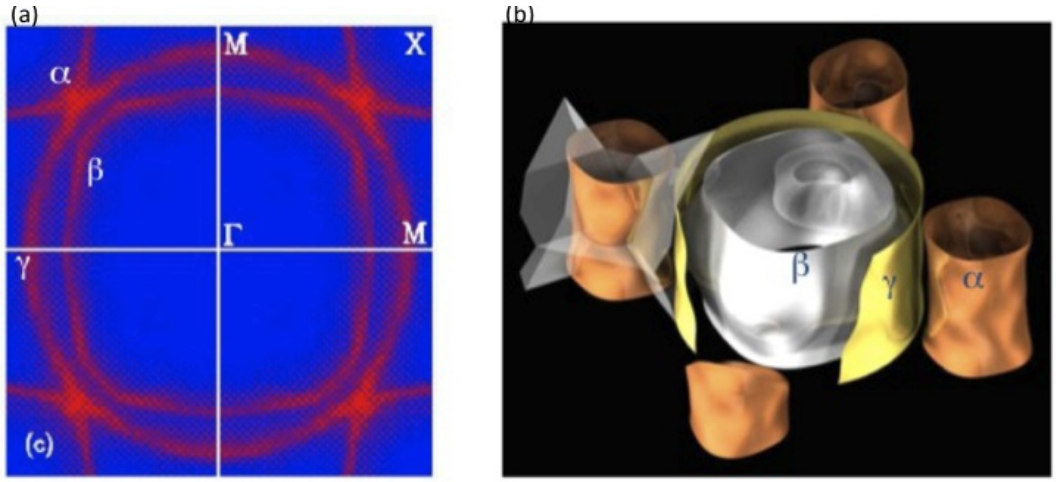

Figure 1.5: The Fermi surface obtained from (a) ARPES measurement [8] and, (b) quantum oscillation measurement [6].

The normal state specific heat of Sr_2RuO_4 measurement can be explained by Fermi liquid theory. The specific heat measurement is shown in Fig. 1.6(a) in which, below 15 K, C_p is modeled well by the expression $\gamma_{el}T+\beta_{ph}T^3$, with $\gamma_{el} = 38 \pm 2$ mJ/molK^2, and $\beta_{ph} = 0.2 \pm 0.005$ mJ/molK^4. No change is seen in either value within experimental errors in an applied magnetic field of 14 T.

The typical results for the normal-state static susceptibility χ of Sr_2RuO_4 are shown in Fig. 1.6(b). This data indicates the spin or Pauli term comes from the striking isotropy of χ in the presence of a very anisotropic electronic structure.

We can summarize the properties of Sr_2RuO_4 as follows:

(i) The superconductivity of Sr_2RuO_4 condenses from a metallic state that is a strongly two-dimentional Fermi liquid.

(ii) The Fermi surface consists of three weakly corrugated cylindrical sheets, α

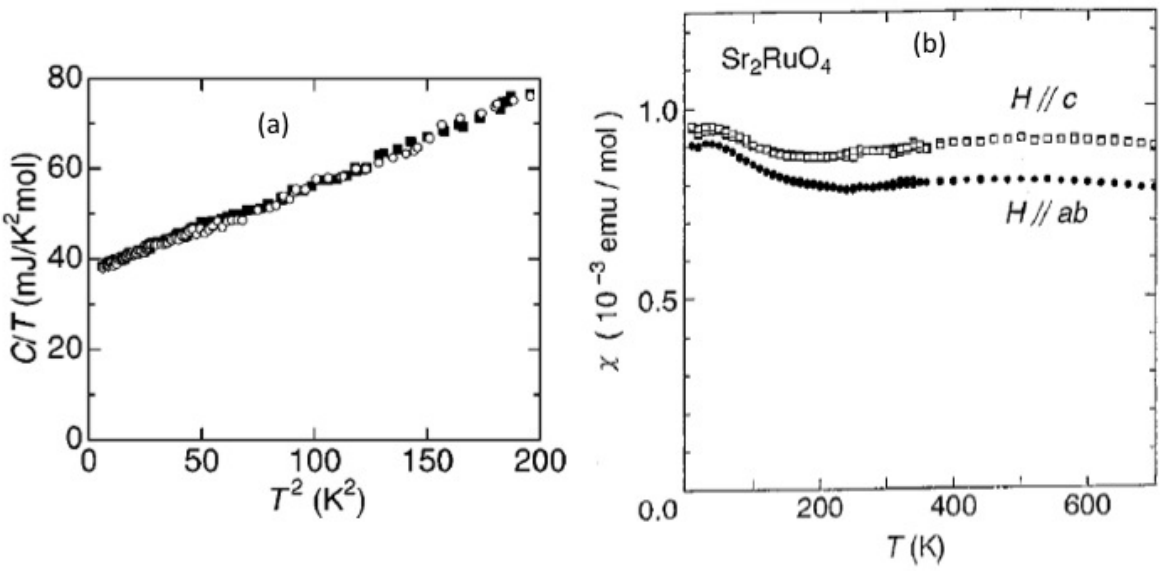

Figure 1.6: (a) The total specific heat of Sr_2RuO_4 divided by temperature between T_c and 14 K in zero field (filled squares) and an applied magnetic fields of 14 T (open circles) applied parallel to c axis. (b) The static susceptibility of Sr_2RuO_4 for fields of 1 T applied parallel to the ab plane and the c axis [1].

(which is holelike), and β and γ (which are electronlike). It is shown in Fig. 1.5.

(iii) There is a significant quasiparticle mass enhancement.

(iv) Although the dynamical susceptibility is enhanced at $q = 0$, the largest peak, due to Fermi-surface nesting, is at $(0.6\pi, 0.6\pi)$.

Table 1.1 presents a comparison between cuprates and ruthenates.

Cuprates	Ruthenates
$T_C \approx$160 K	$T_C \approx 1$ K
Cu $3d^9$ configuration	Ru $4d^4$ configuration
Single band near E_F	Multiple bands near E_F
Cu $3d_{x^2-y^2}$ - O $2p$ orbital near E_F	Ru $4d_{xy,yz,zx}$ - O $2p$ orbitals near E_F
Parent compound is Mott insulator	Parent compound is a conductor
d-wave order parameter	p-wave symmetry
With antiferromagnetic ordering	With ferromagnetic correlation

Table 1.1: Comparison between cuprates and ruthenates

1.2 Iron-based superconductor

The discovery of the iron-based layered superconductor LaFeAs($O_{1-x}F_x$) reported by Hosono group [7] on February 23, 2008, had a great impact on researchers in condensed-matter physics because it provided a new opportunity to investigate the mechanism of non-BCS exotic superconductors. It is also interesting because the

compound $LaFeAs(O_{0.89}F_{0.11})$, which contains one of the most familiar ferromagnetic atom *iron*, shows superconductivity at $\sim$ 26 K. After this discovery, a tremendous number of iron-based superconductors have been discovered. Generally, iron-based superconductors can be classified as REFeAs$(O_{1-x}F_x)$ (RE = Ce, Pr, Sm, Nd *etc*) called 1111 systems, REFe$_2$As$_2$ (RE= Ca, Sr, Ba, Eu) called as 122 systems, AFeAs (A = Li, Na) called 111, and FeCh (Ch = chalcogens) called 11 systems.

The superconducting state can be induced either by electron or hole doping of the parent compounds or also by pressure. Until now, the highest T_c attained is 57.4 K in the electron doped $Ca_{0.4}Na_{0.6}FeAsF$ (1111 compound) [8], while for 122 family the highest T_c of 38 K is reached in the hole doped $Ba_{0.6}K_{0.4}Fe_2As_2$ [9]. It seems that the FeAs layers are responsible for superconductivity in these compounds because the electronic states near the Fermi surface are dominated by contributions from Fe and As. Extensive studies of phonon dynamics [10, 11] suggest that it is unlikely that the superconductivity in iron pnictides is due to simple electron-phonon coupling. Since phonons play no significant role in the superconducting pair formation, it is natural to presume that magnetism has a crucial role in the appearance of superconductivity and consequently antiferromagnetic (AFM) spin fluctuations have been suggested as a possible pairing mechanism. Several neutron diffraction experiments reveal that the common feature of all the iron pnictide parent compounds is a spin density wave (SDW) arising from long range AFM order of the Fe moments at low temperature.

We mainly focus on the 122 and 11 systems in this thesis.

1.2.1 Crystal structure and physical properties

Crystal structure

1111: LaOFeAs (1111) crystalizes in a square lattice with Fe layers sandwiched by two As layers (up and down), each Fe is coordinated by a As tetrahedron. Its electronic properties are dominated by the (FeAs)-triple-layers, which contribute mostly to the electronic states around the Fermi level (E_F). The 1111 family of iron pnictides crystallizes in the ZrCuSiAs-type structure (space group P4/nmm). In this structure, two-dimensional layers of edge-sharing $FeAs_{4/4}$ tetrahedra alternate with sheets of edge-sharing $OLa_{4/4}$ tetrahedra as shown in Fig. 1.7(a).

122: The 122 system which has a tetragonal $ThCr_2Si_2$-type structure of I4/nmm space group contains practically identical edge-sharing $FeAs_{4/4}$ tetrahedra, but they are separated by RE (RE = Ca, Sr, Ba, Eu) atoms. This structure is shown in Fig. 1.7 (b).

111: 111 systems crystallize into a Cu_2Sb-type tetragonal structure containing [FeAs] layer with an average iron valency of 2+ like for 1111 and the 122 parent compound.

11: The PbO-type α-FeSe crystal structure is shown in Fig. 1.7 (d). It has the planar crystal sublattice consisting of edge sharing $FeSe_4$ tetrahedra, the same as the $FeAs_4$ tetrahedra layers found in oxypnictides.

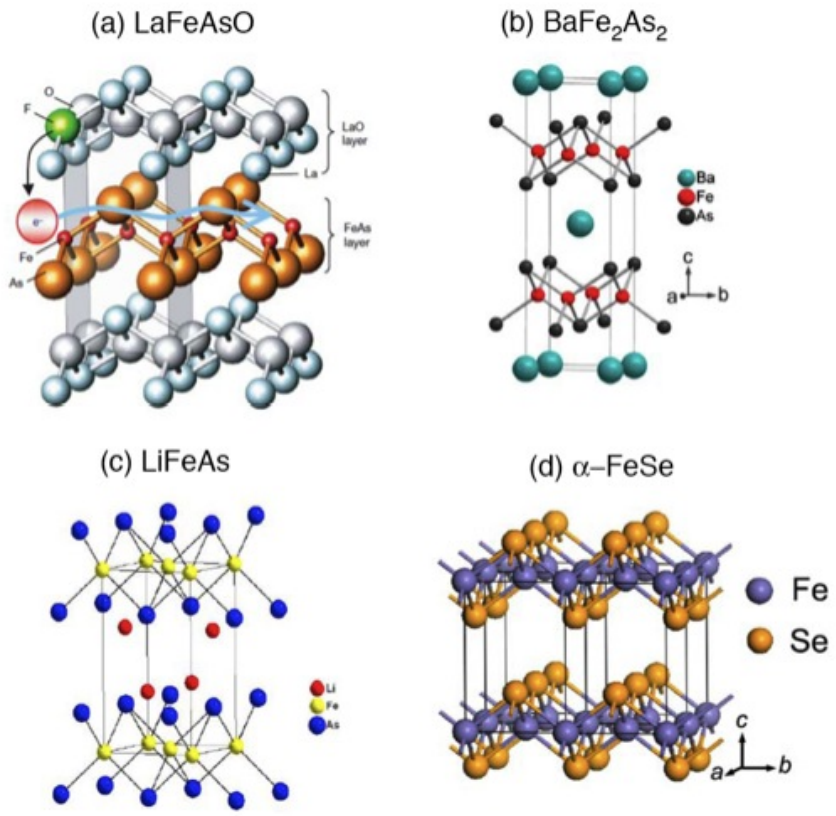

Figure 1.7: Schematic crystal structure of (a) LaFeAsO [12] (b) $BaFe_2As_2$ [9] (c) LiFeAs [13] (d) α-FeSe [14]. Each of these structures contains a square lattice of Fe atoms at high temperatures that can distort at low temperatures. Each Fe atom is tetrahedrally coordinated by As (a, b, c) or Se (d).

Physical properties The following shows the physical properties of iron-based superconductors:

Resistivity Parent compounds of iron-pnictide show an anomaly in the resistivity at a certain temperature depending upon the compound. It is pointed out that this anomaly is due to a structural phase transition. Typical examples of resistivity curves for 1111 and 122 system are shown in Fig. 1.8.

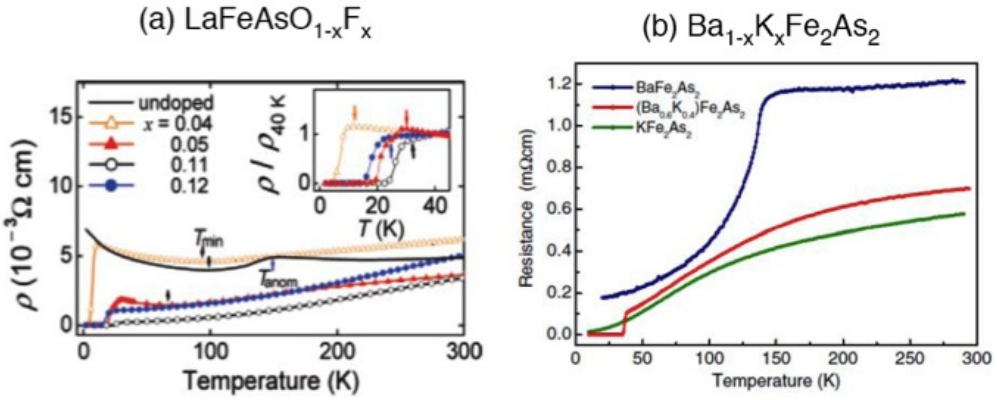

Figure 1.8: Typical resistivity of (a) $LaFeAsO_{1-x}F_x$ [7]. (b) (Ba,K)Fe_2As_2 [9].

Upper critical field Fig 1.9 shows a weak isotropy in the upper critical field H_{c2} of hole (K) and electron (Co) doped $BaFe_2As_2$. The nearly isotropic temperature dependence of the H_{c2} values at low temperatures was attributed to a 3D Fermi surfaces (FSs) in these compounds which is confirmed in the 122 systems by ARPES. This is in contrast with the quasi-two- dimensional electronic structure and large anisotropy of the cuprates.

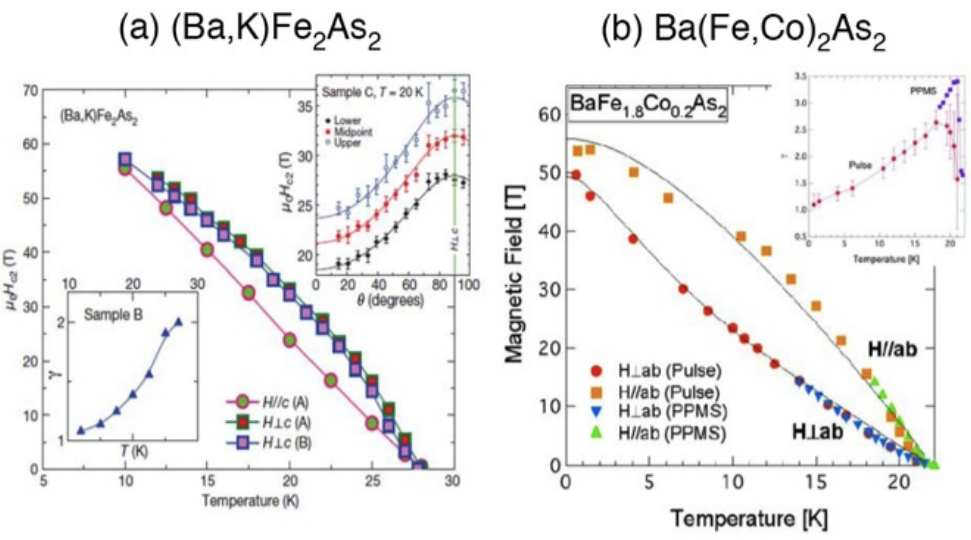

Figure 1.9: The weak anisotropy in the upper critical field H_{c2} [15]. (a) (Ba, K)Fe_2As_2 (b) $Ba(Co,Fe)_2As_2$ [16].

Antiferromagnetic Order Since superconductivity in iron pnictides appears by doping their parent compounds with charge carriers or using pressure, it is natural to ask what is the ground state of the parent compound? Also, an anomaly in the resistivity of the parent compounds of these materials occurs below a certain temperature (in case of LaFeAsO, it is at $\sim$ 150 K) in addition to a small anomaly in the d. c. magnetic susceptibility. Optical conductivity and theoretical calculations suggest that LaFeAsO exhibits a spin-density-wave (SDW) instability that is suppressed by doping with electrons to induce superconductivity.

The first direct evidence of SDW order in LaFeAsO came from neutron-scattering experiments by de la Cruz *et al.* [17]. They showed that LaFeAsO undergoes an abrupt structural distortion below $\sim$ 155 K, changing the symmetry from tetragonal

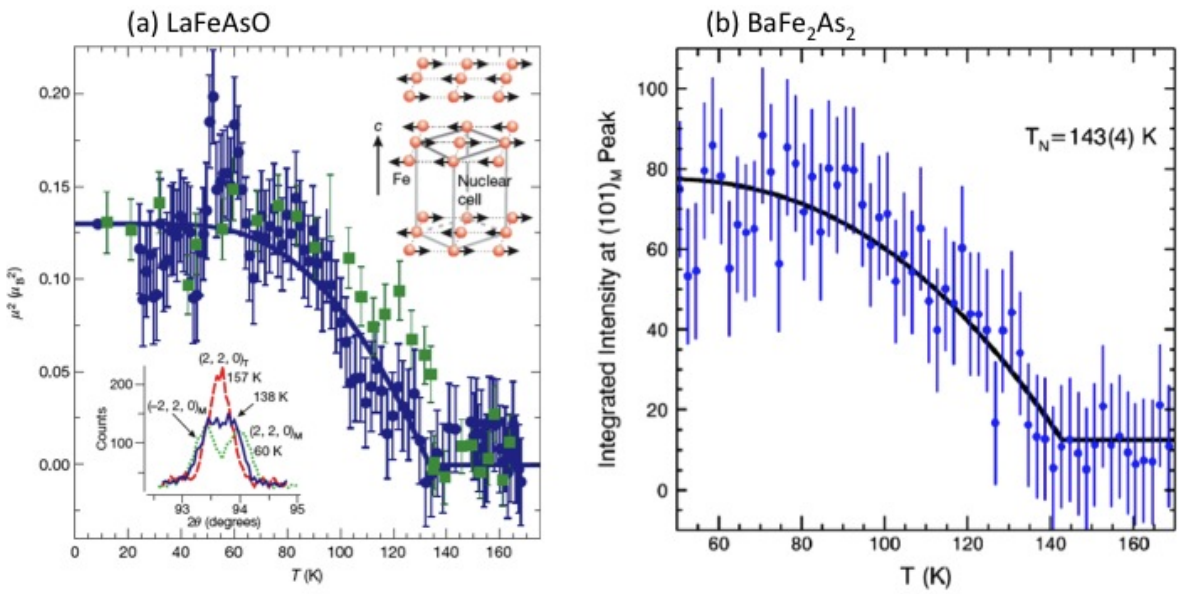

Figure 1.10: Antiferromagnetic ordering in (a) LaFeAsO [17] and (b) $BaFe_2As_2$ [18]

(space group P4/nmm) to monoclinic (space group P112/n) at low temperatures, followed by a long-range SDW-type antiferromagnetic (AFM) order with a small moment but simple magnetic structure developing below $\sim$ 137 K. The magnetic structure is consistent with theoretical predictions, but the moment of 0.365 μ_B per iron atom obtained here at 8 K is much smaller than the predicted values of $\sim$ 2.3 μ_B per iron atom. Later the AFM order in $BaFe_2As_2$ was also observed by a neutron diffraction study [18]. Similarly to the 1111 system, $BaFe_2As_2$ shows tetragonal to orthorombic structural and magnetic transitions. But the important things is that both transitions occur simultaneously at the same temperature. These results are summarized in Fig. 1.10.

1.2.2 Electronic structure

The study of the electronic structure shows that the Fermi surface and band structures of the different families of pnictides are rather generally similar. Although the field is very recent and thus most need to be determined experimentally, one can draw a few broad conclusions from the ARPES point of view that seem to hold for all these systems:

1. Every systems show non-negligible renormalization effects due to electronic correlations.

2. All systems exhibit a complex multi-sheet Fermi surface with holelike pockets at the Brillouin zone center (Γ point) and electronlike pockets at the zone corner (M point).

3. The superconducting gap size indicates a strong coupling regime and is Fermi surface-sheet dependent.

4. The superconducting gaps are isotropic along each Fermi surface sheet.

5. The superconducting gap size seems related to the nesting of Γ-centered holelike Fermi surface pockets with M-centered electronlike Fermi surface pockets, which are connected by the antiferromagnetic wavevector.

However, apart from the common general features in their electronic structures, many differences may exist among the different families and even in the same family as well.

$BaFe_2As_2$ D. J. Singh [19] performed band structure calculations taking experimental tetragonal lattice parameters at room temperature and relaxing the internal co-ordinate of *As* using LDA total-energy minimization. The results using experimental *As* co-ordiantes are shown for the purpose of comparison.

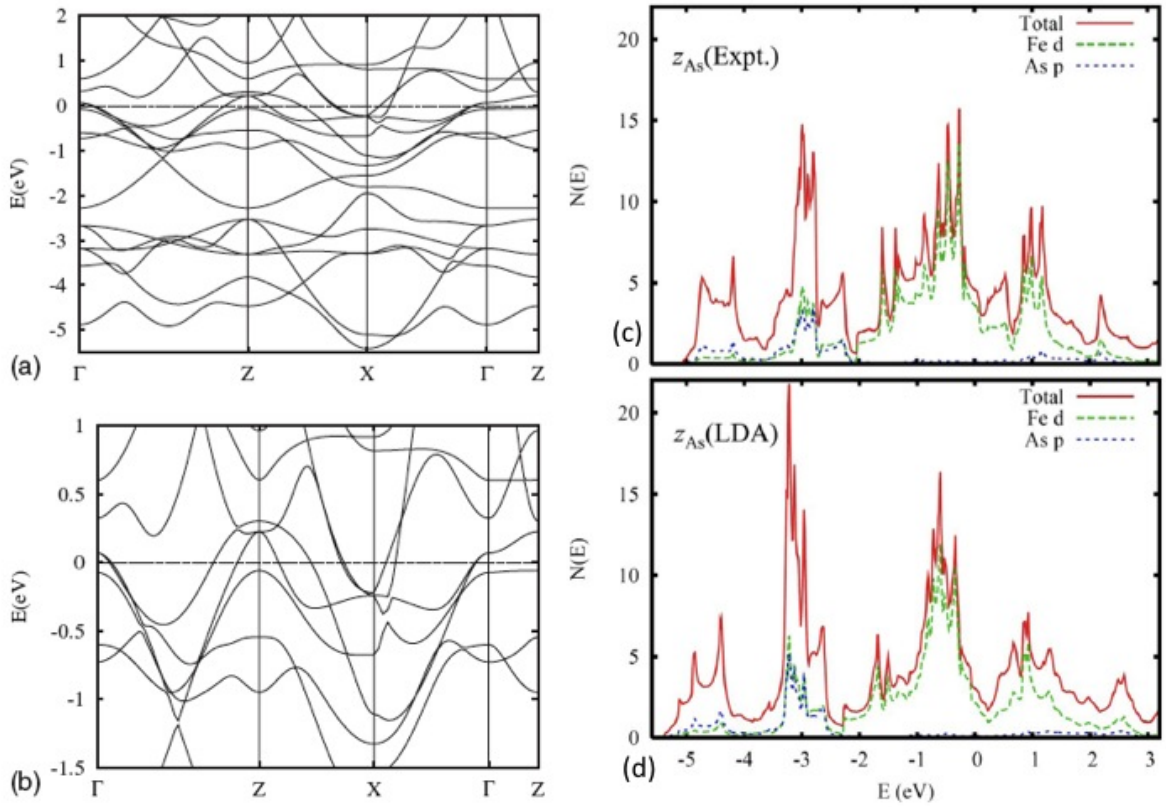

Figure 1.11: (a) Calculated band structure of $BaFe_2As_2$ for LDA values of z_{As}. (b) This panel shows a zoom in near E_F (c) Calculated electron density of states of $BaFe_2As_2$ for experimental and (b) LDA (bottom) values of z_{As} [19]

The calculated LDA band structures and electronic density of states (DOS) are

shown in Figs 1.11. There is a high density of states near E_F which is due to the contribution of Fe $3d$ states. The corresponding Fermi surfaces are shown in Fig. 1.12. Hole like Fermi surface sheets appear at the Brillouin zone (BZ) center (called Γ point) and electron-like FS sheets appear at the BZ corners (called M point). The hole-like FS at the BZ center flares out at $k_z = 1/2$ (Z point), giving a three-dimentional nature to the Fermi surface. However, this flaring out is sensitive to the As height z_{As}. In particular, it is reduced as As is moved away from the Fe plane. This is mainly observed using the experimental value of As internal coordinate $z_{As} = 0.3545$ rather than the LDA-calculated value of $z_{As} = 0.342$.

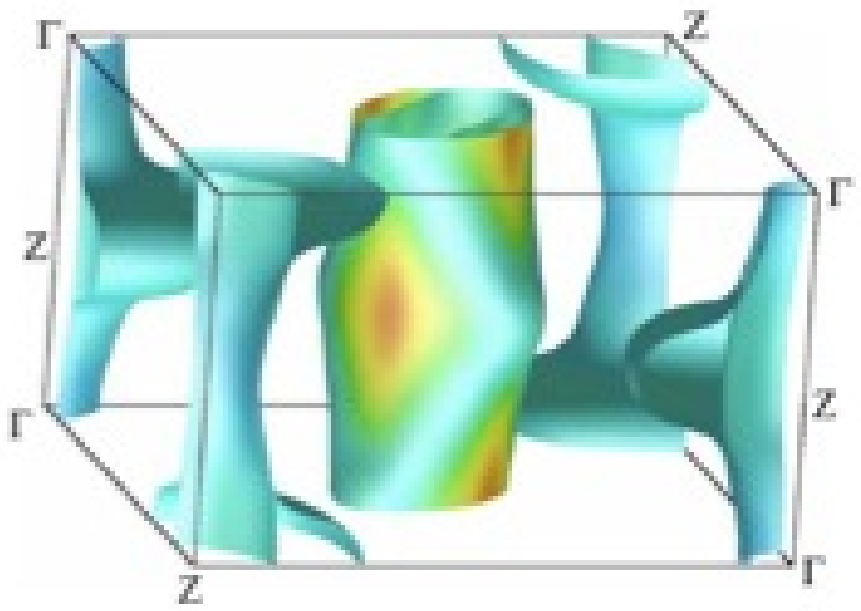

Figure 1.12: LDA Fermi surfaces of $BaFe_2As_2$ for LDA internal coordinates [19].

The sensitivity of these calculations to the As potition appears in the DOS near

E_F. By comparing the upper panel (c) [z_{As} (expt)] and lower panel (d) [z_{As} (LDA)] of Fig. 1.11, we notice that the DOS N(E_F.) is larger when the As height is raised to the experimental value leading to a more magnetic state.

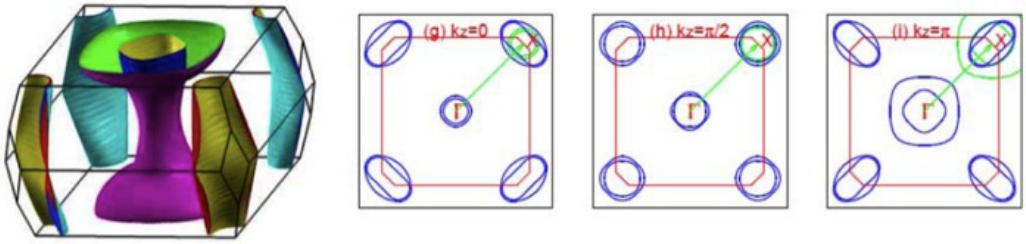

Figure 1.13: Calculated Fermi surface of $BaFe_2As_2$ [20].

Fig. 1.13 shows the calculated electronic structure of $BaFe_2As_2$ taken from another reference [25]. These results show good agreement with those shown above but this calculation focuses on the three-dimentional electronic structure observed in $BaFe_2As_2$. Fig. 1.13 shows that for the $k_z = 0$ ($k_z = \pi$) plane, the size of the hole pockets is smaller (larger) than the electron pockets, and only for the $k_z = \pi/2$ plane, the size of the two is almost equal. This suggests enhanced three dimensionality in the electronic structure of $BaFe_2As_2$.

The band structures and Fermi surfaces of the 11-type $Fe_{1+y}Te_{1-x}Se_x$ compounds calculated using LDA are similar to those of the 122 and 1111-type compounds [21].

Experimental observation: Ref. [22] shows the direct observation of inner (called α) and outer (called β) hole Fermi surfaces at the zone center (Γ point) and electron

(called γ) like Fermi surface at the zone corner (M point) of $Ba_{0.6}K_{0.4}Fe_2As_2$ using angle-resolved photoemission spectroscopy. They have observed two superconducting gaps with different values: a large gap around 12 meV on the α and γ Fermi surfaces and a small gap around 6 meV on the β Fermi surface. It is also important to note that the gaps are nodeless and nearly isotropic around their respective FS sheets as shown in Fig. 1.14. The pairing between α and γ bands which are connected by the (π, 0) spin-density wave vector, strongly suggests that the pairing mechanism originates from the inter-band interactions between these two nested FS sheets.

Although Fe-based superconductors were discovered just around 2 years ago, this allows a new path to study a high T_c superconductor. Though the study of iron-based superconductors is in early states, rapid research works on theoretical and experimental fonts have been performed. It is important to point out the similarities and differences between cuprates and pnictides, which are given below:

Similarities between cuprates and pnictides

- Superconductivity with T_c exceeding 50 K
- Layered structures
- Magnetically ordered parent compounds
- Doping induces superconductivity
- Similar phase diagrams
- Magnetic resonances in the SC state

Differences between cuprates and pnictides

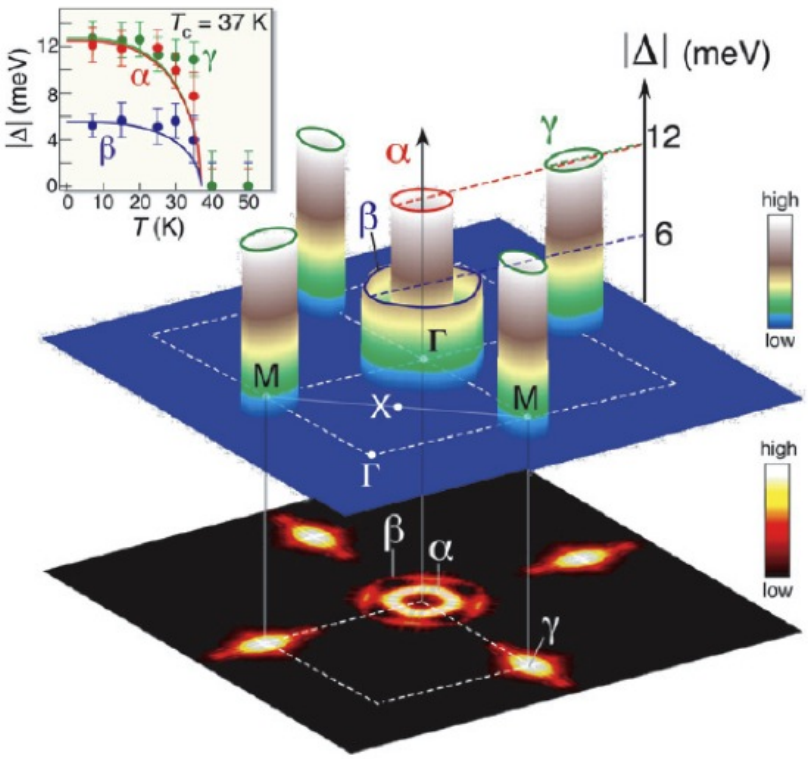

Figure 1.14: Three-dimensional plot of the superconducting gap size in $Ba_{0.6}K_{0.4}Fe_2As_2$ on three observed Fermi surface sheets and their temperature evolution (inset) [22].

Cuprates	Pnictides
Spin 1/2	Spin 1
Single d-orbital	Multiple d-orbitals
Mott Insulator parent compound	Semimetal parent compound
Magnetism near (π, π)	Magnetism is at $(\pi, 0)$.
d-wave (nodal quasiparticles)	No nodal quasiparticles

Bibliography

[1] A. P. Mackenzie and Y. Maeno, Rev. Mod. Phys. **75**, 657 (2003).

[2] Y. Maeno *et al.*, Nature (London) **372**, 532 (1994).

[3] K. Ishida *et al.*, Nature (London) **396**, 658 (1998).

[4] N. E. Hussey *et al.*, Phys. Rev. B **57**, 5505 (1998).

[5] A. Damascelli *et al.*, Phys. Rev. Lett. **85**, 5194 (2000).

[6] C. Bergemann *et al.*, Phys. Rev. Lett. **84**, 2662 (2000).

[7] Y. Kamihara *et al.*, J. Am. Chem. Soc. **103**, 3296 (2008).

[8] P. Cheng *et al.*, Euro. phys. Lett. **85**, 67003 (2009).

[9] M. Rotter *et al.*, Phys. Rev. Lett. **101**, 107006 (2008).

[10] R. Mittal *et al.*, Phys. Rev. B **78**, 104514 (2008).

[11] R. Mittal *et al.*, Phys. Rev. B **78**, 224518 (2008).

[12] H. Takahashi *et al.*, Nature (London) **453**, 376 (2008).

[13] X. C. Wang *et al.*, Solid State Communication **148**, 538 (2008).

[14] F.-C. Hsu *et al.*, Proc. Natl. Acad. Sci. USA **105**, 14262 (2008).

[15] H. Q. Yuan *et al.*, Nature (London) **457**, 565 (2009).

[16] M. Kano *et al.*, J. Phys. Soc. Jpn **78**, 084719 (2009).

[17] C. de. la Cruz *et al.*, Nature **453**, 899 (2008).

[18] Q. Huang *et al.*, Phys. Rev. Lett. **101**, 257003 (2008).

[19] D. J. Singh, Phys. Rev.B **78**, 094511 (2008).

[20] G. Xu *et al.*, Euro. phys. Lett. **84**, 67015 (2008).

[21] A. Subedi, Phys. Rev.B **78**, 134514 (2008).

[22] H. Ding *et al.*, Euro. phys. Lett. **83**, 47001 (2008).

Chapter 2

Angle resolved photoemission spectroscopy (ARPES)

2.1 Photoemission spectroscopy

2.1.1 History and fundamentals of photoemission

Photoemission spectroscopy is a general term which refers to all techniques based on the photoelectric effect originally observed by Hertz [1]. In 1887, Heinrich Hertz observed, even before the discovery of electron, that a sparkle between two electrodes was more easily observed if the electrodes were illuminated. This was later explained as a manifestation of the quantum nature of light by Einstein (1905) [2]. The modern era of photoemission spectroscopy started in 1964 with the papers of Berglund and Spicer. The first paper of Berglung and Spicer worked out what is called the three-

step model for photo-emission, and the second one applied it to data on Cu and Ag. At the same time, there were two papers by Gobeli *et al.* and Kane (1964), nearly simultaneously, with wide spread calculations of accurate electronic structure of many materials.

Photoemission spectroscopy (PES) can be categorized into two major sub-fields according to the energy of the incident photons used:

(1) X-ray photoemission spectroscopy (XPS), also known as ESCA- Electron Spectroscopy for Chemical Analysis, uses X-rays to study core level electrons. XPS has been widely used in physics, chemistry, biology and material science.

(2) Ultraviolet photoemission spectroscopy (UPS) uses ultraviolet photons to study valence electrons.

In most photoemission studies, the kinetic energy of emitted electrons is measured. The independent-electron model is adopted for the description of the electrons in a solid before and after the emission of the electrons. The measured kinetic energy, E_{kin}, and the work function, ϕ (typically 4-5 eV for metals), give the information of the final energy E_f after the emission inside the sample. Then E_i, the initial energy before the emission, can be derived. The spectrum resembles the density of occupied electron states weighted by a smooth function that varies smoothly with energy. If an electron energy analyzer accepts electrons within only small solid angle, the angular dependence of measured spectra can be treated as well, leading to spectra of E_i vs the wave vector of the initial state. This can be compared to the calculated band

structure. High resolution ARPES spectra can be obtained by the recent improvement of high-resolution detector and photon sources.

The schematic drawing of the energetics of the photoemission process is shown in Figs. 1 and 2. A monochromatic light shines on a well prepared sample surface. Then, based on the photoelectric effect, electrons in the material absorbing photons are excited to higher energy, some of them escape out from the sample into vacuum. An electron energy analyzer collects the outgoing electrons at a certain finite solid angle (θ, ϕ), as a function of electron's kinetic energy. In the angle-integrated mode, in which electrons are collected from all the directions, the electron density of states are measured. An ARPES spectrum has a direct relation with the electron's distribution inside the material, plus the broadening of energy levels due to resolution of the detecting process. By changing (θ, ϕ), one can obtain the angular dependence of band information of a single crystal sample and compare it to band calculations.

Only photoelectrons close to the samples' surface (topmost layers) can escape to the vacuum due to scattering of electron with the environment, such as electrons, ions, photons, plasmons etc... The typical escape lenght for photoelectrons created by 20 -100 eV photon energy is about 5 Å. Therefore, in order to learn about the bulk electronic structure, photoemission spectroscopy experiments have to be performed on atomically clean and well-ordered systems, which implies that fresh and flat surfaces have to be prepared immediately prior to the experiment in ultrahigh-vacuum conditions. The typical pressure for PES experiment is about 10^{-10} to 10^{-11} Torr,

and a sample's life time is from a few hours to a few days.

When light impinges on a solid, an electron in the solid can absorb a photon and be excited into an unoccupied state. If the photon energy is high enough, the electron will get out of the surface and go into vacuum. This photoelectric phenomenon was first discovered by Hertz in 1887 [1], which was explained later by A. Einstein in 1905 [2] with quantization of light. Experimentally photoelectrons are analyzed with respect to their kinetic energy E and their momentum $\mathbf{p}$. Given the energy of light and work function, the binding energy of electrons before excitation can be determined by:

$$|E_B| = h\nu - \phi - E_{kin} \tag{2.1}$$

where $h\nu$ is the incident photon energy, ϕ is the work function of the solid and E_{kin} is the kinetic energy of photoelectrons. As shown in Figure 2.1, in the case of metals, core levels are at high binding energies and non-dispersing, valence bands are at low binding energies and the Fermi energy E_F is at the top of valence band and separated from vacuum by the work function ϕ. If an electron with a binding energy E_B absorbs a photon with energy $\hbar\nu$, the electron can get excited into vacuum and an photoelectron can be detected with a kinetic energy $E_{kin} = \hbar\nu - \phi - E_B$. The kinetic energy distribution of photoelectrons reflects the binding energy distribution of the electrons in solids, and can reveal detailed information about the electronic structure of solids. The electron energy distribution produced by incoming photons and measured as a function of kinetic energy E_{kin} of the photoelectrons is more

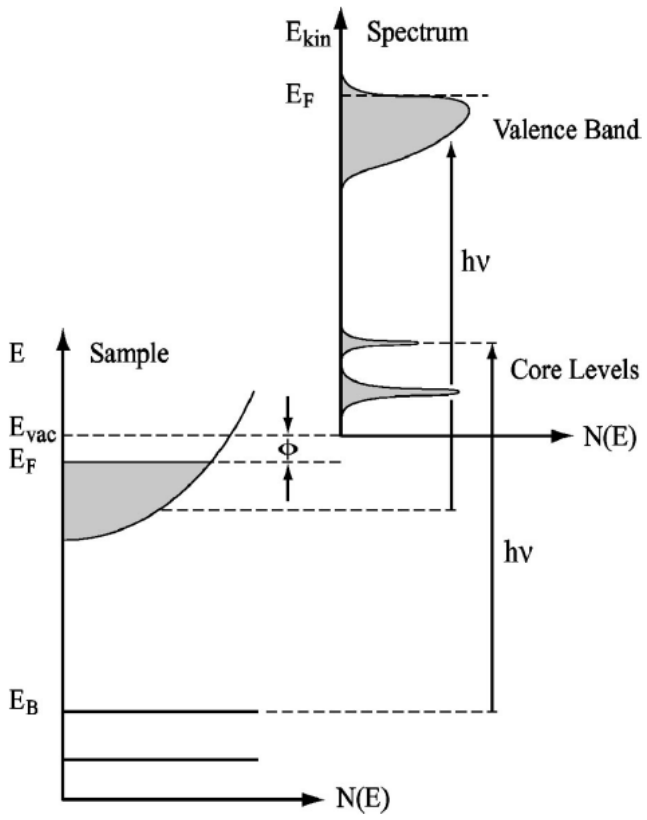

Figure 2.1: Energetics of the photoemission process [3]. Electrons with binding energy E_B absorb photons $\hbar\nu$ and escape into vacuum, becoming photoelectrons with kinetic energy $E_{kin} = \hbar\nu - \phi - E_B$.

conveniently expressed in terms of the binding energy E_B when one refers to the density of states inside solids ($E_B = 0$ at E_F) as shown in Figure 2.1. Based on the photoelectric effect, photoemission spectroscopy(PES) was developed and has been widely used in studying the electronic structure of solids.

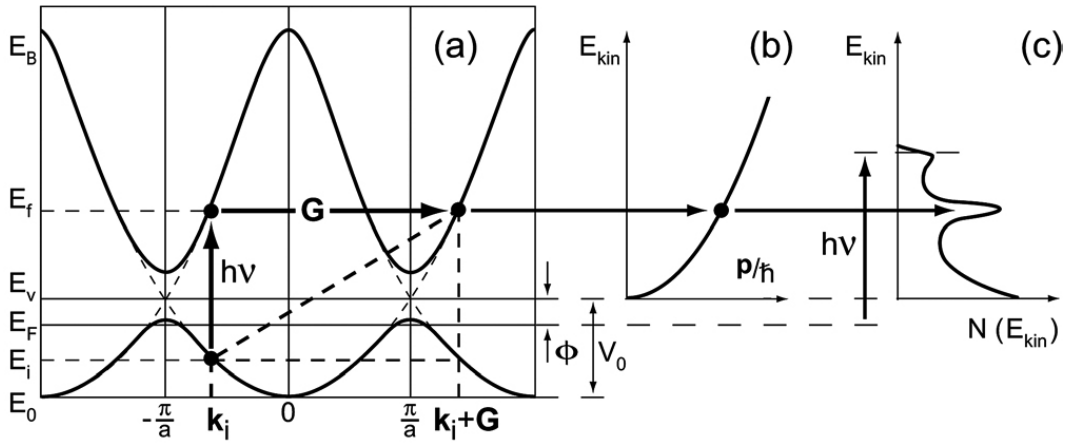

Figure 2.2: Kinematic of the photoemission process within the three-step nearly-free-electron final state model: (a) direct optical transition in the solid (the lattice supplies the required momentum); (b) free-electron final state in vacuum; (c) corresponding photoelectron spectrum, with a background due to the scattered electrons ($E_B = 0$ at E_F) [8].

The photoemission process is a single coherent process and can be rigorously and more accurately described by the one-step model [4]. In the one-step model, photon absorption, electron removal, and electron detection are treated as a single coherent process. In this case the Hamiltonian includes bulk, surface, and vacuum describing the crystal, which implies that not only bulk states have to be considered, but also

surface and evanescent states, as well as surface resonances. However, the one-step model is very complex that usually the three-step model [3] is used to describe photoemission, in which the photoemission process is subdivided into three independent and sequential steps:

1. Optical excitation of the electron in the bulk.

2. Travel of the excited electron to the surface.

3. Escape of the photoelectron into vacuum.

Three-step model is purely phenomenological but has been proven to be quite successful [5–7]. The following description gives a brief explanation of each step:

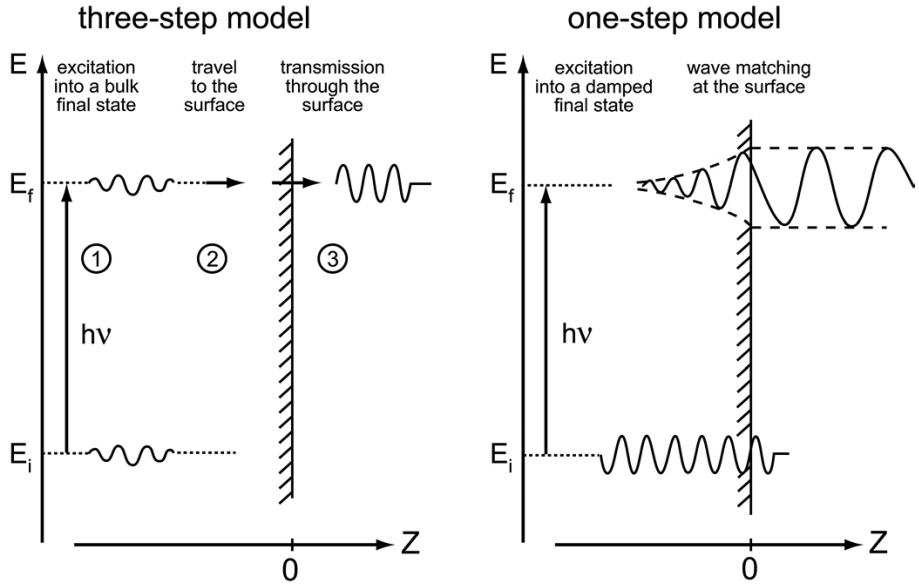

Figure 2.3: Three-step model (left) and one-step model (right) to describe the photoemission process.

Step one: It is the photon excitation process, during which an electron absorbs one photon and enters an unoccupied state. This can be described by the Fermi's golden rule:

$$w_{fi} = \frac{2\pi}{\hbar}|\langle\Psi_f^N|H_{int}|\Psi_i^N\rangle|^2\delta(E_f^N - E_i^N - h\nu) \tag{2.2}$$

where w_{fi} is the transition probability from the N-electron initial state Ψ_i^N to N-electron final state Ψ_f^N, and the interaction H_{int} is described with the dipole approximation:

$$H_{int} = -\frac{e}{mc}\mathbf{A}\cdot\mathbf{p} \tag{2.3}$$

where $\mathbf{A}$ is the electromagnetic vector potential with gauge Φ=0 and $\mathbf{p}$ is the electronic momentum operator.

Sudden approximation: During the process of photoexcitation, the system will relax after one electron is photoexcitated and can be very complex. The sudden approximation can be adopted to make the problem simpler, applicable to the high kinetic energy electrons. It assumes that once an electron absorbs a photon, its speed is so fast that the emitted electron hardly interact with the $(N-1)$ electrons left behind. In this limit, the photoemission process is assumed to be sudden, with no post-collisional interaction between the photoelectron and the system left behind. With this sudden approximation, the final state Ψ_f^N can be written as a product of wave function of photoelectron $\phi_f^{\mathbf{k}}$ and the state of the remaining $(N-1)$ electrons

Ψ_f^{N-1}:

$$\Psi_f^N = \mathcal{A}\phi_f^{\mathbf{k}}\Psi_f^{N-1} \tag{2.4}$$

where $\mathcal{A}$ is the operator that antisymmetrizes the wave function. Let us assume the initial state Ψ_i^N is a single Slater determinant in Hartree-Fock formalism, and write it as the product of a one-electron orbital $\phi_i^{\mathbf{k}}$ and a (N-1)-particle term:

$$\Psi_i^N = \mathcal{A}\phi_i^{\mathbf{k}}\Psi_i^{N-1} \tag{2.5}$$

where $\phi_i^{\mathbf{k}}$ is the orbital from which the electron is excited and Ψ_i^{N-1} is the wave function of the remaining $(N-1)$ electrons. With this approximation and from equation (2.2), we can write the transition probability as:

$$\langle\Psi_f^N|H_{int}|\Psi_i^N\rangle = \langle\phi_f^{\mathbf{k}}|H_{int}|\phi_i^{\mathbf{k}}\rangle\langle\Psi_m^{N-1}|\Psi_i^{N-1}\rangle \tag{2.6}$$

$$w_{fi} = \frac{2\pi}{\hbar}|\langle\phi_f^{\mathbf{k}}|H_{int}|\phi_i^{\mathbf{k}}\rangle|^2|\langle\Psi_m^{N-1}|\Psi_i^{N-1}\rangle|^2\delta(E_f^N - E_i^N - h\nu) \tag{2.7}$$

where $\langle\phi_f^{\mathbf{k}}|H_{int}|\phi_i^{\mathbf{k}}\rangle = M_{f,i}^{\mathbf{k}}$ is the one electron dipole matrix element, and the second term is the (N-1) electron overlap intergral. After excitation of the electron from orbital $\mathbf{k}$, the remaining $(N-1)$ electrons are in excited states and will relax to minimize their energy. Assuming that the final state with $(N-1)$ electrons has m excited states with the wave function Ψ_m^{N-1} and energy E_m^{N-1}, the total photoemission intensity measured as a function of E_{kin} at a momentum $\mathbf{k}$ is proportional to

$$\sum_{f,i}|M_{f,i}^{\mathbf{k}}|^2\sum_m|c_{m,i}|^2\delta(E_{kin} + E_m^{N-1} - E_i^N - h\omega) \tag{2.8}$$

where $c_{m,i} = \langle \Psi_m^{N-1} | \Psi_i^{N-1} \rangle$ such that $|c_{m,i}|^2$ is the probability that after removal an electron from orbital $\phi_i^{\mathbf{k}}$ from the N electron state and the remaining $(N-1)$ electrons will be in excited state m.

Step two: It can be described in terms of an effective mean free-path, proportional to the probability of the excited electron to the surface of solids. During the process, photoelectrons can be scattered by electrons and phonons. In most cases the electron-electron interaction mainly affects the mean free path. Even though the properties of materials can be very different, an universal mean free path curve can be drawn for energies of interest, because the electrons in solids can be approximated as free electrons. Figure 2.4 shows the universal curve of the mean free path at different photon energy, characterized a minimum about a few angstroms at 20 - 100 eV, which is the typical energy range widely used in ARPES measurements. This makes ARPES a surface technique, probing the electronic states within a few layers of the surface. Therefore, ARPES experiments have to be performed on atomically clean and well ordered systems, implying that fresh and flat surfaces have to be prepared immediately prior to the experiment in ultra-high vacuum (UHV) conditions.

Sticking coefficient: The sticking coefficient S is the term used in surface physics and defined as the ratio of the number of adsorbate atoms or molecules that stick to a surface to the number of total molecules impinging on the surface. Assuming $S = 1$, it takes 2.5 Langmuirs (1L = 10^{-6} torr·s) to cover one layer of a surface. Now

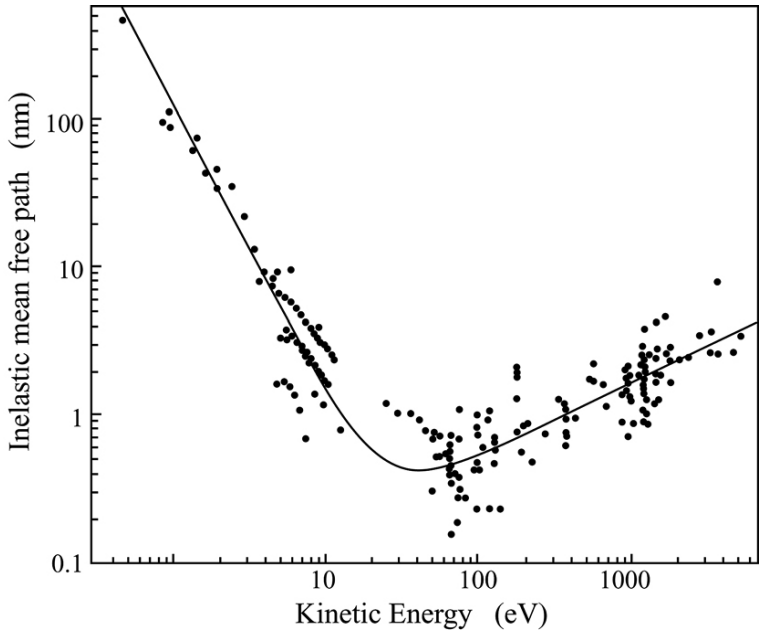

Figure 2.4: The *universal curve* for surface sensitivity in photoemission which shows the mean free path as a function of photon energy [9]. The data is measured on many different materials.

the vacuum can be as good as 2×10^{-11} torr, so it takes 13 hours to cover a surface. The sticking coefficient can be very different, depending on materials and molecules. BSCCO cuprates can survive in a vacuum chamber for several days without observable change of spectra. Similarly, ruthenates and iron-based superconductor can survive in UHV chamber for several hours without any contamination. To probe the bulk electronic structure of solids, one way is to increase the photon energy, called x-ray photoemission (XPS), which has poor energy and momentum resolution. An alternative way is to use low photon energy, which achives very high energy and momentum resolution, but covers less BZ. The photon energy that can be achieved with a laser is as low as 6 eV [11]. Nowadays, the interest in laser-ARPES is growing.

Step three: This describes the probability of photoelectrons escaping into the vacuum. There is a potential barrier between the solid surface and the vacuum. The potential is usually called the work function ϕ, which is the minimum energy needed for an electron at Fermi energy to escape into vacuum. Only those whose kinetic energy is higher than the work function can escape into vacuum. The work function (around 4-5 eV for metals) depends upon the material used for measurement.

2.2 Angle resolved photoemission spectroscopy (ARPES)

Figure 2.5 shows a geometry of an ARPES experiment in which the emission direction of the photoelectron is specified by the polar (θ) and azimuthal (ϕ) angles. This

figure illustrates schematicaly an ARPES setup with a light source, a sample, and a detector. When photons are incident on the surface of a sample, electrons in solids called photoelectrons can absorb photons and escape into vacuum to be collected by the detector. The kinetic energy E_{kin} of photoelectrons can be measured and

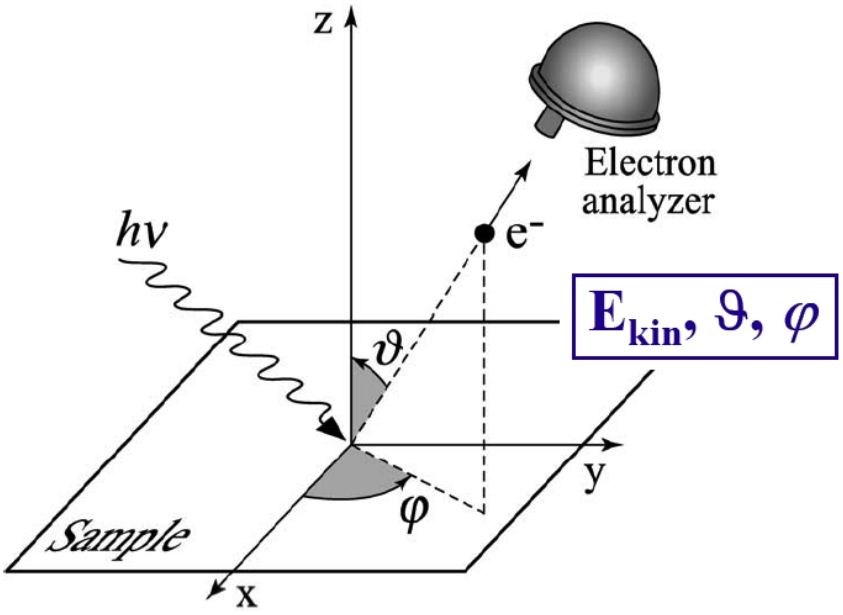

Figure 2.5: Schematic ARPES experimental set up [8]. Photon with energy $\hbar\nu$ impinges on the surface of samples. Electrons can absorb photon and be excited into vacuum. Those photoelectrons will be analyzed with respect to energy and momentum by an electron analyzer.

their momentum can be derived easily by $p = \sqrt{E_{kin}/2m}$. During the process of photoemission, the energy E and parallel momentum $k_{//}$ are conserved and can be

epxressed as below in terms of the kinetic energy E_{kin} and angle θ, ϕ:

$$k_x = \frac{1}{\hbar}\sqrt{2mE_{kin}}sin\theta cos\phi \tag{2.9}$$

$$k_y = \frac{1}{\hbar}\sqrt{2mE_{kin}}sin\theta sin\phi \tag{2.10}$$

ARPES measures the electron distribution $I(E_{kin}, \theta, \phi)$ with respect to E_{kin}, θ and ϕ, there is one-to-one mapping to $I(\omega, k_x, k_y)$. The intensity measured in ARPES experiment $I(\mathbf{k}, \omega)$ can be described as:

$$I(\mathbf{k}, \omega) = A(\mathbf{k}, \omega)f(\omega)I_0(\mathbf{k}, \omega, \mathbf{A}) \tag{2.11}$$

where $A(\mathbf{k}, \omega)$ is the single particle spectral function, $f(\omega)$ the Fermi-Dirac distribution function which implies that ARPES measures the occupied states only and $I_0(\mathbf{k}, \omega, \mathbf{A})$ the magnitude of matrix element $|M_{f,i}(\mathbf{k})|^2$ which depends on the electron momentum and on the energy and polarization of the incoming photon.

To describe an interacting many body system, a Green's function formalism is introduced. Green's function can be written in time-ordered $G(t - t')$, which can be interpreted as the probability amplitude that one electron added to the sytem at time t will stay in the same state at time t'. Green function can be written in energy-momentum representation as follows: $G(\mathbf{k}, \omega) = G^+(\mathbf{k}, \omega) + G^-(\mathbf{k}, \omega)$.

$$G^{\pm}(\mathbf{k}, \omega) = \sum_m \frac{|\langle \Psi_m^{N\pm1}|c_{\mathbf{k}}^{\pm}|\Psi_i^N\rangle|^2}{\omega - E_m^{N\pm1} + E_i^N \pm i\eta} \tag{2.12}$$

where $c_{\mathbf{k}}^+$ or $c_{\mathbf{k}}^-$ creates or annihilates an electron with energy ω, momentum $\mathbf{k}$ in the initial state Ψ_i^N, and η is a positive infinitesimal. The one particle spectral function

$A(\mathbf{k},\omega) = -(1/\pi)ImG(\mathbf{k},\omega)$ is written as:

$$A^{\pm}(\mathbf{k},\omega) = \sum_{m} |\langle \Psi_m^{N\pm1}|c_{\mathbf{k}}^{\pm}|\Psi_i^N|^2 \delta(\omega - E_m^{N\pm1} + E_i^N) \tag{2.13}$$

Green's functions can be expressed in terms of the self-energy $\Sigma(\mathbf{k},\omega) = \Sigma'(\mathbf{k},\omega) + i\Sigma''(\mathbf{k},\omega)$, which includes the information on electron-electron interactions. Its real and imaginary parts contain all the information on the energy renormalization and lifetime, respectively. Green's function can be written as:

$$G(\mathbf{k},\omega) = \frac{1}{\omega - \epsilon_k - \Sigma(\mathbf{k},\omega)} \tag{2.14}$$

$$A(\mathbf{k},\omega) = -\frac{1}{\pi}\frac{\Sigma''(\mathbf{k},\omega)}{[\omega - \epsilon_{\mathbf{k}} - \Sigma'(\mathbf{k},\omega)]^2 + [\Sigma''(\mathbf{k},\omega)]^2} \tag{2.15}$$

Among the general properties of the spectral function, there are several sum rules. Some fundamentals are given below:

$$\int_{-\infty}^{\infty} d\omega A(\mathbf{k},\omega) = 1 \tag{2.16}$$

$$\int_{-\infty}^{\infty} d\omega f(\omega) A(\mathbf{k},\omega) = n(\omega) \tag{2.17}$$

Given the spectral function $A(\mathbf{k},\omega)$, band dispersion and self-energy can be extracted. The Green's function has poles when $\omega - \epsilon_{\mathbf{k}} - \Sigma'(\mathbf{k},\omega) = 0$. This corresponds to $\omega = \epsilon_{\mathbf{k}} + \Sigma'(\mathbf{k},\omega)$, which is the renormlized band disperion. For interacting systems, self-energy Σ includes all the information about interactions, which make ARPES a powerful technique in probing the properties of solids. Assuming the self-energy Σ is $\mathbf{k}$ independent, then Σ can be extracted from ARPES data. With bare band $\epsilon_{\mathbf{k}}$

approximated by LDA calculations or just a linear approximation $\epsilon_{\mathbf{k}} = \mathbf{v_F} \cdot (\mathbf{k} - \mathbf{k_F})$, we can get:

$$\Sigma'(\mathbf{k}, \omega) = \omega - \epsilon_{\mathbf{k}} \tag{2.18}$$

Approximately, $A(\mathbf{k}, \omega)$ has a lorentzian lineshape with maximum of $-\frac{1}{\pi}\frac{1}{\Sigma''(\mathbf{k},\omega)}$, so that the width of half maximum can be reached when:

$$-\frac{1}{\pi}\frac{\Sigma''(\mathbf{k}, \omega)}{[\omega - \epsilon_{\mathbf{k}} - \Sigma'(\mathbf{k}, \omega)]^2 + [\Sigma''(\mathbf{k}, \omega)]^2} = -\frac{1}{2\pi}\frac{1}{\Sigma''(\mathbf{k}, \omega)} \tag{2.19}$$

Solving this equation will give:

$$\Sigma''(\mathbf{k}, \omega) = \frac{1}{2}(\epsilon_{k2} - \epsilon_{k1}) = \frac{1}{2}\frac{\partial \epsilon_{\mathbf{k}}}{\partial \mathbf{k}}\Delta\mathbf{k} \tag{2.20}$$

By measuring the width of the constant energy line, we can extract the imaginary part of the self-energy. In fact the real part and imaginary part of the self-energy are related by a Kramers-Kronig relation, meaning that with one of them we can derive the other. We can measure both of them from ARPES data. This analysis has been done many times and demonstrated its power in probing electron-phonon interactions and other electron interactions with other collective modes.

Figure 2.6 shows a typical 2-dimensional intensity map $I(\mathbf{k}, \omega)$, which is the ARPES intensity as a function of binding energy and momentum. The x-axis is the momentum and the y-axis is the energy. The intensity value gives the counting of photoelectrons at that momentum and energy.

Data Analysis There are the following ways to analyze ARPES data:

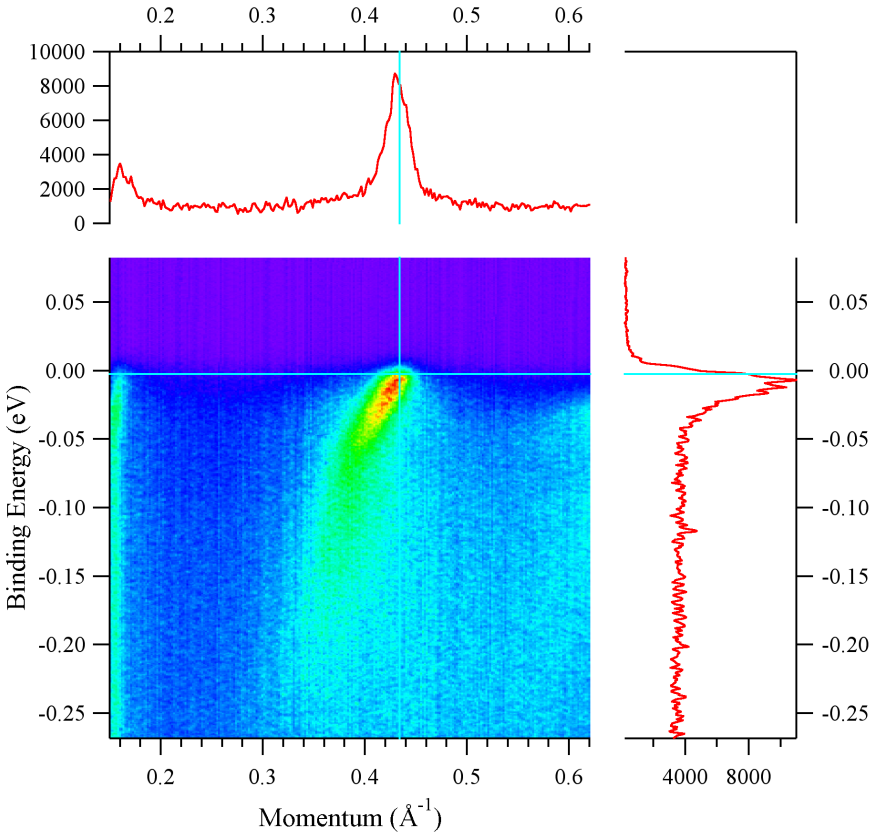

Figure 2.6: ARPES intensity plot with EDC and MDC. The image plot is a typical ARPES intensity map. The upper panel is the MDC line. The right one is the EDC line.

(1) *Energy Distribution Curves (EDCs)*: The data analyzed through a constant momentum line is called energy distribution curve (EDC), which is the ARPES intensity as a function of energy and,

(2) *Momentum Distribution Curves (MDCs)*: The data analyzed through a constant energy line is called momentum distribution curve (MDC) [12], which is ARPES intensity as a function of momentum. These two curves are used frequently in the analysis of ARPES data. The EDC function can be expressed as:

$$I_{EDC}(\omega) = I_0(\mathbf{k}_{const}, \hbar\nu, \mathbf{A})\frac{1}{\pi}\frac{\Sigma''(\mathbf{k},\omega)}{[\omega - \epsilon_{\mathbf{k}} - \Sigma'(\mathbf{k},\omega)]^2 + [\Sigma''(\mathbf{k},\omega)]^2} f(\omega) \tag{2.21}$$

We can see that the EDC spectra involves the almost constant matrix element. This is an advantage of the EDC analysis. However, an EDC has a non-trivial ω-dependence: (i) an EDC is not a lorentzian or any simple function; (ii) an EDC has the Fermi function term, which makes it asymmetric; (iii)its peak postion is not given by the pole condition; (iv) at last the EDC width does not only depend on the imaginary part of the self-energy Σ'', but also the real part of the self-energy Σ'. All this make the data analysis of an EDC complicated. Since the development of the Scienta analyzer, which can measure the two-dimensional map at the same time with better resolution, MDC analysis becomes available.

$$I_{MDC}(\mathbf{k}) = I_0(\mathbf{k}, h\nu, \mathbf{A})\frac{1}{\pi}\frac{\Sigma''(\mathbf{k},\omega)}{[\omega - \epsilon_{\mathbf{k}} - \Sigma'(\mathbf{k},\omega)]^2 + [\Sigma''(\mathbf{k},\omega)]^2} f(\omega_0) \tag{2.22}$$

MDC analysis has some advantages: (i) in the vincity of the Fermi energy, the MDC lineshape is symmetric lorentzian; (ii) MDC will not be affected by the Fermi function.

(3) *Second Derivative Intensity Plot (SDI)*: In principal, the EDCs and MDCs analysis should be enough to determine the band dispersion. However, it is difficult to do so when the peaks in EDCs and MDCs are broad, especially when there are several broad bands. In that case, the second derivative of EDCs (or MDCs) can be used to enhance broad peaks and it helps to track the band dispersions well. After taking the second derivative of a function, any bump in this function will be turned into a sharper dip, and the minimum point of the dip is the position of the bump present before. Multiplying by negative sign to second derivative, we can turn the dip into a peak. We have used second derivative of intensity plots in the coming chapter to analyze the ARPES data.

2.2.1 Matrix elements and finite-resolution effects

The measured ARPES intensity $I(\mathbf{k}, \omega)$ is the product of the spectral function $A(\mathbf{k}, \omega)$, the Fermi function $f(\omega)$ and the matrix element $I_0(\mathbf{k}, \omega, \mathbf{A})$. The matrix element depends on photon energy, electron momentum, geometry setting and light polarization. Sometimes the matrix element can suppress the photoelectron intensity, which is not good for measuring the spectral function. On the other hand, we can also choose different matrix elements to enhance some bands while suppressing others. This can also give us some information about the electronic structure of solids.

As we know, ARPES directly probes the one-particle spectral function $A(\mathbf{k}, \omega)$. However, in extracting the quantitative information from the experiment, not only the

effect of the matrix element term $I_0(\mathbf{k}, \omega, \mathbf{A})$ has to be considered, but also the finite experimental resolution and the extrinsic continuous background due to the secondary photoelectrons (those electrons which escape from solid after having suffered inelastic-scattering events and, therefore, with a reduced E_{kin}). The resolution functions are energy resolution (typically a Guassian) and momentum resolution (more complicated function). For background correction, there are different kinds of functions used. For example, the step-edge background consists in three parameter for height, energy position, and width of the step-edge, which reproduces the background observed all the way to E_F in an unoccupied region of momentum space.

The matrix element can be written as:

$$M_{f,i}^{\mathbf{k}} = \langle \phi_f^{\mathbf{k}} | - \frac{e}{mc} \mathbf{A} \cdot \mathbf{p} | \phi_i^{\mathbf{k}} \rangle \tag{2.23}$$

By using the commutation relation $\hbar \mathbf{p} = -i[x, H]$, matrix element becomes:

$$\langle \phi_f^{\mathbf{k}} | - \frac{e}{mc} \mathbf{A} \cdot \mathbf{p} | \phi_i^{\mathbf{k}} \rangle = \langle \phi_f^{\mathbf{k}} | - \frac{e}{mc} \mathbf{A} \cdot \mathbf{r} | \phi_i^{\mathbf{k}} \rangle \tag{2.24}$$

ARPES is usually done in the UHV region, ranging from a few eV to a few hundred eV. For $\hbar\omega = 10$ eV, one has $\lambda = 10^3$ Å, which is much larger than the lattice constant and therefore A can be taken as constant. As shown in Figure 2.7a, the initial orbital has the $d_{x^2-y^2}$ symmetry, which is even with respect to the mirror plane. The final state is taken as plane waves $e^{i\mathbf{k}\cdot\mathbf{r}}$. For k whose direction is even to the mirror plane, the intensity is strong. For k whose direction is odd to the mirror plane, the total integral will be zero. For a generic initial state of either even or odd symmetry with

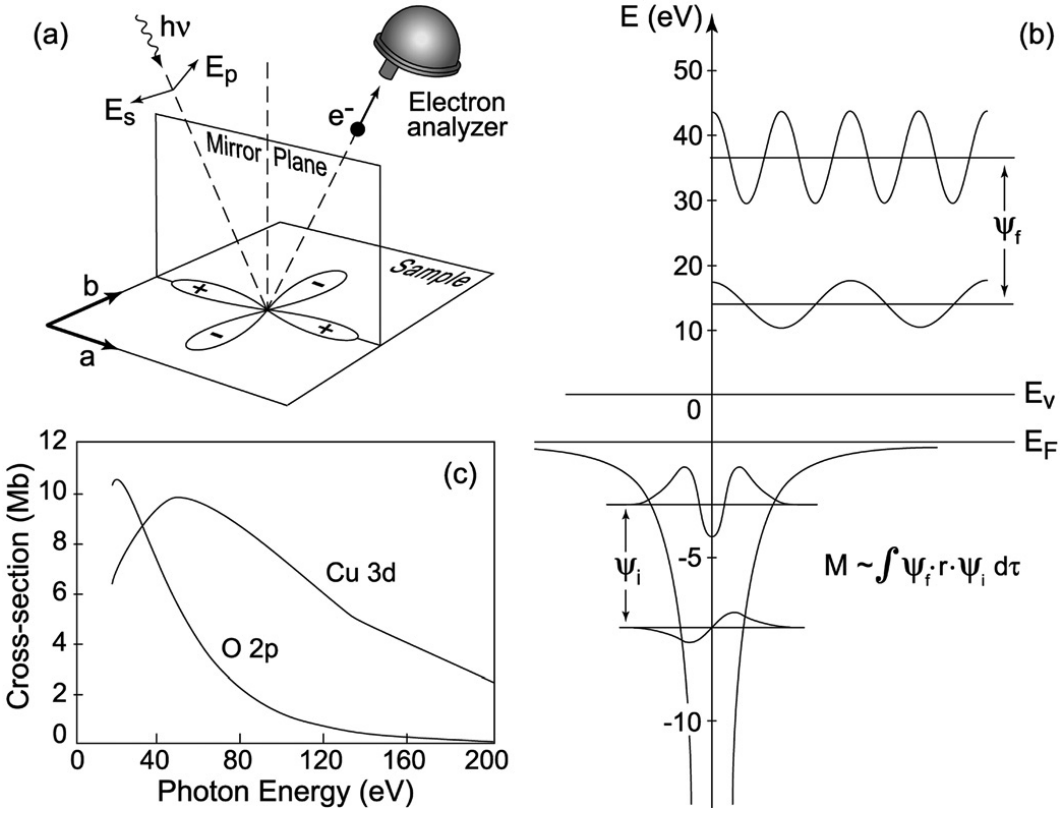

Figure 2.7: Schematic representation of the polarization and photon energy effects in the photoemission process. (a) Mirror plane emission from a $d_{x^2-y^2}$ orbital. (b) Sketch of the optical transition between atomic orbitals with different angular momenta (the harmonic oscillator wavefunctions are here used for simplicity) and free electron wavefunctions with different kinetic energies [22]. (c) Calculated photon energy dependence of the photoionization cross-sections for Cu 3d and O 2p atomic levels [13].

respect to the mirror plane, the polarization conditions resulting in an overall even matrix element can be summarized as:

$$\langle\phi_f^{\mathbf{k}}| - \frac{e}{mc}\mathbf{A}\cdot\mathbf{r}|\phi_i^{\mathbf{k}}\rangle \begin{cases} \phi_i^{\mathbf{k}} & even & \langle+|+|+\rangle & A & even \\ \phi_i^{\mathbf{k}} & odd & \langle+|-|-\rangle & A & odd \end{cases}$$

The matrix element also depends on photon energy. Assuming that the photoelectron is a plane wave $e^{i\mathbf{k}\cdot\mathbf{r}}$, one can rewrite the matrix element as:

$$|M_{f,i}^{\mathbf{k}}|^2 \propto |\langle\phi_f^{\mathbf{k}}|\mathbf{A}\cdot\mathbf{r}|\phi_i^{\mathbf{k}}\rangle|^2 \propto |(\mathbf{A}\cdot\mathbf{k})\langle\phi_i^{\mathbf{k}}|e^{\mathbf{k}\cdot\mathbf{r}}\rangle|^2 \tag{2.25}$$

If the incident photon energy increases, the momentum $\mathbf{k}$ and the kinectic energy also increase. Then, the matrix element changes in a non-necessarily monotonic fashion. As shown in Figure 2.7c, the cross section of Cu $3d$ and O $2p$ electrons are photon energy dependent. Besides its photon energy dependence, the matrix element $|M_{f,i}^{\mathbf{k}}|^2 \propto |\mathbf{k}\cdot\mathbf{k}|^2$ causes the intensity to zero when the system is symmetry forbidden.

2.3 Experimental aspects

An ARPES system consists of several components, mainly detector, light source, and vacuum system.

Detector ARPES measures a continuous spectrum of photoelectron intensity as a function of kinetic energy and space angle, which is done by an electron energy analyzer. There are many types of electron analyzers using different mechanisms. In principle, four methods can be used to analyze the energy of an electron [22]:

1. The use of resonances in a scattering process.

2. The time-of-flight.

3. The deceleration of an electron using a retarding electric field.

4. The change of the orbit of a particle by an electric or magnetic field.

Now most widely used detectors in ARPES are hemispherical detectors, which use the forth method to convert energy resolution into space resolution. A conventional hemispherical analyzer consists of a multielement electrostatic input lens, a hemispherical deflector with entrance and exit slits, and electron deflectors (i.e., a channeltron or multichannel detector). The heart of the analyzer is the deflector. The mechanism of the energy analyzer, shown schematically in Figure 2.8, involves an inner and an outer hemispheres, with radius R_1 and R_2. High voltage difference ΔV is applied the two hemispheres. The electric field generated between the inner and outer concentric hemspheres will allow eletrons with a narrow kinetic energy range to pass through, while all other electrons will hit the inner or outer plates. The energy is pass energy $E_{pass} = e\Delta V/(R_1/R_2 - R_2/R_1)$. Electrons will be retarded or accelerated to this kinetic energy to pass through.

Electrons lens: The lens can retard the electrons to the energy that can be detected by the analyzer. A two dimensional high resolution detector is mounted at the exit slit of the analyzer. The detector is highly position resolved, and can convert electrons

into light, which can be detected by a CCD camera. The resolution measured with E_{pass} is determined by the radius and the slits, $\Delta E_\alpha = E_{pass}(w/R_0 + \alpha^2/4)$.

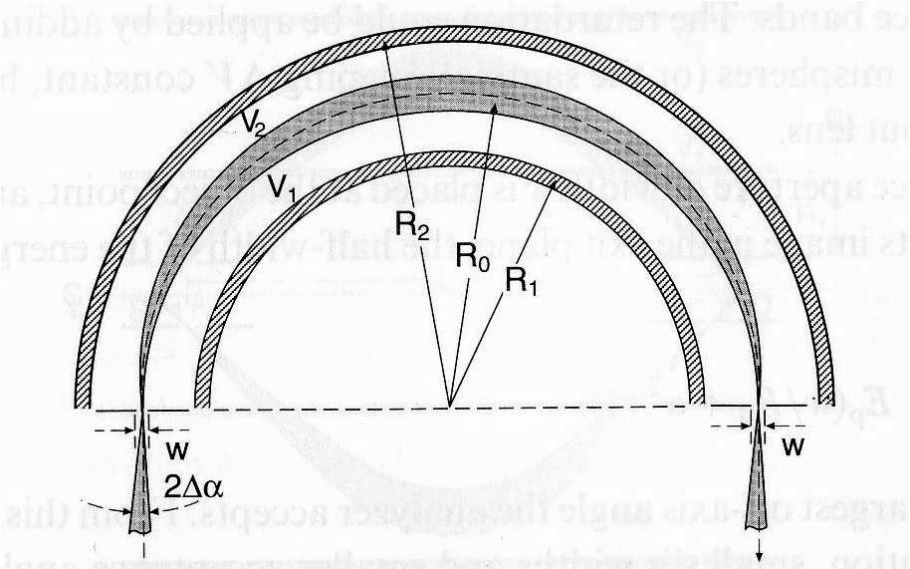

Figure 2.8: Hemispherical electron analyzer [22]. The inner and outer hemispherical plates with radius R_1 and R_2 are connected to high voltage V_1 and V_2.

Detectors manufactured by Scienta such as SES 2002, R4000, SES 100 have been used to collect data in this work. The Scienta detector can measure the 2 dimensional spectra simutaneouly and can achieve high energy and momentum resolution. The detector consists in three parts: (1) hemispherical energy analyzer; (2) electron lens; (3) two dimensional high resolution electron detector. The Scienta analyzer system is doubly μ-metal shielded to reduce the effect of a magnetic field even in presence of strong magnetic field. The Scienta detector (SES 2002) is a 200 mm radius hemispherical analyzer. The lens can be utilized in several modes of operation in order

to give an optimum performance in different types of experiments such as UV light ARPES and XPS. It has an energy resolution of 2 meV at the pass energy $E_p = 2$ eV and an angular resolution of about 0.1 degree. At the photon energy 22 eV, Scienta detectors can resolve up to 1/50 of the first Brillouin zone of a high T_c cuprates.

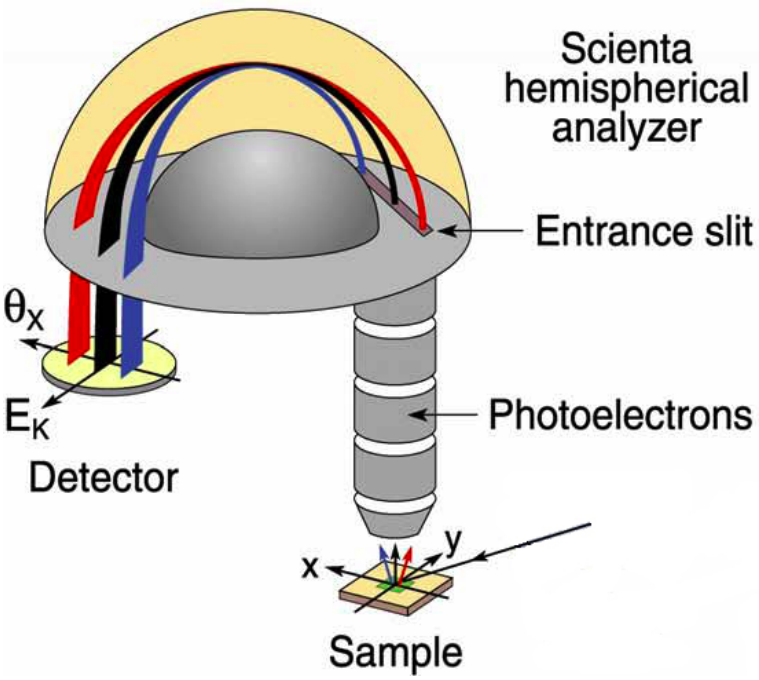

Figure 2.9: Scienta hemispherical detector. The detector is composed of photoelectron lens, a hemispherical analyzer and a detector.

As shown in Figure 2.9, the electron lens collect photoelectrons. With a retarded potential, the lens can retard photoelectrons and reduce their kinetic energy to E_{pass} and spread the electrons from different angles to different positions at the entrance slit. At each angle, electrons have an energy dispersion. Then at the exit slit, the photoelectron spectrum has been converted into a space resolution. A detector is

mounted at the end of the exit slit to detect photoelectrons. It includes a micro channel plane (MCP) and a phosphor plane in series, and the light is detected by a CCD camera. The product Seienta R4000 can achieve: (1) a submev resolution; (2) a 4000 resolving power; (3) a 30 degrees wide acceptance angle; (4) can work with up to 10 keV kinetic energy.

Light source The light source used in ARPES should provide a high intensity of monochromized photons able to emit electrons from the sample. The work function ϕ of a typical material is about 4-5 eV, so the photon energy should be higher than this to knock out electrons. Usually ARPES experiments are performed within the photon energy range from a few electronvolts to a few hundred electronvolts. Basically, there are three kinds of light sources used in ARPES: synchrotron light, gas discharge lamp and laser. As for the work presented in this thesis, most data were taken with synchrotron light and He lamps.

Synchrotron radiation The application of synchrotron radiation in photoemission was used since the late 1960s at a few first-generation sources. The second-genaration synchrotrons are purposely designed storage rings to serve as a source of synchrotron radiation. The third-generation started in 1990s are designed to optimize the characteristics of electron beams in the straight sections, which can accommodate longer insertion devices.

The basic principle of the synchrotron radiation can be explained by classical

electrodynamics. When charged particles move at at a relativistic velocity and are accelerated perpendicular to their trajectory, there will be electromagnetic radiation by particles. The acceleration is usually achieved by magnetic fields. Due to the relativistic energy of the particles the generated light has superior properties. If the electron is relativistic, the radiation emission occurs tangentially to the trajectory and the beam is highly focused. The synchrotron light is usually continuous over a wide range of wave-lenghts. The spectrum of synchrotron radiation covers visible light, ultra-violet (UV) and X-ray radiations. The natural divergence of the radiation is very small and collimators further reduce it. Linear or circular polarizations, which can be achieved depending on the application, is of particular interest in investigations of magnetic systems and orbital symmetry. Gratings are used to get monochronized light coming from synchrotron sources. Close to the chamber, light is focused with mirrors. The diagram is shown in Figure 2.10.

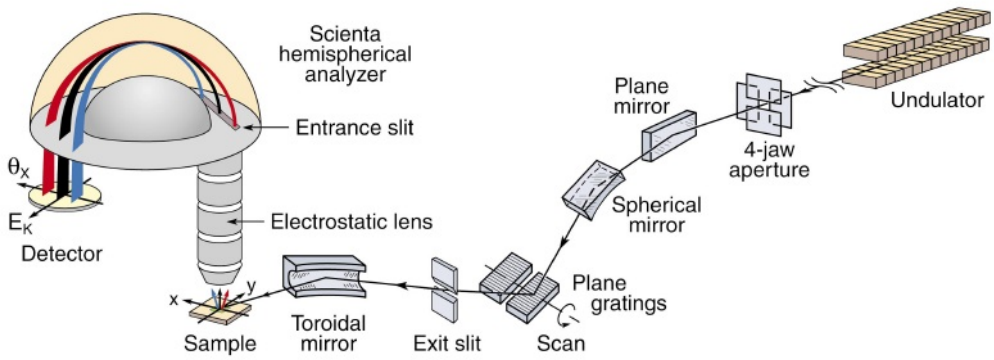

Figure 2.10: Schematic diagram of PGM Beam line and a Scienta electron spectrometer.

Synchrotron light has several advantages:

- High brightness.
- Wide energy range, tunable from infrared to hard X-ray.
- Polarized (linear and circular).

The work presented here has been performed with synchrotron beam at Advanced Light Source (ALS) beam line BL12, Synchrotron Radiation Center (SRC) U1-NIM, Wadeworth and PGM, and National Synchrotron Light Source (NSLS) U13. Different beamlines have optimal performance at different energy range and different end stations. The 200 line/mm grating at ALS BL12 can provide 10^{13} photons/s at 134 eV, which is quite bright. The energy range is from 28 to 320 eV.

Helium discharge lamp Helium lamp is a simple light source which utilizes the Helium resonance lines coming from the dilute plasma of He. It is a monochromized ultraviolet light source. Helium has two characterized lines: HeI energy is 21.2 eV and HeII energy is at 40.8 eV. Several characters make He lamp a good light source: (i) it is easy to operate; (ii) the size is small (iii); the energy is appropriate for ARPES experiment; (iv) the line width of He resonance is 10 meV or less; (v) He gas is inertial element and has weak contamination effect to most samples after using small apertures and differential pumping between the lamp and the sample chamber. The new generation He lamps utilize the Electron Cyclotron Resonance(ECR) mechanism to produce low pressure He plasma. ECR is created in a small metallic discharge

cavity by the application of a strong permanent magnetic field B, perpendicular to the microwave E vector. Under ECR, electrons will move in a circular motion with a frequency of 10 GHz microwave. The circulation motion in the cavity will increase the probability of electrons colliding with He atoms, and produce a high flux of radiation.

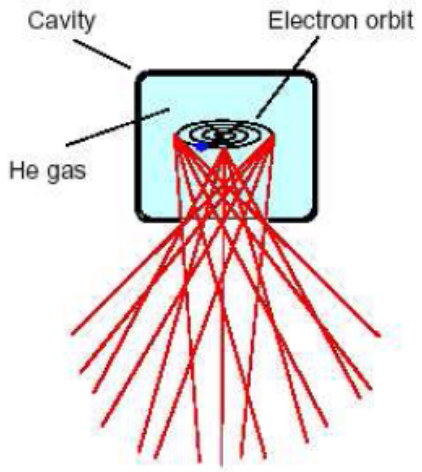

Figure 2.11: Low pressure helium gas in a small cavity is excited by ECR electrons to produce high intensity UV radiations.

Low pressure of He can increase the intensity ratio of HeII to HeI. This design can produce HeI with linewidth of 1.1 meV. The He lamp setup includes: (1) a microwave generator; (2) a resonance cavity; (3) an He source; (4) differential pumping; (5) a grating. He lines have two components, for example He I_{α} and I_{β} for the He I line, and a grating is introduced to get monochronized light. At the same time, the grating can work as a focusing mirror. There are some disadvantages related to the He lamp: (1) the flux is not as high as an undulator beamline; (2) the photon energy can not

be tuned; (3) the gas flow will get into the measurement chamber without a filter, thus affecting the vaccum; (4) light spot is large so momentum resolution is not good, thus a large flat surface is necessary.

Laser source Although the synchrotron sources offer unparalleled flexibility in wavelength tunability, the cost is on the order of 100 million dollars and also it requires a large support staff for operation and maintenance. Because of this, and the fact that there are currently only four synchrotron facilities in the United States at which high-resolution ARPES experiments are regularly performed, there is a great deal of competition for beam time. Alternative photon sources for ARPES, such as lasers, are therefore highly desirable. There are developments of table-top 6 eV laser photon sources. These sources offer state-of-art in resolution and other aspects of data quality such as bulk sensitivity.

Vacuum system ARPES experiment are usually performed with photon energy 10-100 eV, with a mean free path of about 5-20 Å, just the top most layers of the sample. Fresh, flat and atomically ordered surfaces are critical to ARPES measurements. Basically, vacuum pressure can be divided as follows:

1. Rough (low) vacuum: 10^{-3} Torr
2. Medium vacuum: 10^{-3} - 10^{-5} Torr
3. High vacuum (HV): 10^{-6} - 10^{-8} Torr

4. Ultra-high vacuum (UHV): $< 10^{-9}$ Torr

For ARPES experiments, samples must be cleaved and measured in a UHV environment. To construct vacuum systems, different kinds of pumps are used such as mechanical pump, turbo pump, sublimation pump, cryogenic pump, ion pumps etc... The following gives a brief introduction of the different pumps used in ARPES systems.

Mechanical pump This pump is based on *positive displacement*, where the gas is transported by means of pistons, gears, vanes, rotating cams, and so on. A typical mechanical pump consists of an inlet, and an exhaust with a one-way valve, and an off-centre rotating piston in a cylindrical cavity. As the piston rotates, gas is pulled into the cavity, and is forced out through the exhaust port. The rotating piston has spring-loaded vanes to create a seal with the cavity wall. A rotary pump uses rotating vanes to display gases. Low-vapor-pressure oil is used for sealing, lubrication and cooling purpose. This pump can create a pressure of $\sim 10^{-3}$ [14].

Turbo pump This pump is based on *momentum transfer*, where the pumped gas is entrained in and removed by an energetic stream of a pumping fluid or directed by fast-moving blades. Turbomolecular pumps use a series of high-speed rotors (25,000 to 75,000 rpm) and flow stabilizing, stationary stators to impart a preferential motion to gas molecules and create molecular flow through the pump. They are called "molecular bats" or "axial flow turbines". Multiple stages consisting of rotor/stator

pairs are mounted in series and mechanical energy of the blades is transfered into gas molecules. Magnetic bearings are used to reduce friction and oil contamination. A turbomolecular pump mechanism cannot exhust directly to atmosphere and thus requires a backing pump. Usually, a oil sealed rotary vane pump is used as a backing pump [14].

Ion pump This pump is based on *entrainment*, where the gas is absorbed on the surface of a suitable material that may or may not be refrigerated. Ion pumps utilize a sputtering process to ionize gas molecules and embed them into an anode or cathode wall. The entrainment process can utilize a getter such as titanium to bind and bury the molecules. They can operate in the ultra high vacuum range and eliminate contamination by organic molecules.

The pumping action in sputter-ion pumps is thought to be produced by the following processes [14]:

1. Ion burial and entrapment within the metal lattice a few atomic layers under the surface of the cathode.

2. Gettering of chemically active gases at the cathode and elsewhere by sputtered deposits.

3. Diffusion of hydrogen into the cathode material.

4. Dissociation of complex molecules into simpler fractions which are then pumped by one of the mechanism.

5. Production of neutral atoms of high velocity (or energy) by neutralization of ions and scattering from the cathode surface.

Sublimation pump Getter or titanium sublimation pumps (TSP) entrain gas molecules in a getter, or material that is vaporized in order to absorb or capture the molecules, and embed them on the cold outer wall of the chamber. Using a large-surface area porous matrix for entrainment, we can also sue "non-evaporating Gettering sorption" technique.

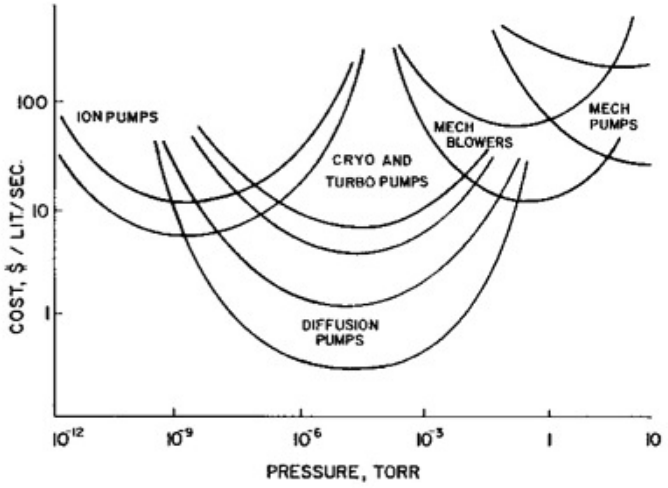

Figure 2.12: Pressure regions showing effectiveness of particular pumps [14].

Cryogenic pump One of the simplest ways of creating vacuum is to lower the temperature of a gas until it condenses into a liquid and then becomes a solid. Cryogenic pumps utilize extremely cold (at the temperature of liquid He and N_2) surfaces and adsorption surfaces to freeze or trap molecules. These pumps can operate with

relatively high pressures. Modern cryopumps are usually built as self-contained units with their own vacuum shell and an inlet flange, similar to diffusion pumps and turbomolecular pumps. The cooling is achieved by the use of mechanical cryorefrigerators at a temperature of 10 to 20 K and combining condensation and sorption [14].

Each pumping device has certain advantages of performance, cost, and process compatibility which make its use preferable in particular applications. This general concept of practicality is illustrated in Figure 2.12, where approximate costs for a variety of pumping speeds is shown relative to inlet pressure.

Bibliography

[1] H. Hertz, Ann. Physik **31**, 983 (1887).

[2] A. Einstein, Ann. Physik **17**, 132 (1905).

[3] S. Hüfner, Photoelectron Spectroscopy, (Springer-Verlag, Berlin, 1995).

[4] Mahan, G. D., Phys. Rev. **B**, 4334 (1970).

[5] P. J. Feibelman, and D. E. Eastman, Phys. Rev. B **10**, 4932 (1974).

[6] Fan, H. Y., Phys. Rev. **68**, 43 (1945).

[7] C. N. Berglund, and W. E. Spicer, Phys. Rev. **136**, A1030 (1964).

[8] A. Damascelli, Z. Hussain and Z. -X. Shen, Rev. Mod. Phys. **75**, 473 (2003).

[9] M. P. Seah and W. A. Dench, Surf. Interface Anal. **1**, 2 (1979).

[10] S. Souma, T. Sato, and T. Takahashi, Rev. of Sci. Instrument **78**, 123104 (2007).

[11] J. D. Koralek *et al.*, Phys. Rev. Lett. **96**, 017005 (2006).

[12] T. Valla *et al.*, Science **285**, 2110 (1999).

[13] J. J. Yeh *et al.*, Atom. Data Nucl. Data Tabl. **32**, 1 (1985).

[14] M. H. Hablanian, High-Vacuum Technology: A Practical Guide (Marcel Dekker, Inc., 1990).

Chapter 3

Metal insulator transition and $Ca_{2-x}Sr_xRuO_4$

3.1 Introduction

In condensed-matter systems, metal insulator transitions (MIT) are widely observed which are accompanied by high resistivity changes even over tens of orders of magnitude. Among them, the very interesting and important ones are the transitions driven by correlations associated with on-site electron-electron Coulomb repulsion. The insulating phase caused by the correlation effects is categorized as the Mott insulator. Near the transition point, the metallic states often show fluctuations or ordering in the spin, charge, and orbital degrees of freedom. The physical properties are very different from ordinary metals. Many new theoretical models have been developed

over the years to explain the doped Mott insulators because the properties of these insulators can not be explained by simple models based on Fermi-liquid theory [1].

Many facinating properties of the correlated meterials near metal-insulator transition have been studied extensively in d-lectron systems such as high-T_c superconducting cuprates. More recently, other kinds of correlatated systems such as ruthenates, cobaltates, and iron-based superconductors have attracted interest due to novel superconducting and other exotic phases in these systems.

Here we will discuss the physical properties calcium substituted Sr_2RuO_4 ($Ca_{2-x}Sr_xRuO_4$). Sr_2RuO_4 (called as Sr214) is isostructure with first high T_C superconductor $La_{2-x}Ba_xCuO_4$ and this is only perovskite superconductor which contains no copper. Although, it shows low T_c ($\sim$ 1.5 K), attention was given due to its unconventional superconducting states (possibly p-wave spin triple), which can not be described by BCS theory.

By substituting Ca for Sr, $Ca_{2-x}Sr_xRuO_4$ can quickly lose its superconductivity and eventually become an insulator. The subsitution of isovalent but smaller Ca^{2+}-ion for Sr^{2+}-ion does not lead to a more metallic state. Instead, the system changes from superconductor to paramegnetic metal, ferromagnetic metal, and finally aniferromagnetic insulator with increasing Ca concentration.

$Ca_{1.5}Sr_{0.5}RuO_4$ is believed to be a quantum critical point (QCP) because at this doping, the susceptibility diverges and the corresponding Curie temperature approaches zero Kelvin. The end member Ca_2RuO_4 , is a Mott antiferromagnetic insulator. Therefore, Ca substitution connects the system from metal to insulator.

$Ca_{1.8}Sr_{0.2}RuO_4$ is also interesting to study because it shows a metal/non-metal transition by varying temperature and calcium concentration, and it is at the boundary between a magnetic metal and an antiferromagnetic insulator. It also exhibits non-Fermi liquid behaviors in the resistivity. The Mott transition is believed to be driven by the change of electron filling among multiple orbitals. Thus, $Ca_{2-x}Sr_xRuO_4$ can be called a "doped Mott insulator". This gives a golden opportunity to study the evolution of electronic structure from a multi-band metal to a Mott insulator in an isoelectronic system.

3.2 *d*-electron system

This thesis mainly describes electronic states of the d electron system such as ruthenates ($4d$ system) and Fe ($3d$) system. The electronic states of d- electron system is described as follows.

The atomic orbitals of transition-metal elements are made as eigenstates under the spherical potential generated by the transition-metal ion. Due to periodic potential of atoms, the atomic orbital forms bands. In transition-metal compounds, the overlap is often determined by indirect transfer between d orbitals through ligand p orbitals. In $4d$ system, $4s$ and $4p$ bands are pushed well below the d band, where screening effects by $4s$ and $4p$ is weak. In case of $3d$ orbital, the bands are formed under the strong influence of anisotropic crystal field in solids.

Figure 3.1 shows an example of the crystal field splitting. In this case cubic lattic

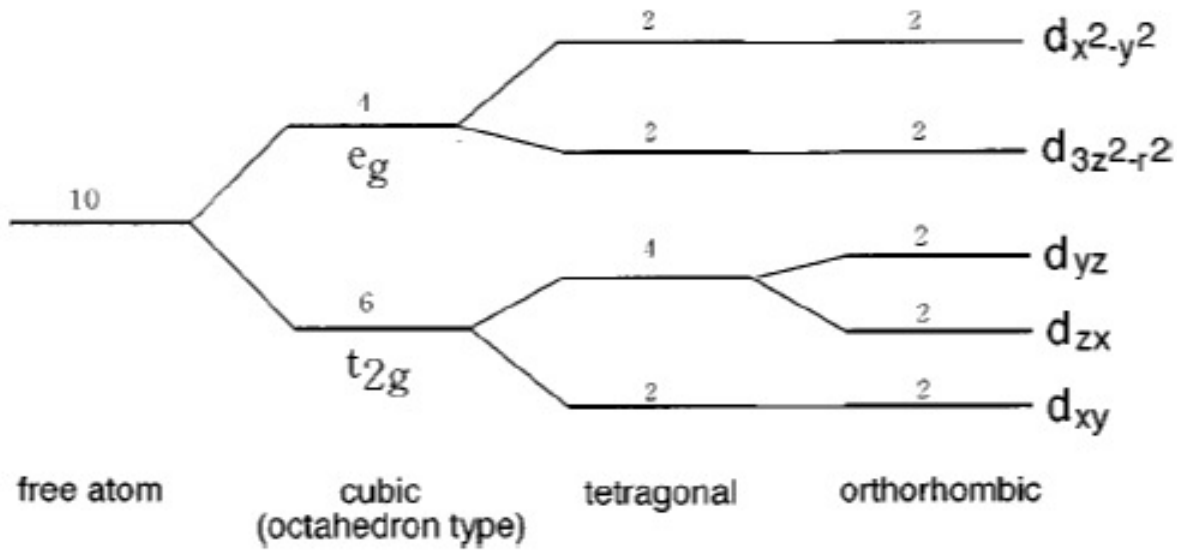

Figure 3.1: Crystal-field splitting of $3d$ orbitals under cubic, tetragonal and orthorhombic symmetries. [1].

symmetry promotes to a higher energy level of fourfold degenerate e_g orbital and sixfold degenerate lower orbitals t_{2g}. When the atom is surrounded by ligand atoms having octahedron configuration, the e_g orbital has anisotropy with larger amplitude in the direction of the principle axes. Thus e_g orbital further expands into $d_{x^2-y^2}$ and $d_{3z^2-r^2}$ orbitals. Similarly, the t_{2g} orbital has anisotropy with larger amplitude of the wave function toward other directions and may be represented by d_{xy}, d_{yz}, and d_{zx} orbitals.

Figure 3.2 shows an example of configurations for transition-metal $3d$ orbitals which are bridged by ligand p orbital. Here the relevant $3d$ orbitals and oxygen $2p$ and As $3p$ orbitals become closer in case of cuprates and pnicties respectively. This is mainly because the positive nuclear charge increases with change, which makes the chemical potential of the d electrons lower and closer to the p orbital. It is important to consider the hybridization effects between $4d$ and p orbitals.

3.3 Metal-insulator transition

The first theory of explaining metal-insulator transition is based on a non-interacting or weakly interacting electron system. This theory explains materials according to electrons at the outermost orbital at zero temperature. For example, in the case of insulators, the highest electron band is completely filled, while, for metals, it is partially filled. Alternatively, we can say that the Fermi energy level lies in a band gap for insulators while it is inside bands for a metal. For non-interacting systems,

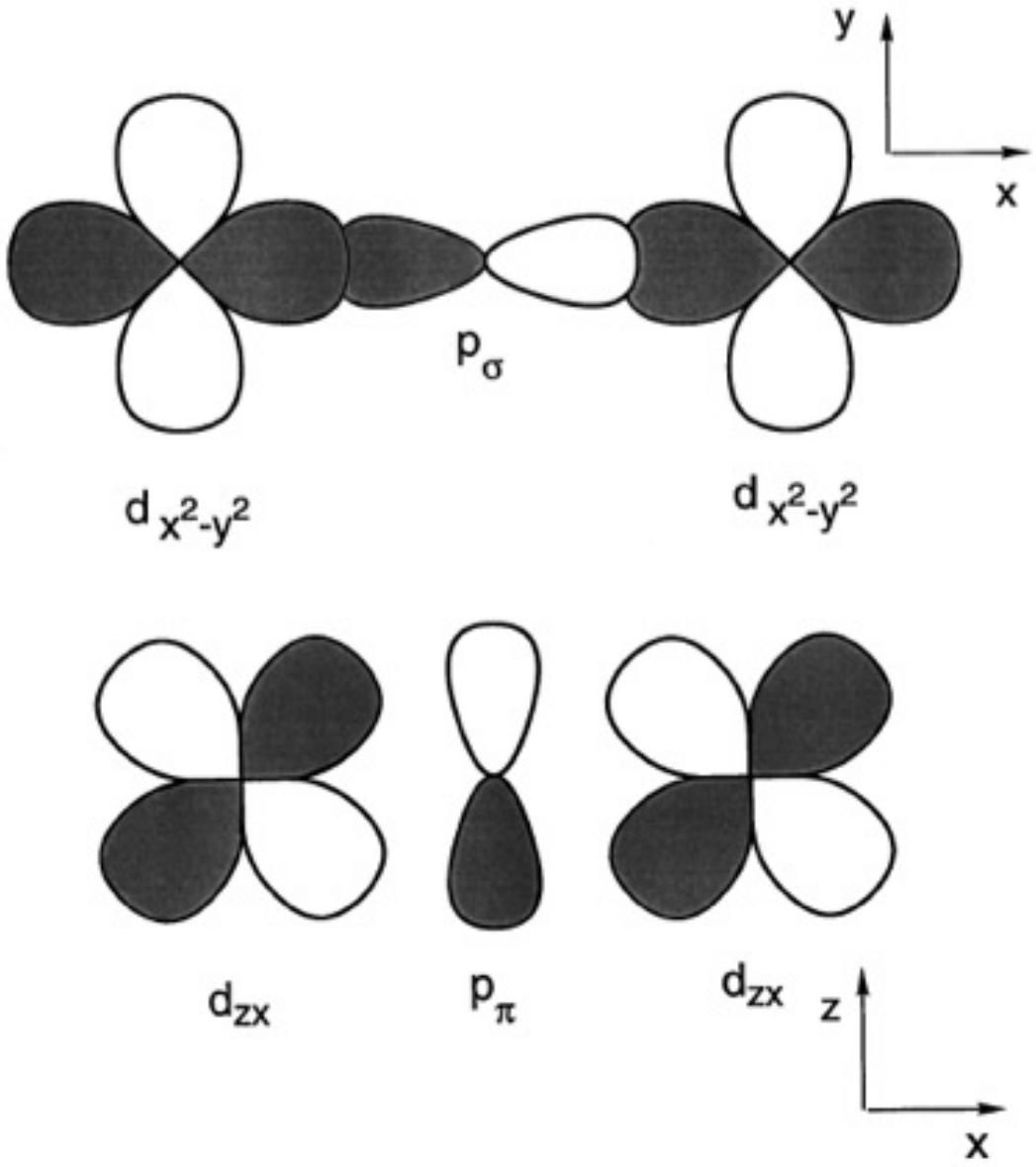

Figure 3.2: Configuration for transition-metal $3d$ orbitals which are bridged by ligand p orbitals. [1].

electron bands are formed by the overlap of atomic orbitals in a periodic lattice. It is also noticed that insulators with a small energy gap are regarded as semiconductors due to thermal excitation of electrons [1].

However, there is another kind of insulators that have partially filled orbitals. Their insulating nature is caused by the electron-electron Coulomb repulsion at the same atomic sites, generally called electron correlation. This kind of insulators is called Mott-insualtor. Mott insulators are a class of materials that are expected to conduct electricity under conventional band theory, but which in fact turn out to be insulators when measured. This effect is due to electron-electron interactions which are not considered in the formulation of conventional band theory. Mott insulators are usually found in transition metal oxides with partially filled d-electron orbitals [2], since d-orbitals are more localized and have strong Coulomb repulsion. One classical example is the NiO, which has a half filled outermost orbital but is a very good insulator.

The understanding of strongly correlated systems has been a big challenge for condensed matter physics for a long time. In addition to the Mott insulating phase, the more challenging subject is how to describe the metallic phase near the Mott transition, which often display some interesting phenomena, such as high T_c superconductivity, colossal magnetoresistance. The fluctuations of spin, charge, and orbital correlation are strong and sometime critically enhanced near MIT in the metallic region. The Hubbard model [3, 4] was developed to understand this kind of properties.

The second quantized expression of the Hubbard model is given by:

$$H_H = H_t + H_U - \mu N \tag{3.1}$$

where

$$H_t = -t \sum_{<ij>} (c^{\dagger}_{i\sigma} c_{j\sigma} + h.c.) \tag{3.2}$$

$$H_U = U \sum_{i} (n_{i\uparrow} - 1/2)(n_{i\downarrow} - 1/2) \tag{3.3}$$

$$N = \sum_{i,\sigma} n_{i\sigma} \tag{3.4}$$

t= transfer amplitude, and U = Coulomb potential

In the Hubbard model, the electron correlation strength U/t and band filling parameter n are important. The schematic phase diagram is shown in Fig. 3.3.

3.3.1 Orbital selective Mott transition

The strongly correlated multi-orbital electron systems are among the most interesting topics in condensed matter physics. The addition of orbital to localized spin degrees of freedom leads to various remarkable phenomena such as maganite $La_{1-x}Sr_xMnO_3$ [5] and the ruthenates Sr_2RuO_4 [2] where interesting phenomena such as colossal magnetoresistance [1] and triplet pairing superconductivity [7, 8] were observed. Furthermore, the substitution of Ca for Sr in Sr_2RuO_4 compound provides an exotic phase diagram including showing a band-width controlled Mott transition [9].

The charge, spin, orbital and lattice are the main factors of the physics in transition metal oxides. The interplay and competition among them are the key points to

understand interesting physical properties in transition metal oxides. On the other hand, the Mott transition plays an important role in understanding correlation effects in solid states [1]. One of the important issues in the study of the Mott transition is whether the Mott transition in realistic materials is purely interaction driven or orbital and lattice degree of freedom also play some role [10]. Most of the realistic materials which undergo Mott transition have more than one active orbital [1, 6]. The orbital selective Mot transition (OSMT) is a very important feature for the Mott transition in a multi-orbital system. It was first proposed by Anisimov in the study of $Ca_{2-x}Sr_xRuO_4$ [4, 6, 9, 14]. According to Anisimov et al. [6], which is based on a non-crossing approximation calculation within dynamical mean field theory (DMFT), that the valence electron distribution becomes (3, 1) at $x_c = 0.5$. They further proposed that one of the α and β bands hosts two of the three electrons and is thus completely filled and band-insulating while the other, half-filled band becomes Mott localized with spin-1/2 local moment due to the narrow bandwidth relative to the Coulomb energy (Hubbard U). The half-filled γ band, howerver, remains itinerant due to its wider bandwidth, resulting in a metallic phase consistent with transport experiment.

The orbital degree of freedom is involved in the OSMT and the Mott transition in different orbitals happens individually because of the lifting of orbital degeneracy. In a crystal, basically there are two origins which can induce the asymmetry in the orbital space. The first one is the breaking of the local rotational symmetry in the crystal,

which makes different orbits pointing along different direction have different band width. The second one is the crystal field splitting generated by lattice distortion, which removes the degeneracy of the energy levels. A two-band generalized Hubbard model with half filling has been proposed to study the basic features of OSMT. Most of the studies on this two-band model using dynamical mean field theory reach the following common conclusions: (i) The OSMT is induced by the band width asymmetry of the different orbits. The crystal field splitting will reduce rather than enhance the tendency to OSMT. (ii) The orbitally selective Mott Phase (OSMP), in which one orbit is already localized while the other one keeps itinerary, will be greatly enhanced when the symmetry of the local interaction is lowered by including the Hund's rule coupling.

Although the two-band model has been extensively studied in the recent years, it may not be directly applied to the situation of $Ca_{2-x}Sr_xRuO_4$, because the effective model here is three-band model with four total electrons [6,30]. The most interesting feature of the OSMT in this system is that the OSMT will be accompanied by the change of orbital polarization. Before reaching OSMT, as predicted by LDA calculation and confirmed by ARPES [4,30], the four electrons in $Ca_{2-x}Sr_xRuO_4$ are almost evenly distributed among the three t_{2g} orbitals. Therefore, the average occupation number of each orbital is 4/3 before the OSMT. In order to have OSMT, 1/3 of electron has to be moved from the localized orbital to the non-localized ones. Thus the OSMT is always accompanied by the charge redistribution or the charge of orbital po-

larization. Since the crystal field splitting strongly couples to the orbital polarization, it will play a very important role in the OSMT for the three-band model [17].

3.4 $Ca_{2-x}Sr_xRuO_4$ and metal-insulator transition

One of the fundamental problems of many-body interactions in condensed matter physics is a metal-insulator transition under Coulomb interaction. $Ca_{2-x}Sr_xRuO_4$ provides a good example in understanding the metal-insulator transition in an iso-electronic multi-band system. The system changes from a Mott-insulator, $Ca_{2-x}RuO_4$, to a unconventional p-wave superconductor, Sr_2RuO_4, and has other interesting phases in between as shown in Fig. 3.2(a) and (b). Studies of $Ca_{2-x}Sr_xRuO_4$ help us to understand the unconventional superconductivity in Sr_2RuO_4, Mott insulator and Mott transition.

$Ca_{2-x}Sr_xRuO_4$ is a bandwidth control system. The systematic phase diagram in the plane of U/t versus filling δ is shown in Fig. 3.3. The metal-insulator transition is realized by the control of the bandwidth instead of the electron filling.

3.4.1 Phase diagram of $Ca_{2-x}Sr_xRuO_4$

Sr_2RuO_4 is a p-wave superconductor which shows a metallic normal state. Substituting isovalent Ca^{2+} ion in place of Sr^{2+} , $Ca_{2-x}Sr_xRuO_4$ develops a rich phase diagram which is shown in Fig. 5.9(a) and (b). The rotation and tilting of RuO_6 octahedra is shown in Fig. 5.9(c)-(f).

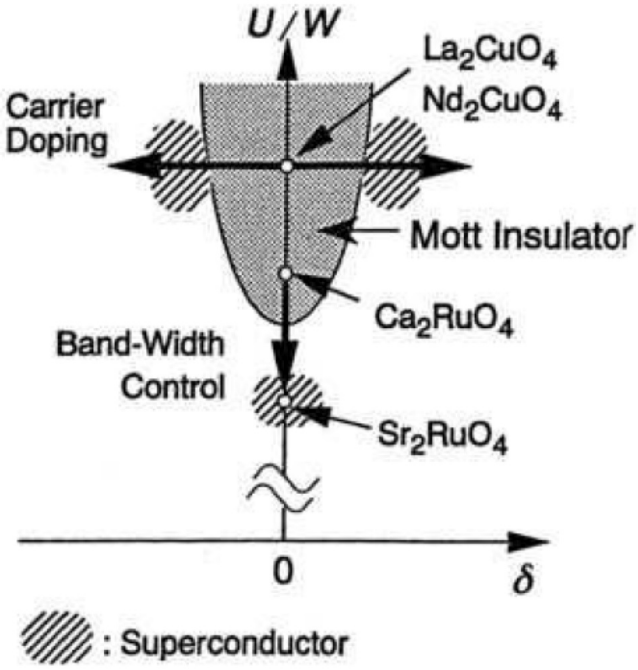

Figure 3.3: Schematic phase diagram in the plane of the correlation U/t and the filling derivative δ from integer. The horizontal arrows indicate the carrier doping route and the vertical one is the band width control route.

The phase diagram is divided into three regions, which are called as region I ($0 < x < 0.2$), region II ($0.2 < x < 0.5$) and region III ($0.5 < x < 2$).

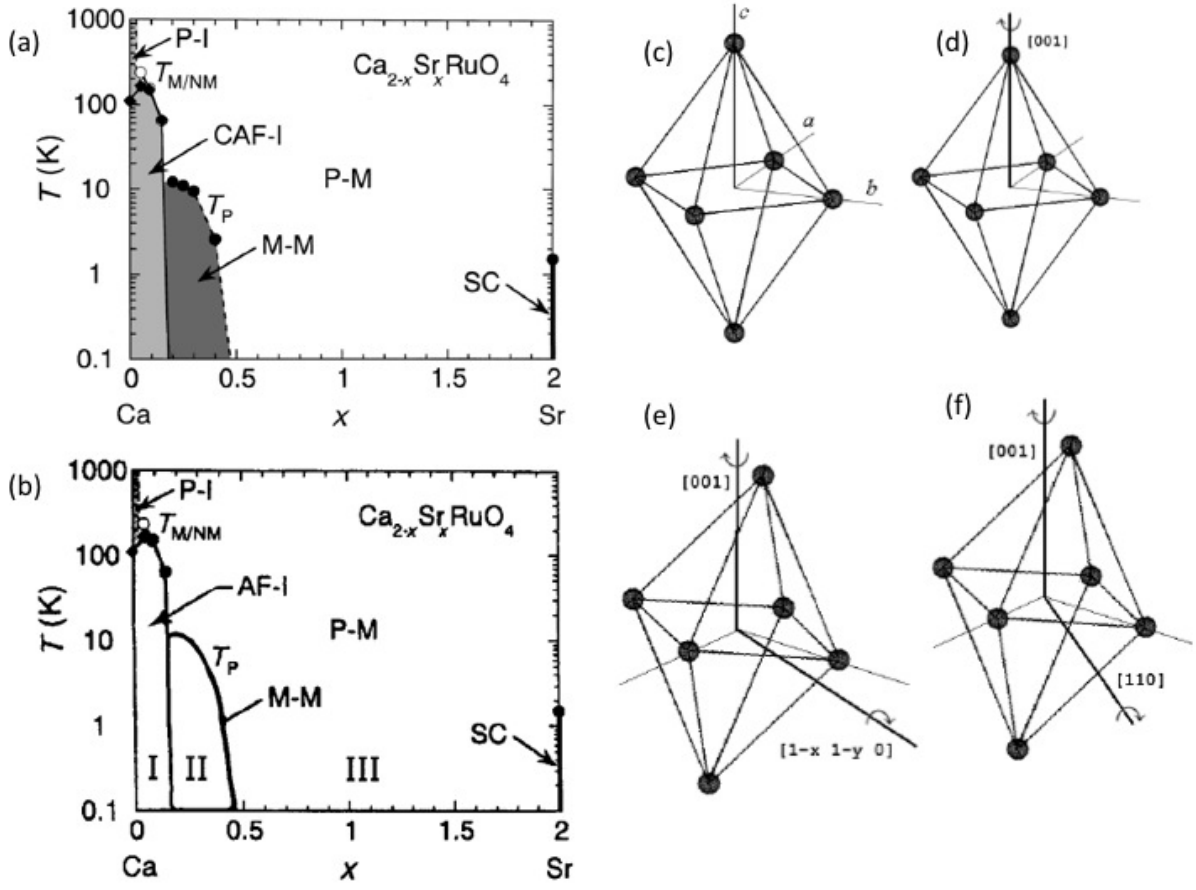

Figure 3.4: (a) and (b) Phase diagram of $Ca_{2-x}Sr_xRuO_4$ taken from [9]. (c)-(f) plots showing rotation and tilting of the RuO_6 octahedra at x =0, 0.2, 0.5, 2 respectively [6].

Region III ($0.5 < x < 2$): In this region, the system is basically a paramagnetic metal. It is clear from experiments that the superconductivity is quickly suppressed when Sr is substituted by Ca in Sr_2RuO_4. This is believed to be a natural consequence of disorder in a *d*-wave superconductor. In this region, the crystal structure of the

system starts to change. Sr_2RuO_4 has an undistorted K_2NiF_4 structure with $I4/mmm$ space group at low temperatures. After x=1.5, this structure becomes unstable, and RuO_6 octrahedra start to rotate around c-axis with $I4_1/acd$ space group. At x =1.5, only diffusive scattering representative of short range rotation is present.

The value of $x_c = 0.5$ is a critical value, separating a metallic and orbitally ordered phase with antiferromagnetic spin correlation ($x < x_c$) from the paramagnetic metal for $x > x_c$. In this case, one observes $\theta_{cw} \approx 0$ for $x \approx x_c$ and magnetic moment takes a value of $S = 1/2$. This value is quite distinct from the value of $S = 1$ in Ca_2RuO_4 - the expected value for a localized Ru^{4+}-ion with 2 holes in the t_{2tg}-subshell. In addition, alloys with $x \approx x_c$ are metallic, not insulating.

Region II (0.2 < x < 0.5): The system is a magnetic metal at low temperatures in this region. The Neel temperature is about the order of 10 K. At low temperatures, there is a transition between non-magnetic and magnetic metal. The RuO_6 octrahedron starts to tilt in this region. Around $x = 0.5$, a combination of rotation and small tilt is found. This structure is called "tilt phase", which is either a subgroup of $I4_1/acd$ or $Pbca$. The tilt angle increases with decreasing Sr concentration. At x =0.2, a tilt angle of about 7^o is found.

Region I (0 < x < 0.2): In this region,the system is an antiferromagnetic insulator at low temperatures. The system changes from magnetic metal to an AFM insulator upon reducing the Sr concentration beyound $x = 0.1$. It becomes a bad metal at high temperatures. Either by changing doping or temperature, the metal-

insulator transition can be achieved. There is also structural transition at this region. At low temperatures, its structure is a small c lattice parameter $S - Pbca$ structure. Upon increasing temperature, the structure changes to a large c lattice parameter $L - Pbca$ structure. The transition between the $S - Pbca$ and $L - Pbca$ is first order structural transition. The tilting angle also increases.

3.4.2 Transport properties of $Ca_{2-x}Sr_xRuO_4$

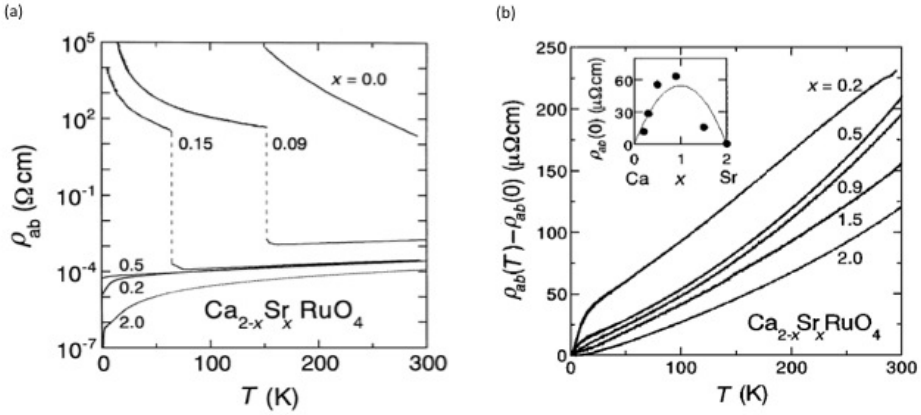

Figure 3.5: (a) Temperature dependence of the in-plane resistivity, ρ_{ab}(T), for $Ca_{2-x}Sr_xRuO_4$ with different values of x. (b) ρ_{ab}(T) subtracted by the zero temperature residual resistivity $\rho_{ab}(0)$. The inset is $\rho_{ab}(0)$ with fit by the Nordheim law $Ax(x-2)$.

Resistivity Measurement: The resistivity (ρ_{ab} and ρ_c) of $Ca_{2-x}Sr_xRuO_4$ shows a strong Ca substitution dependence as illustrated in Fig. 3.5. In region I, Ca_2RuO_4 is non-metallic at all temperatures. The metal-non metal transition for $x = 0.09$ and

0.15 is achieved at $T_{M/NM} \simeq 155$K and 70 K, respectively. The resistivity changes abruptly by a factor more than 10^4 at $T_{M/NM}$. At $x = 0.15$, the resistivity data below transition temperature $T_{M/NM}$ can be fit well by $\rho_{ab}(T) = A \exp(T_o/T)^{1/4}$, which suggests that localization dominates the non-metallic behavior.

In region II and III, ρ_{ab} curves show metalic ($d\rho/dt > 0$) behavior. $\rho_{ab}(T)$-$\rho_{ab}(0)$ increases quite systematically with Ca substitution. The residual resistivity $\rho_{ab}(0)$ has a peak around x =1.0, which is consistent with Nordieim formula $Ax(2-x)$, as shown in inset of Fig. 3.5(b).

The out-of plane resistivity $\rho_c(T)$ is less temperature dependent and even non-metallic. In order to show the temperature dependence clearly, the c-axis resistivity is normalized by the value at 300 K shown in Fig. 3.6. In region I, the $\rho_c(T)$ is metallic near to the M-NM transition temperature at 70 K. However, in the region II, a clear change from non-metallic to metallic is observed upon lowing temperature.

Susceptibility Measurement: In the metallic regions (II and III), the susceptibility $\chi(T) = M/H$, shows systematic variations with x at a low magnetic field. In Fig. 3.7(a) and (b), the in-plane susceptibility $\chi_{ab}(T)$ curves for single crystal samples are shown for region II and III, respectively. The insets of Fig. 3.7(b) are the inverse susceptibility measured by polycrystalline samples.

In order to study the evolution of the temperature dependence of susceptibility,

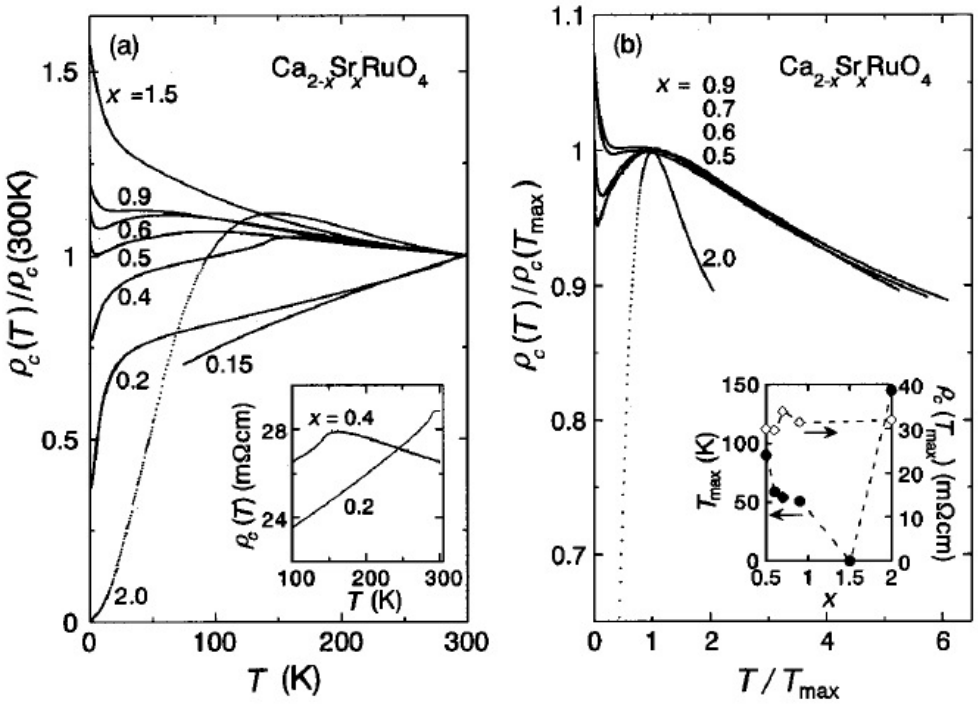

Figure 3.6: (a) Temperature dependence of the out-of-plane resistivity, ρ_c(T) normalized by the values at 300 K for $Ca_{2-x}Sr_xRuO_4$ with different values of x. For x =0.15, the data are shown only above the M-NM transition point of 70 K. The inset illustrates the crossover at T_o for x =0.2 and 0.4 (b) The variation of ρ_c(T)/ρ_c(T_{max}) against T/T_{max} for several values of x in region III. The inset displays the x dependence of T_{max} (solid circle) and ρ_c(T_{max}) (open diamond).

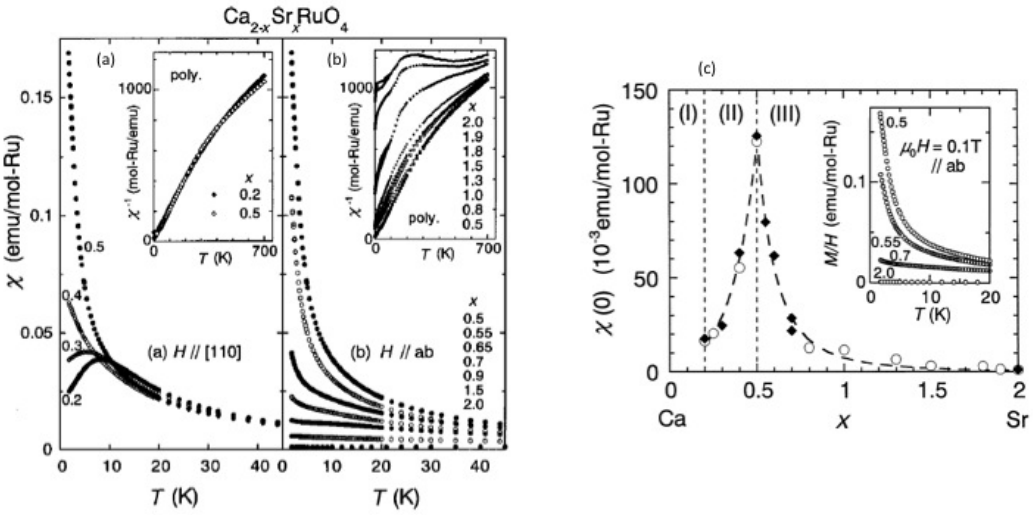

Figure 3.7: Temperature dependence of the in-plane susceptibility for $Ca_{2-x}Sr_xRuO_4$ with different values of x (a) in region II for the [110] component and (b) in region III. For both regions, the zero field-cooled (ZFC) and field-cooled (FC) curves agree very well. The insets for (a) and (b) display the inverse susceptibility of polycrystalline samples in regions II and III, respectively. (c) $\chi(0)$ at 2.0 K vs Sr concentration in regions II and III.

the Curie-Weiss analysis is used. The data can be fitted by

$$\chi = \chi_o + \frac{C}{T - \Theta_w} \tag{3.5}$$

Here χ_o is a temperature-independence term, C is the Curie constant, and Θ_w is the Weiss temperature. The effective Bohr magneton P_{eff} was derived from the formula

$$C = \frac{N_A P_{eff}^2 \mu_B^2}{3K_B} \tag{3.6}$$

where N_A, μ_B and K_B are Avogadro's number, the Bohr magneton and Boltzmann's constant, respectively.

All the data in region II and III can be fitted well by the formula. Figure 3.7(c) illustrates doping dependence of the in-plane susceptibility at low temperatures. When the Sr concentration is decreased from Sr_2RuO_4, $\chi(0)$ increases and reaches at a maximum at $x = 0.5$. This maximum value is about 100 times larger than that of Sr_2RuO_4. Then it decreases upon further decreasing of x value. The maximum of susceptibility in region III ($x \to 0.5$) is believed to be due to the increase of FM spin fluctuations. The decrease is due to the competition between the FM and the AFM state. The system reaches an AFM state when x approaches 0.2.

Field dependence of the magnetization: Figure 3.8 shows the field dependence of M and the longitudinal magnetoreistance at 0.6 K. As B increases, M shows a stepwise increase at $B_{cr} = 2.3$ and 6 T for its ab-plane and c-axis components, respectively. These metamagnetic transitions should be due to the field destabilization

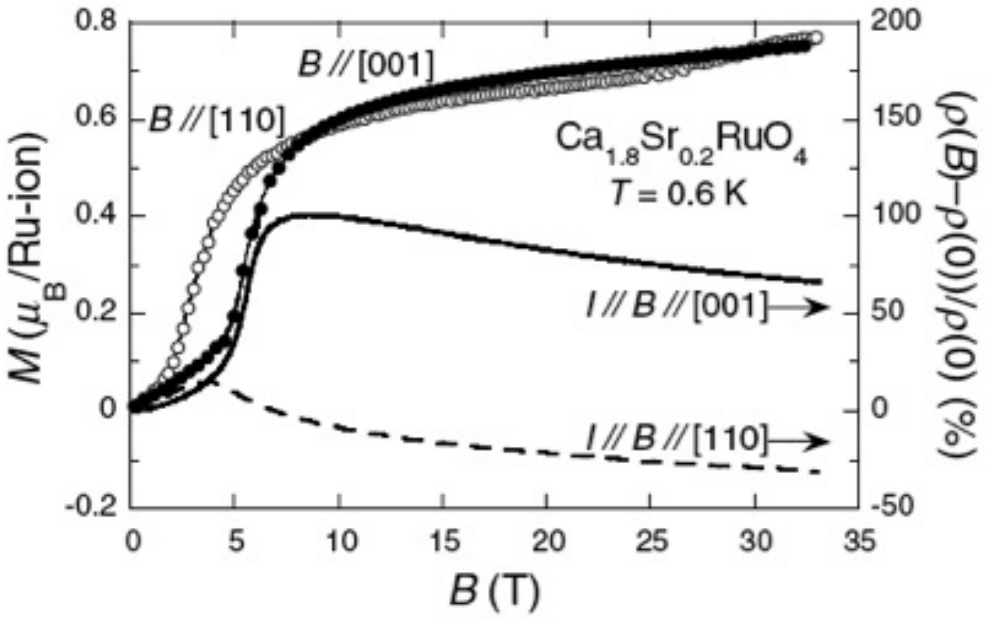

Figure 3.8: Field dependence of the magnetization and longitudinal magnetoresistance at 0.6 K for $Ca_{1.8}Sr_{0.2}RuO_4$ taken from reference [18].

of the AF coupling. At the heighest fields, both components show a tendency to saturate around $0.8\mu_B$. For the Ru^{4+} state, the moment is expected to increase up to a saturation value of 2 μ_B. until a half-metallic state is achieved. It is important to note that the observed saturation moment is close to the effective magneton of 1 μ_B estimated from the Curie-Weiss analysis of $\chi(T)$. This suggests that the system at high fields is in an almost polarized FM state with a local moment of $S = 1/2$. Also, both the *ab*-plane and *c*-axis components of the magenetoresistence change their signs from positive to negative across B_{cr}, which is consistent with a change in the spin coupling from AF to FM.

In $Ca_{1.8}Sr_{0.2}RuO_4$, γ Fermi surface is absent at 1.5 electron occupancy [19]. It is possible for the γ complex to undergo the Mott transition and become localized in the doubled unit cell, contributing a spin-1/2 local moment. Since there are two Ru atoms per supercell, the localized magnetic moment is 0.5 μ_B per Ru atom. This is indeed consistent with the field dependent magnetization measurement as shown in Fig. 3.8. The sharp increase of the magnetization to 0.5 μ_B as the applied field reaches about 5 T can be attributed naturally to the polarization of the local moment, whereas the subsequent gradual growth of the magnetizaton with further increasing field arises from Pauli paramagnetism of the itinerant α and β band electrons.

Effective Bohr Magnetron: The systematic doping dependence (x) of the effective Bohr magneton P_{eff} extracted from the data in Fig. 3.7 is shown in Fig. 3.9. At x =0, *i.e.* for Ca_2RuO_4, the P_{eff} has the largest value with almost 80 % of the

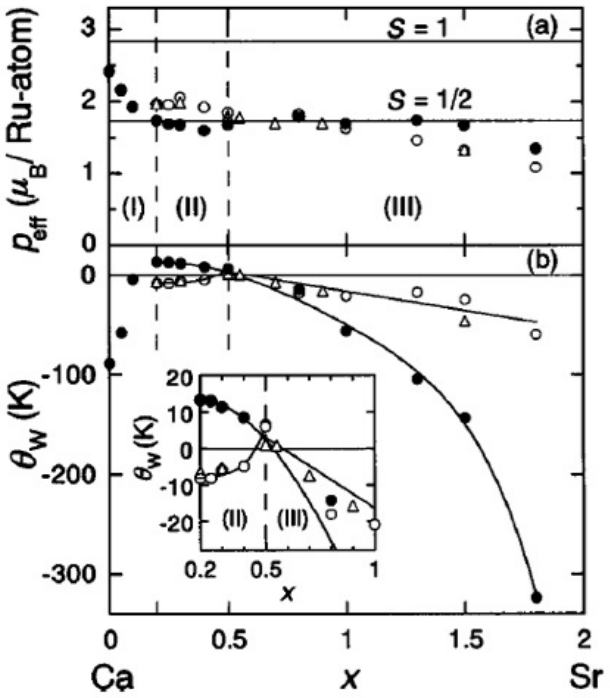

Figure 3.9: Curie-Weiss parameters against the Sr content x in $Ca_{2-x}Sr_xRuO_4$. The solid and open circles correspond to the results of polycrystalline samples for the high-temperature and the low temperature fitting regions, respectively. (a) the solid horizontal lines correspond to the effective Bohr magnetons with S =1/2 and 1. The inset in panel (b) is an enlarge figure for region II. The solid curves are guides to the eye.

expected value for S =1 configuration. As x increases, P_{eff} decreases rapidly in region I and becomes almost a constant for $0.2 \leq x \leq 1.5$ with a value that corresponds to S =1/2. The electronic states of S =1/2 are not fully understood yet. The extracted Weiss temperatures are shown in Fig 3.9(b). In the region III ($0.5 \leq$x ≤ 2), the Weiss temperatures (Θ_w) are negative. Θ_w increases with decreasing x and it approaches to zero when x approaches 0.5. However, the negative values of Θ_w in region III can be understood as the evolution of FM spin fluctuations according to the self-consistent renormalization theory.

When the system reaches region II, Θ_w shows two different kinds of behavior. The high temperature data show a positive Θ_w while the low temperature data and the single crystal data show a negative Θ_w . The negative Θ_w indicates an AFM interaction while the positive Θ_w indicates a FM interaction. There is a structural transition (T_o) which may cause a change in magnetic interactions. $Ca_{2-x}Sr_xRuO_4$ changes from a paramagnetic metal to a magnetic metal at the critical x value. The Weiss temperature Θ_w approaches zero. The phase transition occurs at $T = 0$, so the transition is a quantum transition at $x_c \sim 0.5$. This point is called quantum critical point.

Bibliography

[1] M. Imada *et al.*, Rev. Mod. Phys. **70**, 1039 (1998).

[2] R. Peierls, Proc. Phys. Soc. A, **49**, (1937).

[3] J. Hubbard, Proc. R. Soc. A, **277**, (1964).

[4] J. Hubbard, Proc. R. Soc. A, **281**, (1964).

[5] Y. Tokura *et al.*, J. Phys. Sco. Jpn **63**, 3931 (1994).

[6] Y. Maeno *et al.*, Nature **372**, 532 (1994).

[7] Y. Maeno *et al.*, Physics Today **54**, 42 (2001).

[8] A. P. Mackenzie *et al.*, Rev. Mod. Phys. **75**, 657 (2003).

[9] S. Nakatsuji *et al.*, Phys. Rev. Lett. **84**, 2666 (2000).

[10] S. Biermmann *et al.*, Phys. Rev. Lett. **94**, 026404 (2005).

[11] M. Capone *et al.*, SCIENCE **296**, 2364 (2002).

[12] V. Anisimov *et al.*, Eur. Phys. J. B. **25**, 191 (2002).

[13] G. Kotliar *et al.*, Phys. Rev. B **54**, R14221 (1996).

[14] J. S. Lee *et al.*, Phys. Rev. Lett. **96**, 057401 (2006).

[15] S.-C. Wang *et al.*, Phys. Rev. Lett. **93**, 177007 (2004).

[16] Z. Fang *et al.*, Phys. Rev. B **69**, 045116 (2004).

[17] X. Dai *et al.*, arXiv:0611075 (2006).

[18] S. Nakatsuji *et al.*, Phys. Rev. Lett. **90**, 137202 (2003).

[19] M. Neupane *et al.*, Phys. Rev. Lett. **103**, 097001 (2009).

Chapter 4

Observation of a novel orbital-selective Mott transition in $Ca_{1.8}Sr_{0.2}RuO_4$

4.1 Introduction

$Ca_{2-x}Sr_xRuO_4$ is a fascinating $4d$ multi-orbital system that exhibits a rich and intricate phase diagram, ranging from a chiral p-wave superconductor (Sr_2RuO_4) to a Mott insulator (Ca_2RuO_4) [2, 3]. Similarly to the high-T_c cuprates, the metal-insulator transition under the influence of electron correlations in the ruthenates is of fundamental importance and currently under intensive debate. There is accumulating experimental evidence for the coexistence of local moments and metallic transport,

and heavy fermion behavior in the region of $0.2 \leq x \leq 0.5$ [3–5], which is remarkable because there are no f-electrons in this material. To account for the coexistence of localized and itinerant electrons in this region, the scenario of orbital selective Mott transition has been proposed [6,7] as the following: Sr_2RuO_4 has three degenerate t_{2g} orbitals (d_{xy}, d_{yz}, and d_{zx}) occupied by four $4d$ electrons. The isovalent Ca substitute does not change the total carrier concentration (i.e. no doping), but rather increases the effective electron correlation strength (U_{eff}) relative to the reduced bandwidth which is induced by structural change due to the smaller ion radius of Ca^{2+}. Consequently, it is possible that an OSMT takes place in the narrower bands, i.e., the one-dimensional (1D) d_{yz} and d_{zx} orbitals, where electrons undergo a Mott transition and become localized, while the electrons in the wider two-dimensional (2D) d_{xy} band remain itinerant. A similar partial localization mechanism has been proposed for some heavy fermion materials, e. g., UPd_2Al_3 [8].

While the concept of OSMT is of critical importance to the multi-orbital Mott Hubbard systems and has been studied extensively in theory [6, 7, 9–11], it has not been confirmed experimentally. Our previous ARPES study [12] shows that, for samples with $x = 0.5$, the two 1D (α and β) Fermi surface sheets are clearly "visible" as well as that of 2D (γ) FS, although the latter is considerably smeared and weaker in comparison to the case of Sr_2RuO_4. This is in sharp contrast to the OSMT prediction that the 1D FS sheets become Mott localized.

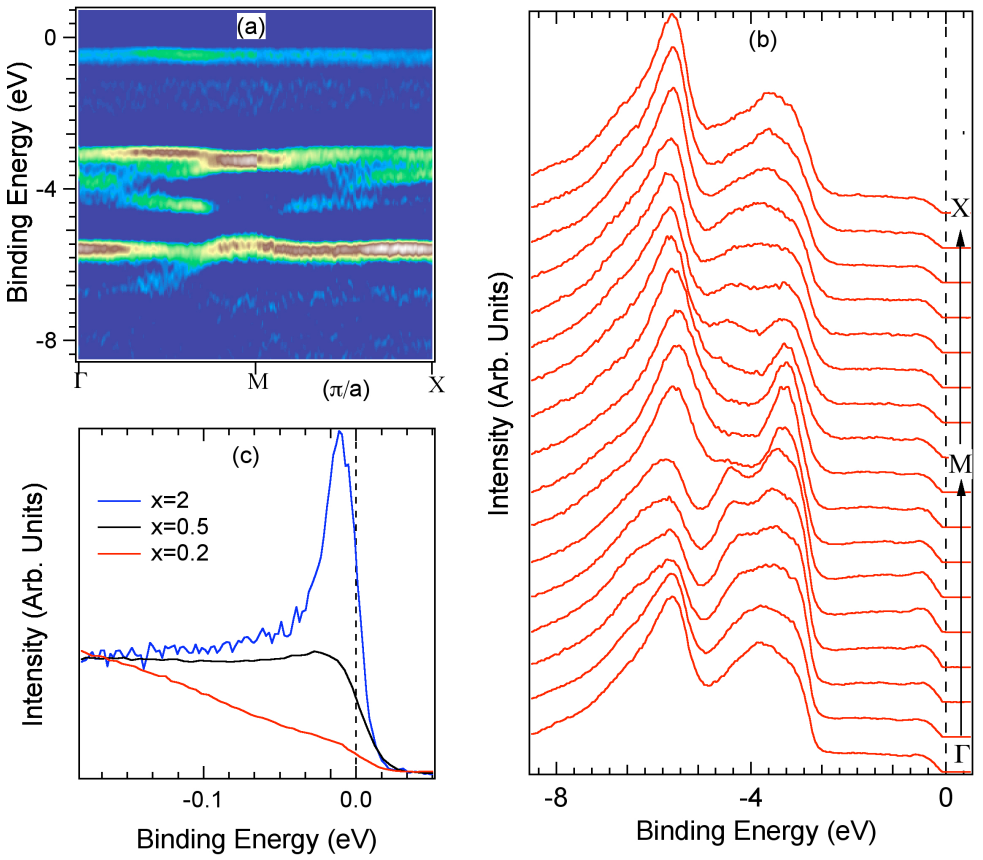

Figure 4.1: The valence band of $Ca_{1.8}Sr_{0.2}RuO_4$. (a) Plot of second derivative of ARPES intensity for the valence band of $Ca_{1.8}Sr_{0.2}RuO_4$ taken along Γ-M-X ($h\nu$ = 75 eV, T = 40 K). (b) The corresponding EDCs along Γ-M-X. (c) Comparison of the EDCs for x = 0.2, 0.5, 2, taken at the β band crossing point along Γ-M ($h\nu$ = 32 eV, T = 40 K).

4.2 Experimental method

To check if the OSMT occurs at a lower Sr concentration, we have conducted a series of ARPES experiments [1] on high-quality single crystals at $x = 0.2$, grown by the floating zone technique [5]. All of our experiments have been performed at high-flux synchrotron undulator beam lines (e.g., Wadsworth, U1-NIM, PGM at the Synchrotron Radiation Center, Wisconsin), using a high-efficiency Scienta SES-2002 electron analyzer. The energy and momentum resolutions are 10 - 30 meV and 0.02 Å^{-1}, respectively. Samples were cleaved *in situ* and measured at 40 K in a vacuum better than 1 x 10^{-10} torr. The samples have been found to be very stable and without degradation for the typical measurement period of 48 hours. Precise determination of the low-energy electronic structure at this doping level is important since $Ca_{1.8}Sr_{0.2}RuO_4$ is at the boundary between a magnetic metal and an antiferromagnetic insulator, and exhibits non-Fermi liquid behaviors in the resistivity [3]. However, it is a rather difficult and lengthy experiment due to a much reduced ARPES spectral intensity in the vicinity of the Fermi energy (E_F) near the insulating phase. Several techniques have been used to boost photoelectron signals, including enhancement of the APRES matrix elements through fine tuning of photon energy and measurements at different Brillouin zones (BZs).

4.3 Sample quality

The ARPES intensity of $Ca_{1.8}Sr_{0.2}RuO_4$ sample is very weak because it is at the border of insulating and metallic phase. We have done the following measurement to make sure that the quality of the sample is good:

I. Valence band measurement: As shown in Fig. 4.1(a) and (b), strong spectral intensity and clear dispersion similar to the case of Sr_2RuO_4 are observed in the valence band of $Ca_{1.8}Sr_{0.2}RuO_4$, indicating good quality of sample and surface. However, the spectral intensity near E_F experiences dramatic reductions as the Sr content x approaches 0.2, as demonstrated in Fig. 4.1c, reflecting the fact that the system is near an insulating phase.

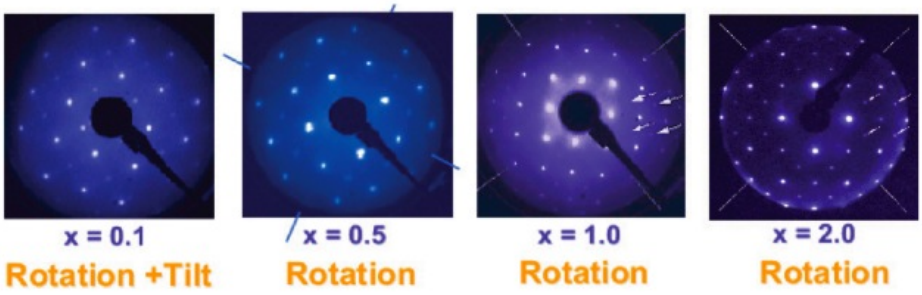

Figure 4.2: LEED patterns of of $Ca_{2-x}Sr_xRuO_4$ at different Sr levels (x= 0.1, 0.5, 1.0 and 2) show the rotation of RuO_6 octahedra.

II. LEED patterns of sample surface: $Ca_{1.8}Sr_{0.2}RuO_4$ is easy to cleave and usually has a good (001) surface. It exhibits a clear LEED pattern for cleaved surfaces. Figure 4.2 shows LEED pictures for different Sr concentrations from the reference [21].

The brighter LEED spots form a square lattice corresponding to the 2-dimensional RuO_2 lattice. The additional faint sports, which appear in the middle of the four bright spots, are caused by the rotation of the RuO_6 octahedra along the c-axis. This rotation is known to exist in the bulk of $Ca_{2-x}Sr_xRuO_4$ when x $\leq$ 1.5. The typical LEED pattern of $Ca_{1.8}Sr_{0.2}RuO_4$ measured during our ARPES experiments is almost identical to the one shown above for $Ca_{1.9}Sr_{0.1}RuO_4$, indicating the good quality of the sample surface.

III. Laue pictures of samples:

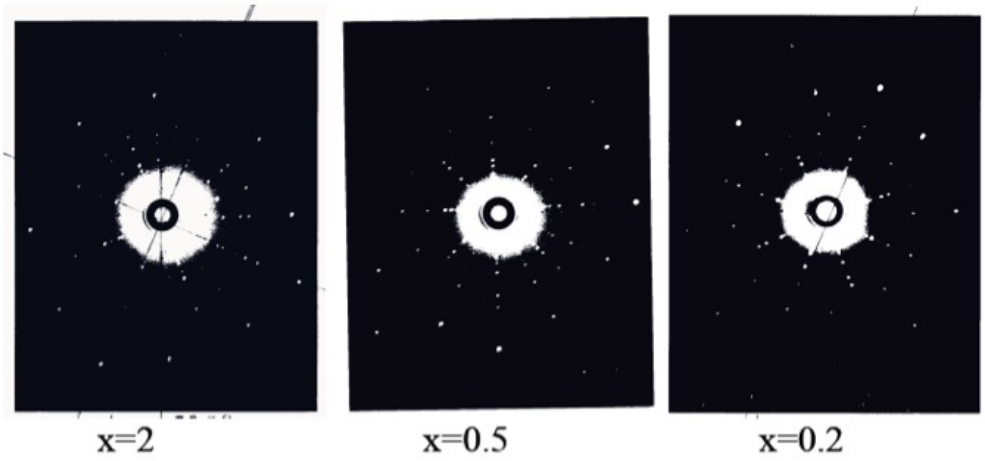

Figure 4.3: Laue pictures of of of $Ca_{2-x}Sr_xRuO_4$ at x= 2, 0.5, 0.2

Figure 4.3 shows some of the Laue pictures for three doping levels that show clear atomic patterns indicating good sample quality. The spots on Laue picture for $Ca_{1.8}Sr_{0.2}RuO_4$ are as sharp as pristine Sr_2RuO_4, indicating that single crystals are of high quality at this doping level.

IV. Direct comparison of APRES spectra between $Ca_{1.8}Sr_{0.2}RuO_4$ and Sr_2RuO_4:

Figure 4.4 shows ARPES intensity plots and the corresponding second derivative plots along a cut parallel to Γ-X (a few degrees off Γ-X). The first cut is for $Ca_{1.8}Sr_{0.2}RuO_4$, which clearly shows the α, β and α bands. However, there is no sign of the γ band. The second cut is for Sr_2RuO_4, which was measured in almost identical experimental conditions, clearly revealing three bands close to the X point. Note that the γ band is the strongest in Sr_2RuO_4.

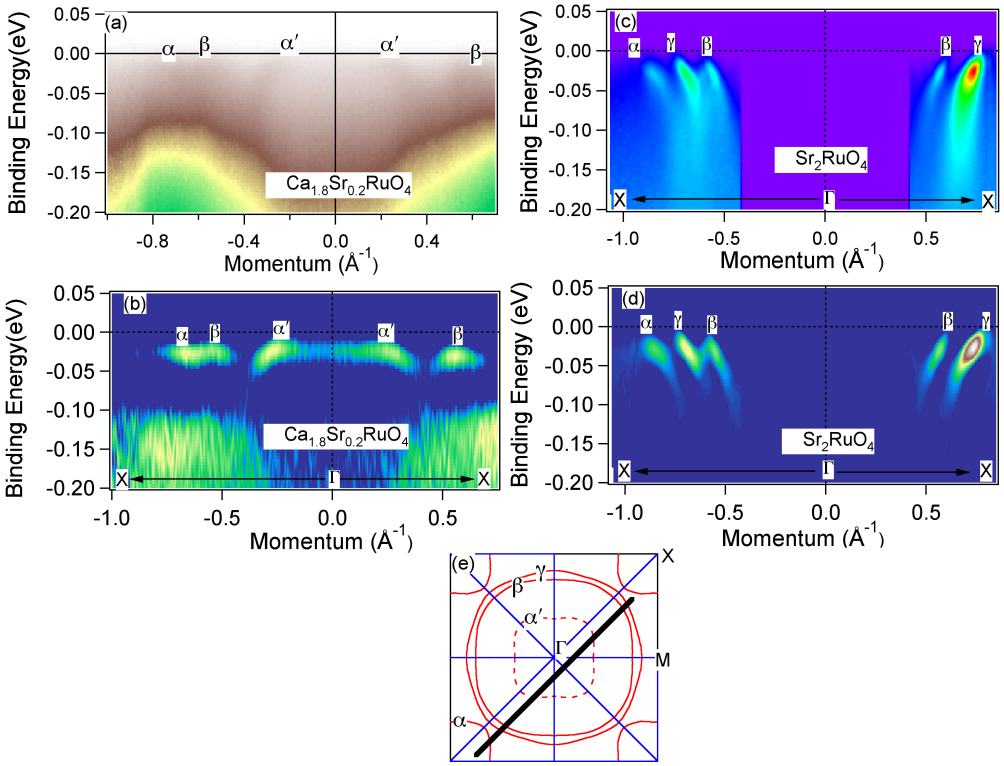

Figure 4.4: Comparison of ARPES intensity plots (a and c) and second derivative plots (b and d) along a long cut parallel to the Γ-X direction (the black line shown in panel e) between $Ca_{1.8}Sr_{0.2}RuO_4$ and Sr_2RuO_4.

4.4 ARPES results and discussions

To see clearly the low-energy excitations, we zoom in to the binding energy range within 0.2 eV to E_F, as plotted in Fig. 4.5. One can identify weak but discernible peaks dispersing towards to E_F, as shown in Figs. 4.5c and d. Unlike Sr_2RuO_4, which has Fermi liquid-like quasiparticle (QP) peaks [13], $Ca_{1.8}Sr_{0.2}RuO_4$ has a much broader lineshape in its low-energy dispersion. As illustrated in Figs. 4.5a and b, we observe two linearly dispersive bands along the high-symmetry line X-Γ-X, or (π,π)-(0,0)-(-π,-π), crossing E_F around 0.3 and -0.9 $Å^{-1}$, respectively. These two Fermi crossing (k_F) points, plotted in Fig. 4.5f as points # 1 and 2, locate respectively on the calculated α FS for Sr_2RuO_4 and its folded FS (labeled as the α' FS) due to the $\sqrt{2} \times \sqrt{2}$ reconstruction caused by a rotation of the RuO_6 octahedra [14]. We note that the peak intensity in both energy distribution curves (EDCs) and momentum distribution curves (MDCs) diminishes as it approaches E_F or k_F, possibly due to a small energy gap or the QP decoherence effect observed in some transition metal oxides near the metal-insulator boundary [15]. The band dispersion along another high-symmetry line M-Γ-M is displayed in Fig. 4.5e, and we observed four FS crossings (points #3 - #6) whose locations are plotted in Fig. 4.5f. While the crossing points #4 and 5 are on the calculated α' FS, and #3 and 6 are close to the β FS with respect to the location and direction of dispersion as compared with $x = 0$ and 0.5, there is no observation of the dispersing γ band and the corresponding FS crossing.

To verify these band and FS assignments, we have performed many measurements

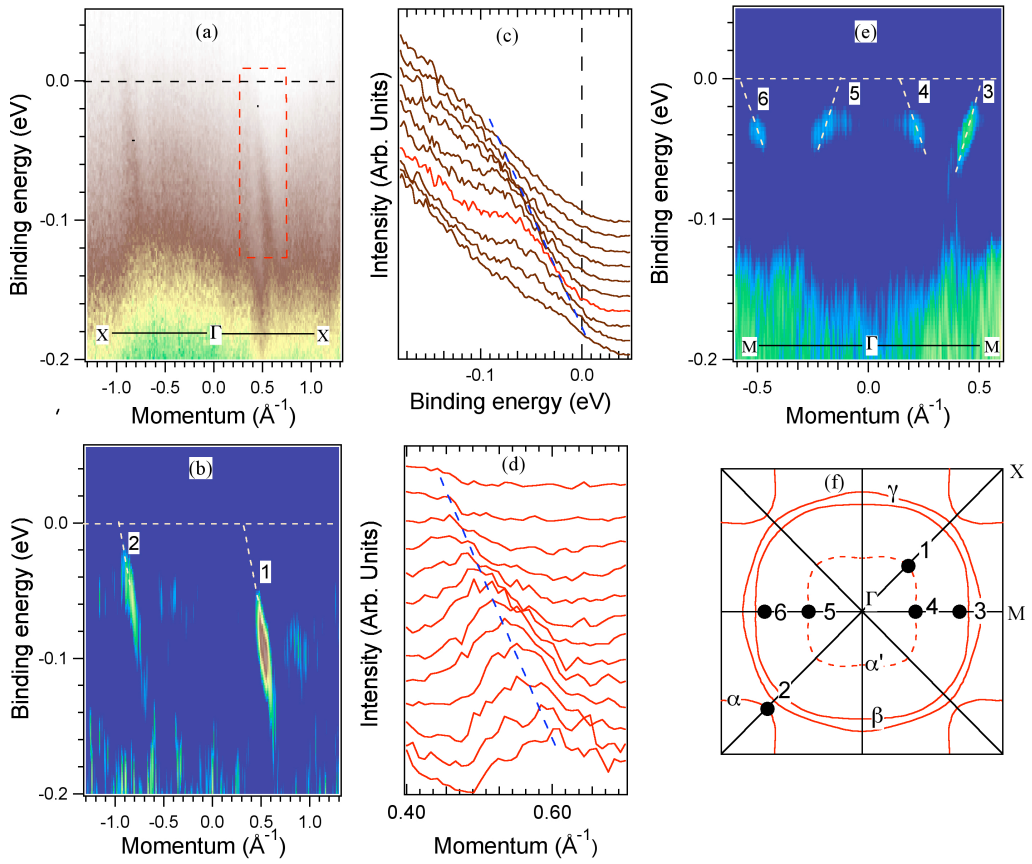

Figure 4.5: Band dispersion along high-symmetry directions in $Ca_{1.8}Sr_{0.2}RuO_4$. (a) ARPES intensity plot along X-Γ-X. (b) The corresponding second derivative plot of (a). The white dashed lines are guide for eyes. (c) EDCs, and (d) MDCs, within the red dashed box in (a), showing low-energy band dispersion, as indicated by blue dashed lines. (e) Second derivative plot of ARPES intensity along M-Γ-M. (f) Fermi crossings (black dots) indicated in (b) and (e), and Fermi surface sheets (red lines) calculated by LDA for Sr_2RuO_4 [17] in the first BZ.

to cover a wide range of k-space. We locate and plot all observed FS crossing points in the first BZ shown in Fig. 4.6a. The extracted k_F points from the dispersive bands indicted by dots are obtained from MDCs and EDCs. It is clear that both the α and β main FS sheets and the folded α' FS are present in $Ca_{1.8}Sr_{0.2}RuO_4$. However, no evidence of the γ FS is found. The disappearance of the γ FS is very puzzling. According to Luttinger counting theorem, the total occupied FS area should remain the same due to the isovalence nature of the Ca-Sr substitution. From the fitted α and β FS sheets, as shown in Fig. 4.6a, we derive the electron occupations $n_\alpha = 1.72$ and $n_\beta = 0.79$, implying that the γ band has 1.49 valence electrons since $n_{total} = 4$. To illustrate this point, we plot the "would be" γ FS in Fig. 4.6a as a simple circle (black dished line), which satisfies the Luttinger counting of 1.49 electrons. Note that it would almost touch the M (π, 0) point, indicating that its van Hove singularity is very close to the Fermi energy, which may lead to instability at low temperature.

To further understand the fate of the γ band, we plot in Fig. 4.6b an EDC of $Ca_{1.8}Sr_{0.2}RuO_4$ integrated over the neighboring region of M (indicated by a rectangular box around M in Fig. 4.6a). In contrast to the EDC of Sr_2RuO_4 at M, which is also plotted in Fig. 4.6b, the EDC of $Ca_{1.8}Sr_{0.2}RuO_4$ shows a dramatic suppression of the γ QPs. In fact, the spectrum consists of a broad feature with a gap of $\gtrsim 100$ meV, and a small "foot" extending toward E_F. The origin of this small "foot" is not entirely clear, although it may possibly come from a residual γ band from a minority phase, or certain impurity states. We regard the disappearance of the γ QP with a

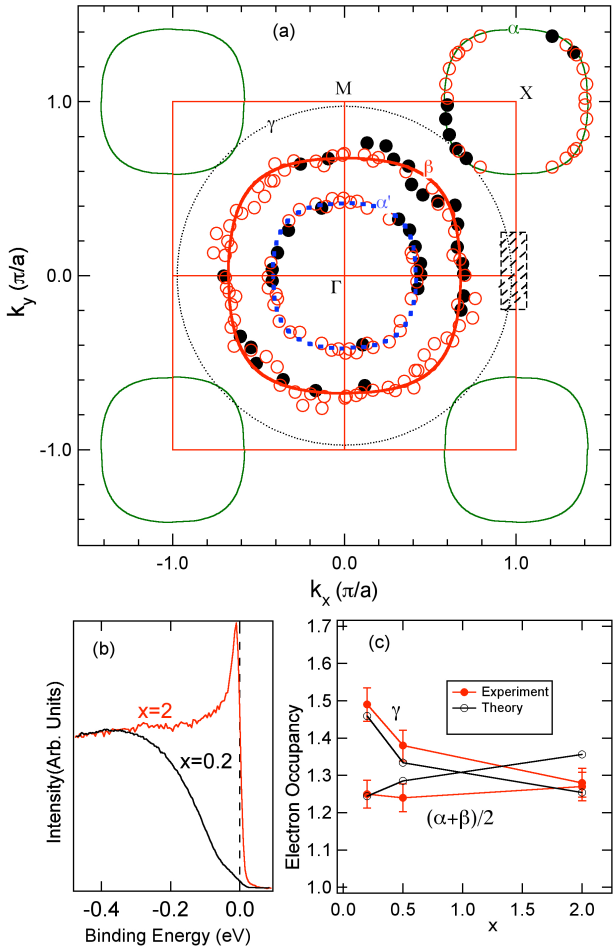

Figure 4.6: Fermi surface and electron occupancy of different orbitals. (a) Measured FS sheets of α (green contours centered at X), β (red contour centered at Γ), and the folded α (blue dashed contour centered at Γ), along with the Fermi crossing points determined by ARPES (black solid dots) and symmetrized points according to the 4-fold crystal symmetry (red open dots). The black dotted contour centered at Γ is the derived γ FS according to Luttinger theorem. (b) Comparison of the $(\pi, 0)$ EDCs between $Ca_{1.8}Sr_{0.2}RuO_4$ and Sr_2RuO_4, integrated over the k-region indicated by the shaded rectangle in (a). (c) The Sr content dependence of electron occupancy of γ and $(\alpha+\beta)/2$, obtained by ARPES (red dots and lines), and LDA (black dots and lines).

large soft gap as an evidence for possible localization of the γ band. We notice that the electron occupancy of the γ band is close to 1.5 (a half integer) from both the experimental derivation based on Luttinger theorem as discussed above, and our theoretical calculation using local density approximation (LDA), as shown in Fig. 4.6c. It is remarkable that the LDA calculation shows good agreement with the ARPES experimental observation. The basic reason for the increase of the γ electron occupation is that the increased hybridization between the t_{2g} and e_g orbitals, due to the increasing rotation and tilting of the octahedra at higher Ca content, pushes down the d_{xy} band [30]. The same effect has been also observed in a similar $4d$-electron system (Sr_2RhO_4) [16].

A natural question is why the FS and the coherent excitations from the γ band are absent at 1.5 electron occupancy. Remarkably, as the system undergoes the $\sqrt{2} \times \sqrt{2}$ reconstruction in the bulk [14], the γ band folds into two subbands by the superlattice potential, accompanied by the doubling of the unit cell. The folded γ bands in the reduced BZ host a total of 3 electrons. The lower subband is completely filled while the upper one is precisely at half-filling. It is thus possible for the γ-complex to undergo the Mott transition and become localized in the doubled unit cell, contributing a spin-1/2 local moment. Since there are two Ru atoms per supercell, the localized magnetic moment is 0.5 μ_B per Ru atom. This is indeed consistent with the field dependent magnetization measurement in $Ca_{1.8}Sr_{0.2}RuO_4$ [4]. The sharp increase of the magnetization to 0.5 μ_B as the applied magnetic field reaches about 5 T (shown

as in Fig. 3.8) can be attributed naturally to the polarization of the local moment, whereas the subsequent gradual growth of the magnetization with further increasing field arises from Pauli paramagnetism of the itinerant α and β band electrons.

4.5 Theoretical explanation

Theoretically, most of the model studies have focused on the two-band Hubbard model, where the OSMT is mainly controlled by the difference in the bandwidths [7,9]. The real situation in $Ca_{2-x}Sr_xRuO_4$ system is more complex. Due to the $\sqrt{2} \times \sqrt{2}$ super structure, there is a total of six bands occupied by eight electrons in the doubled unit cell. We have carried out first-principle calculations and found that the lower three bonding bands are fully occupied by six electrons. The remaining two electrons occupy the upper three anti-bonding bands. If there were no crystal field splitting, these two electrons would be almost evenly distributed among the upper three bands, corresponding to occupations $(2/3, 2/3, 2/3)$. However, the localized orbital must be filled by an odd integer number of electrons in an OSMT, which can be realized in $Ca_{2-x}Sr_xRuO_4$ only when the two electrons redistribute among the upper three bands to reach occupations $(1/2, 1/2, 1)$ due to the crystal field splitting. This is consistent with our ARPES measurements near $x = 0.2$. Indeed, our LDA calculation shows that, with the reduction of the Sr concentration x, the crystal field pulls down the γ band and transfers charge from the α, β bands to the γ band as shown in Fig. 4.6c. When the electron distribution reaches $(1/2, 1/2, 1)$, the three-band complex splits

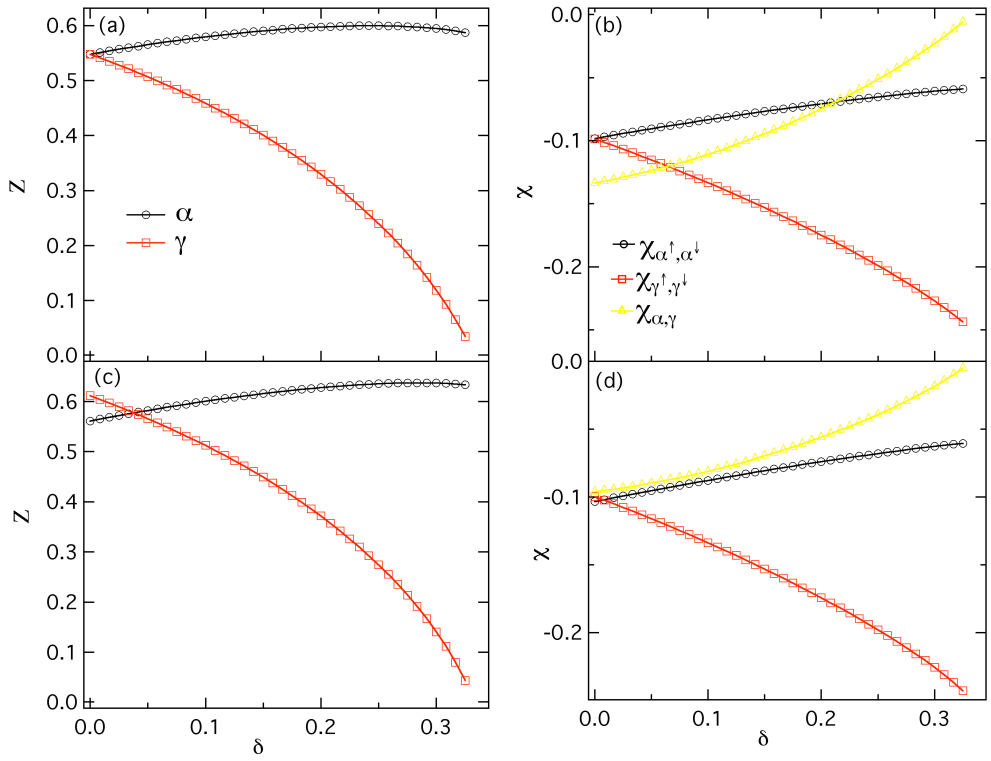

Figure 4.7: Calculations that show OSMT in multi-orbital systems (a) The QP weight for the 3-band Hubbard model with equal bandwidth W as a function of charge transfer δ defined by $(n_\alpha, n_\beta, n_\gamma) = (\frac{2}{3}\text{-}\frac{\delta}{2}, \frac{2}{3}\text{-}\frac{\delta}{2}, \frac{2}{3}\text{+}\delta)$. $U/W = 4.0$, J/W=1.0. (b) The intraband and interband correlation functions, where $\chi_{\alpha\uparrow,\alpha\downarrow} = \langle n_{\alpha\uparrow} n_{\alpha\downarrow}\rangle - \langle n_{\alpha\uparrow}\rangle\langle n_{\alpha\downarrow}\rangle$, $\chi_{\gamma\uparrow,\gamma\downarrow} = \langle n_{\gamma\uparrow} n_{\gamma\downarrow}\rangle - \langle n_{\gamma\uparrow}\rangle\langle n_{\gamma\downarrow}\rangle$ and $\chi_{\alpha,\gamma} = \langle (n_{\alpha\uparrow}+n_{\alpha\downarrow})(n_{\gamma\uparrow}+n_{\gamma\downarrow})\rangle - \langle (n_{\alpha\uparrow}+n_{\alpha\downarrow})\rangle\langle (n_{\gamma\uparrow}+n_{\gamma\downarrow})\rangle$. (c) Same as in (a), except for the three bandwidths of $W, W, 1.5W$. (d) Same as in (b), except for the three bandwidths of $W, W, 1.5W$. Note that the y-axis is negative in (b) and (d). With increasing δ, the intra γ-band correlation becomes large and negative, while the interband correlation approaches zero.

into two groups: two nearly degenerate α and β bands, and a separated γ band with a lowered center of gravity. Therefore, we have one two-band system and one single-band system, both with one electron per unit cell. The reason for the OSMT to take place in the γ band is that the critical interaction U_c for the Mott transition in a single band Hubbard model is about 30% smaller than that of a two-band model with one electron per unit cell and identical bandwidth, a result obtained by variational Gutzwiller and dynamical mean field theory [18,19]. The Hund's rule coupling further increases the critical U_c for the two-band system. Therefore, in a large area of the parameter space, the single γ-band system lies in the Mott phase contributing to the local moment, while the two-band system remains in the metallic phase contributing to the itinerant electrons.

To further illustrate this point, we apply the slave boson mean field theory to a simple three-band Hubbard model with the bandwidth ratios of 1:1:1 and 1:1:1.5 and two electrons per unit cell. The technical details have been explained in reference [20]. In Fig. 4.7, we plot the QP coherence weight (Z) and the orbital correlations as a function of the charge transfer δ. Fig. 4.7a clearly shows that the coherence weight of the γ band decreases continuously while that of the degenerate α band remains almost a constant as the OSMT is approached at charge transfer $\delta = 1/3$, which corresponds to the charge distribution $(1/2, 1/2, 1)$. Concomitantly, as can be seen from Fig. 4.7b, the interband correlations (χ) between the γ and the α, β bands are dramatically reduced. To verify that the bandwidth difference does not play an

important role in the OSMT, we show in Figs. 4.7c and d that the same conclusion is reached for the case where the γ band is 1.5 times as wide as that of the α and β bands.

4.6 Conclusions

In conclusion, we have successfully measured the low energy excitations in multi-orbital ruthenate $Ca_{2-x}Sr_xRuO_4$ near $x = 0.2$ by ARPES and unraveled a novel mechanism for the OSMT. The band dispersions and the associated FSs are observed for the d_{yz} and d_{zx} orbitals. In contrast, the d_{xy} orbital shows a loss of coherent QP excitations due to Mott localization. We discovered that the $\sqrt{2} \times \sqrt{2}$ structure reconstruction plays a crucial role in establishing the half-filling condition of the anti-bonding γ band. We provided microscopic theoretical support for this novel OSMT and demonstrated the importance of the crystal field splitting induced interorbital charge transfer and the orbital degeneracy for promoting an intriguing electronic phase with coexisting local moment and itinerant electrons. Our findings highlight the emergent and fundamentally important phenomena governed by the Mott physics in multi-orbital correlated electron systems, and call for more systematic studies of transition metal based materials.

Bibliography

[1] M. Neupane *et al.,* Phys. Rev. Lett. **103**, 097001 (2009).

[2] Y. Maeno *et al.,* Nature (London) **372**, 532 (1994).

[3] S. Nakatsuji and Y. Maeno, Phys. Rev. Lett. **84**, 2666 (2000).

[4] S. Nakatsuji *et al.,* Phys. Rev. Lett. **90**, 137202 (2003).

[5] R. Jin *et al.,* arXiv:0112405.

[6] V. I. Anisimov *et al.,* Eur. Phys. J. B **25**, 191 (2002).

[7] A. Koga *et al.,* Phys. Rev. Lett. **92**, 216402 (2004).

[8] N. Sato *et al.,* Nature (London) **410**, 340 (2001).

[9] A. Liebsch, Phys. Rev. Lett. **91**, 226401 (2003).

[10] A. Liebsch, Phys. Rev. Lett. **98**, 216403 (2007).

[11] Z. Fang, N. Nagaosa and K. Terakura, Phys. Rev. B **69**, 045116 (2004).

[12] S.-C. Wang *et al.*, Phys. Rev. Lett. **93**, 177007 (2004).

[13] N. J. C. Ingle *et al.*, Phys. Rev. B **72**, 205114 (2005).

[14] R. Matzdorf *et al.,* Science **289**, 746 (2000).

[15] D. S. Dessau *et al.,* Phys. Rev. Lett. **81**, 192 (1998).

[16] B. J. Kim *et al.,* Phys. Rev. Lett. **97**, 106401 (2006).

[17] T. Oguchi *et al.,* Phys. Rev. B **51**, 1385 (1995).

[18] S. Florens *et al.,* Phys. Rev. B **66**, 205102 (2002).

[19] J. P. Lu, Phys. Rev. B **49**, 5687 (1994).

[20] X. Dai, G. Kotliar and Z. Fang, arXiv:0611075.

[21] S. Wang and H. Ding, New. J. of Phys. **7**, 112 (2005).

Chapter 5

ARPES studies of iron-based superconductors

5.1 Motivation

Even though the details of the pairing mechanism in the recently discovered iron-based superconductors is still under intense debate, several theoretical investigations [2–6] and experimental observations [7–11] strongly suggest the importance of inelastic inter-band scattering between hole and electron Fermi surface (FS) pockets connected *via* the antiferromagnetic (AF) wave vector. Within this framework, the pairing strength depends on near- or quasi-nesting, here defined as a large enhancement of the spin susceptibility at a well defined wave vector [6]. The near-nesting conditions depend on the shape and size of the various FS pockets, which are tuned by the

position of the chemical potential. The evolution of the chemical potential with carrier concentration is thus a key issue to understand the evolution of FS near-nesting and superconductivity in these materials [1].

The 122-structural phase of $BaFe_2As_2$ is particularly suitable for a systematic study of the chemical potential shift since it can be doped either by electrons or holes following $Fe^{2+} \rightarrow Co^{3+}$ or $Ba^{2+} \rightarrow K^{+}$ partial substitutions, respectively. Interestingly, the electron- and hole-doped sides of the phase diagram show some noticeable differences. For example, while the maximum T_c value for the hole-doped side reaches 37 K at ambient pressure, it tops around 25 K for the electron-doped systems. Similarly, the superconducting dome extends to much higher doping in the hole-doped case, with an optimal concentration of around 0.2 hole/Fe against 0.08 electron/Fe for the electron-doped side.

Angle-resolved photoemission spectroscopy (ARPES) is a powerful tool to access directly the electronic structure with respect to the chemical potential. Our previous ARPES studies have already revealed strong variations in the pairing strengths associated with the various FS sheets in the electron-doped compounds [10] as compared to the hole-doped ones [7,12], as well as the deterioration of the near-nesting conditions in highly overdoped samples for which T_c vanishes or is significantly suppressed [9,13]. Although near-nesting was naturally proposed to explain these anomalies, this concept has not been linked to the origin of the electron-hole asymmetry (EHA) and up to date there is still no systematic investigation of the impact of the chemical

potential shift on the band structure throughout the whole phase diagram.

Here we present a systematic ARPES study of the chemical potential as a function of carrier doping in the 122-pnictides. With doping, the chemical potential moves smoothly with respect to the low-energy valence states, in agreement with our local density approximation (LDA) calculations. However, we observed anomalously larger (smaller) core level shift than the valence band shift on the hole (electron)-doped side for the relatively undisturbed As $3d$ core levels, possibly due to the screening effect which increases (decreases) the core level shifts upon hole (electron) doping. Based on a rigid band shift approximation justified by our experimental results, we computed the doping dependence of the Lindhard spin susceptibility at the AF wave vector, and found that the Lindhard function itself is asymmetric as a function of doping, in a similar fashion as the asymmetry between the hole and electron superconducting domes. This strongly supports FS-near-nesting-enhanced superconductivity in the pnictides.

5.2 Nesting scenario

Nesting can be explained in a simple way in iron-based superconductors. Some experimental results and theoretical calculations show that an iron-based superconductor actually has several ringlike Fermi surfaces. Crucially, one specific ring can be shifted as a whole to overlap another by a translation vector, an arrangement called "nesting" as shown in Fig. 5.1. In fact, the ring must be shifted by a wavelength and in a

direction that exactly matches the spacing and orientation of the antiferromagnetic striping in the parent compound [14].

The nesting scenario is important in iron based superconductors. It is important to know how nesting conditions change with doping. In the following, a few examples are given in the case of hole and electron doping of Ba122 systems.

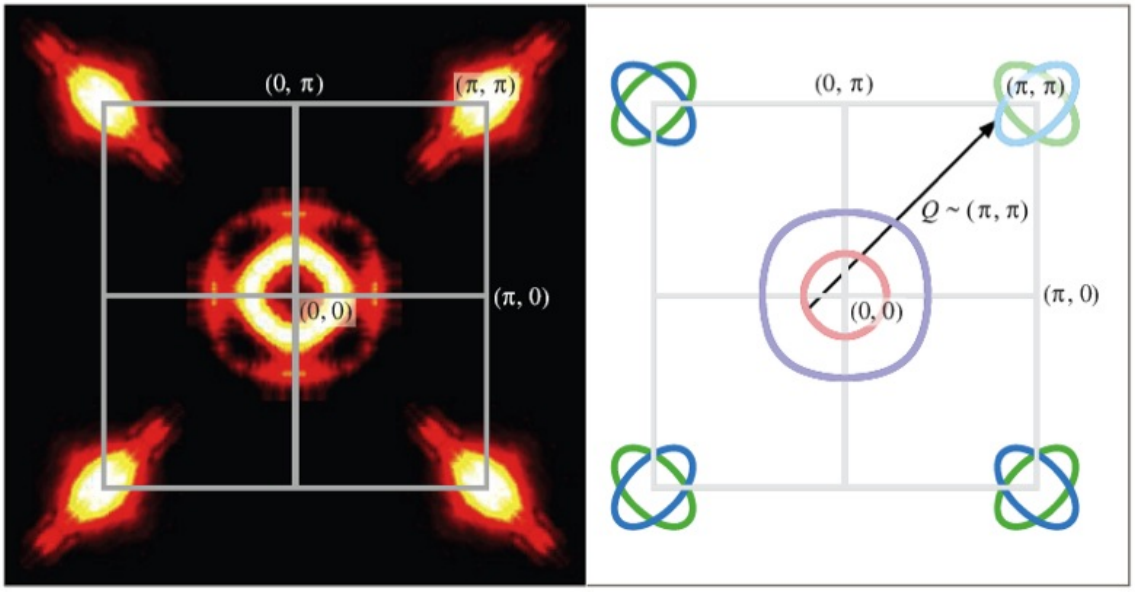

Figure 5.1: **Lay it on me:** The Fermi surfaces of $Ba_{0.6}K_{0.40}Fe_2As_2$ (left) map the momenta of its electrons. Superconductivity may arise because one surface can be shifted to cover another [14].

Optimal doping: hole- and electron-doped For the optimal hole doping system ($Ba_{0.60}K_{0.40}Fe_2As_2$), the ARPES results show two hole like Fermi surfaces (FS) at the zone centre (Γ) and two electron like FS at the zone corner (M point) of the Brilliouin

Zone (BZ), as shown in Fig. 5.2(a). The SC gap values for hole and electron like FSs are plotted in Fig. 5.2 (b) and (c) respectively, which clearly indicate a nearly isotropic values. Also, the gap size and the pairing strength are estimated for the α ($\Delta_\alpha \sim$ 12 meV ; $2\Delta_\alpha/\mathrm{k}_B\mathrm{T}_c = 7.7$), β ($\Delta_\beta \sim 6$ meV ; $2\Delta_\beta/\mathrm{k}_B\mathrm{T}_c = 3.6$), γ ($\Delta_\gamma \sim 12$ meV; $2\Delta_\gamma/\mathrm{k}_B\mathrm{T}_c = 7.7$) and δ bands ($\Delta_\delta \sim 11$ meV; $2\Delta_\delta/\mathrm{k}_B\mathrm{T}_c = 7.2$). The weak coupling BCS pairing strength is around 3.52 (5.6 meV; $2\Delta/\mathrm{k}_B\mathrm{T}_c = 3.52$). Compared with the BCS value, there is a strong pairing amplitude in the inner hole band and electron bands. The size of the inner hole-like Femi surface (α) is approximately the same as that of the electron-like FSs (γ, δ). There is a nesting between inner hole like Fermi surface and electron like Fermi surfaces. There is a strong pairing in the nested Fermi surfaces which is approximately twice as large as the BCS limit [7, 12].

For an optimally electron-doped system ($BaCo_{0.15}Fe_{1.85}As_2$), Figures 5.2(d) and (e) show the FS plot and the SC gap. Due to electron doping, the chemical potential moves up so that one of the hole band lies below E_F. Thus, only one small hole like FS and two bigger electron like FSs are observed. The size of the observed β FS is somehow similar with observed electron FSs. These FSs are nested with each other through the $Q = (\pi, \pi)$ wavevector. It is important to note that the pairing strength of the β ($2\Delta/\mathrm{k}_B\mathrm{T}_c \approx 6$) is enhanced. The FS nesting condition switches from the α to the β band FS as we go from optimally hole- to electron-doped systems [10]. These results are summarized in Fig. 5.3.

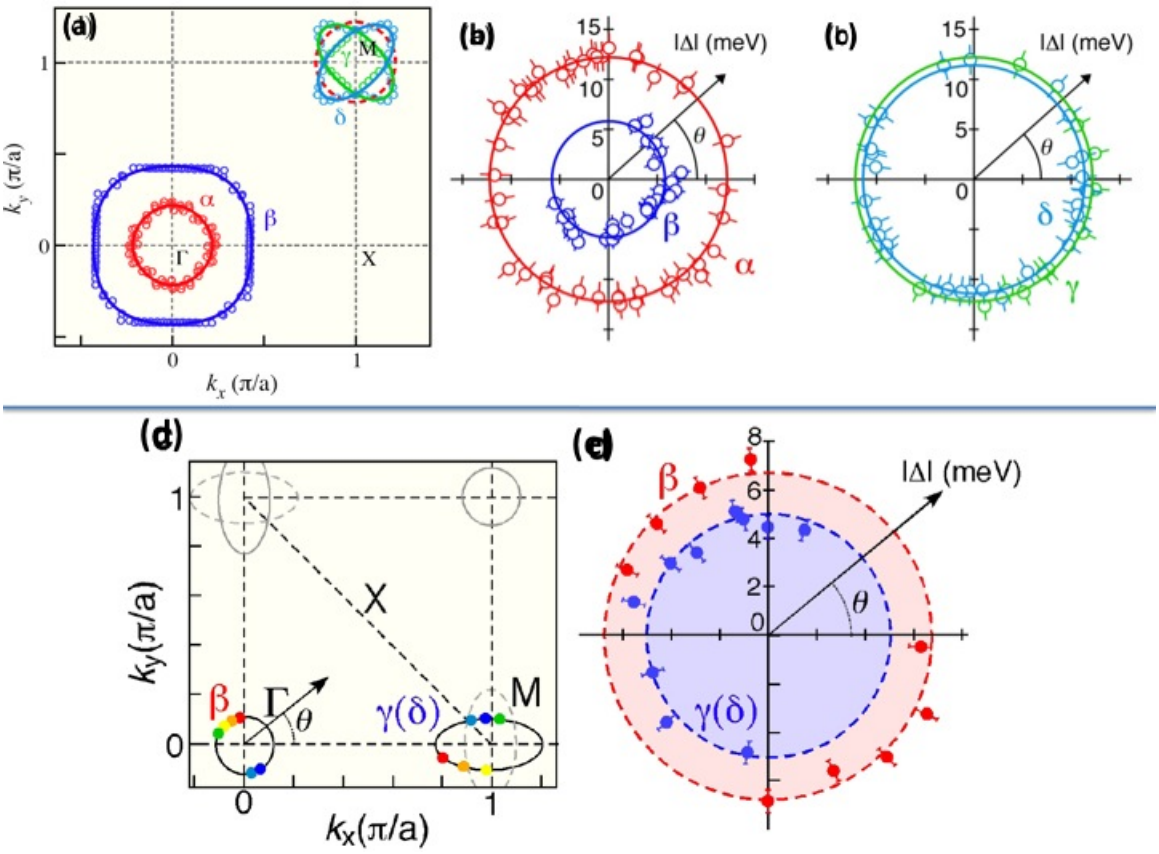

Figure 5.2: (a) Measured Fermi surface (FS) (circle) and tight-binding fitting curves (solid lines). The dashed line is the α FS shifted by the (π, π) wavevector. (b), (c) Superconducting (SC) gap size at 15 K for the (b) α, β and (d) γ and δ FSs as a function of polar angle (θ) [12, 20] for $Ba_{0.60}K_{0.40}Fe_2As_2$ (d) Extracted FS from the ARPES measurements for $BaCo_{0.15}Fe_{1.85}As_2$ (e) SC gap values at 8 K as a function of polar angle (θ) for the β and γ, δ (red and blue dots, respectively) [10].

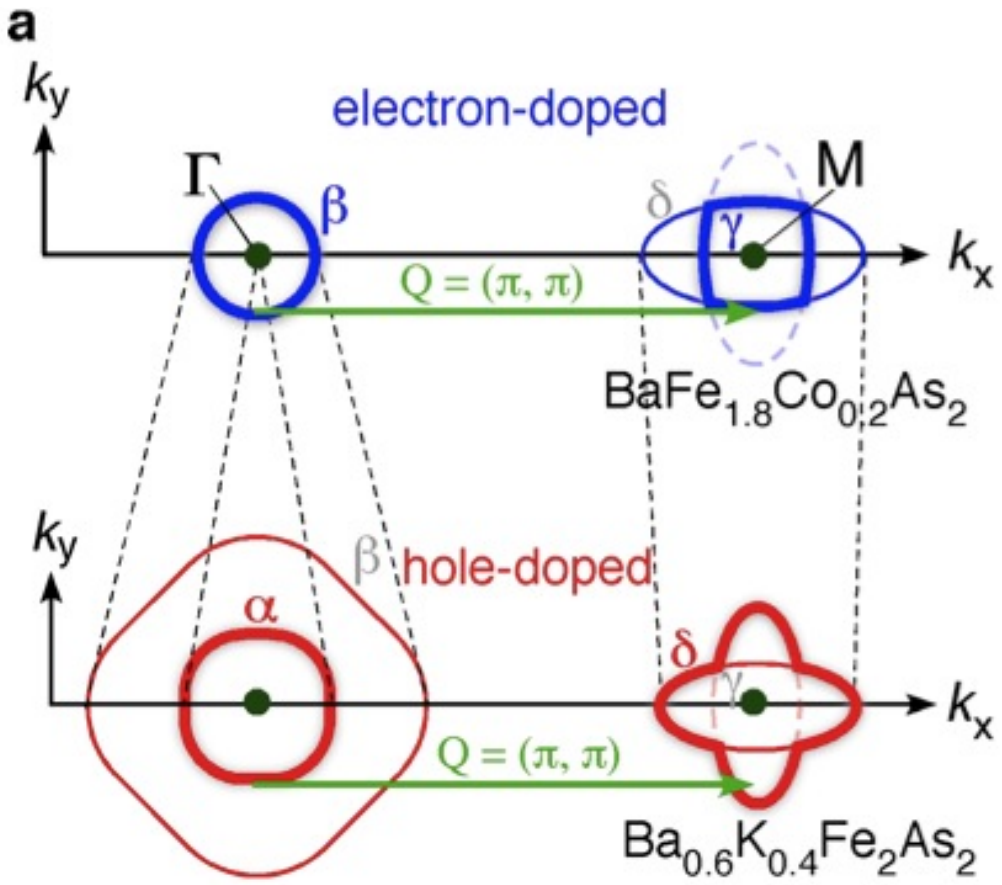

Figure 5.3: (a) Comparison of the energy bands between the optimally hole (K) and electron (Co) doped samples. In the optimally hole doped case, the nesting occurs in between the inner hole and outer electron Fermi surfaces while it is between the outer hole and electron FS in optimally Co-doped samples.

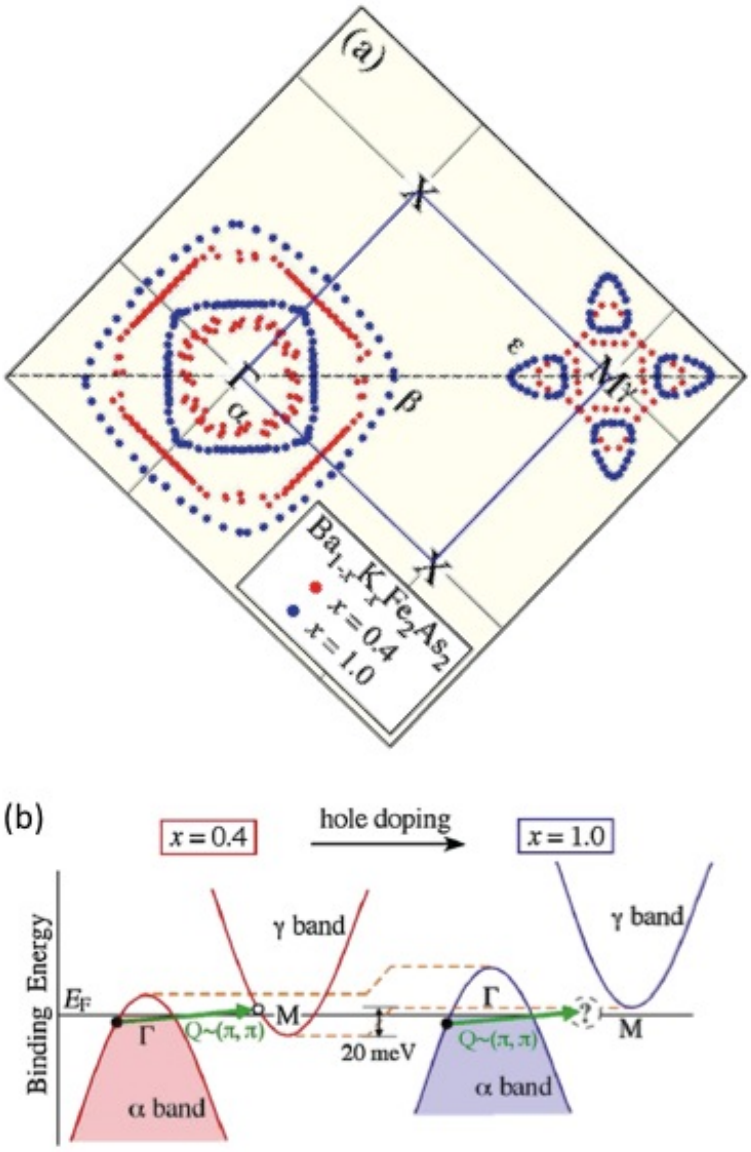

Figure 5.4: (a) Comparison of experimentally determined k_F points between over-doped KFe_2As_2 (T_c = 3 K) and optimally doped $Ba_{0.6}K_{0.4}Fe_2As_2$ (T_c = 37 K) (blue and red circle respectively.) (b) Schematic view of the interband scattering by the AF wave vector Q_{AF} between the hole and electron bands (the α and γ bands) centered at the Γ and M points, respectively [13].

Overdoping: hole- and electron-doped Figure 5.4(a) shows the FS plots for KFe_2As_2 compared with $Ba_{0.6}K_{0.4}Fe_2As_2$. Excess of hole doping means that the chemical potential moved down as compared with optimal hole doping. The electron bands are above the Fermi level and we do not see any electron-like FSs at the M point. The two big hole-like FSs are observed at the zone center. Thus, there is a significant modification of Fermi surface topology, especially at the M point as compared with optimal doping. In the case of KFe_2As_2 ($T_c \sim 3$ K), the near nesting conditions are destroyed. No nesting means no or low T_c [13].

For an over-doped electron system ($BaCo_{0.30}Fe_{1.70}As_2$), figure 5.5(a) presents a comparison of the FS plot with optimally electron-doped system ($BaCo_{0.15}Fe_{1.85}As_2$). Over doping electrons means that the chemical potential moves up as compared with optimal doping electrons. This means that the hole bands are below the Fermi level (E_F). Therefore, no hole-like Fermi surfaces are observed in case of ($Co_{0.30}$). But two big electrons like FSs are observed. Thus there is also a significant modification of the Fermi surface topology which destroys the nesting condition. As shown in the schematic diagram in Fig. 5.5(b), the β FS and γ FS of the SC $Co_{0.15}$ sample are well inter-connected by the AF wave vector $Q_{AF} = (\pi, \pi)$. There is no α band at E_F, and the size of the β FS and γ FS are somehow similar, allowing nesting or quasi-nesting between the relatively similar size FSs. In the case of $Co_{0.30}$, no nesting or quasi nesting condition is applicable because of the significant modification of FSs at the Γ point [9].

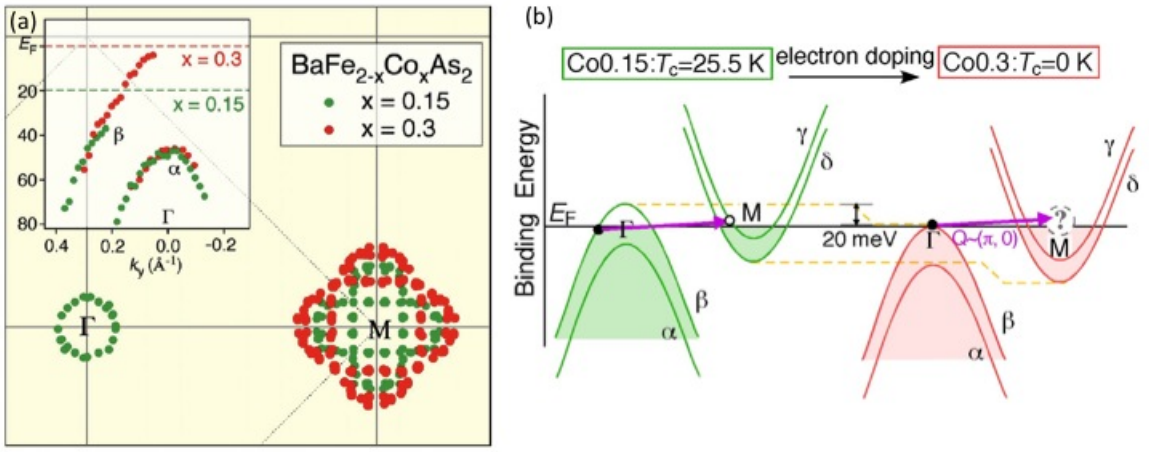

Figure 5.5: (a) Comparison of experimentally determined k_F points between SC $Co_{0.15}$ and non-SC $Co_{0.30}$ samples. The inset shows the experimental band dispersion in the vicinity of E_F around the Γ point. (b) Comparison of energy bands between the $Co_{0.15}$ and $Co_{0.30}$ samples. The interband scattering is dramatically suppressed in the non-SC $Co_{0.30}$ sample since the holelike α and β bands at Γ point are basically below the Fermi level [9].

From the above discussion, the following points can be drawn as conclusions:

1. In multiband Fe-based superconductors, the superconducting gap varies from one Fermi surface pocket to another.

2. The SC gap on each Fermi surface is isotropic.

3. There is sufficient evidence suggesting the importance of inter-band scttering.

4. Superconductivity in these materials is most likely related to AF fluctuations.

5.3 Chemical potential shift with doping and electron-hole asymmetry

Experimental method The high-quality single crystals of the 122 series used in this study were grown by the flux method [15]. Low-energy electron diffraction on mirror-like cleaved surfaces show a sharp 1 x 1 pattern in the non-magnetic phase. High-resolution (4-20 meV) ARPES measurements of the low-energy electronic structure were performed in the photoemission laboratory of Tohoku University using a microwave-driven Helium source (hv = 21.218 eV) and core level studies were done at the Synchrotron Radiation Center and the Advanced Light Source in USA, as well as at the Photon Factory in Japan, using various photon energies. Our experiments have been performed using high-efficiency VG-Scienta SES-100, SES-2002 and R4000 electron analyzers. Samples were cleaved *in situ* and measured at 7-40 K in a vac-

uum better than 1 x 10^{-10} torr. The samples have been found to be very stable and without degradation for the typical measurement period of 20 hours.

Core level and chemical potential shift with doping Photoemission allows measurement of the core level states relative to the chemical potential. It has been used widely in the past to study the chemical potential shift in high-T_c cuprates [16–18]. Fig. 5.6(a) shows a comparison of the core levels in the 0-110 eV binding energy range of 7 samples distributed in the electron-doped and hole-doped sides of the phase diagram. These samples are $BaFe_{1.70}Co_{0.30}As_2$ (T_c = 0 K), $BaFe_{1.84}Co_{0.16}As_2$ (T_c = 20 K), $BaFe_{1.92}Co_{0.08}As_2$ (T_c = 0 K), $Ba_2Fe_2As_2$ (T_c = 0 K), $Ba_{0.75}K_{0.25}Fe_2As_2$ (T_c = 26 K), $Ba_{0.60}K_{0.40}Fe_2As_2$ (T_c = 37 K), and $Ba_{0.30}K_{0.70}Fe_2As_2$ (T_c = 22 K). For simplicity, here after we call them $Co_{0.30}$, $Co_{0.16}$, $Co_{0.08}$, Ba122, $K_{0.25}$, $K_{0.40}$ and $K_{0.70}$, respectively. From low to high binding energies, we observed the Fe 3d (around the Fermi level), Ba 5p (∼14.5 eV), K 3p (∼18 eV), As 3d (∼ 40.4 and 41.3 eV) and Ba 4d (∼ 89.5 and 92 eV) states, respectively. In particular, the As 3d peaks are very strong in all compounds regardless of Co and K doping. Based on a previous photoemission study [19] that indicates that the As atoms in $BaFe_2As_2$ are not perturbed significantly at the cleaved surface, we used the As 3d core levels to investigate the doping dependence of the chemical potential. In Fig. 5.6(b), we show a zoom of the As 3d core levels of all compounds. The position of the peaks moves towards the lower binding energies as K concentration increases. In contrast, the peak positions are almost unaffected by Co-doping. We plot in Fig. 5.6(c) the shift of the As $3d_{3/2}$

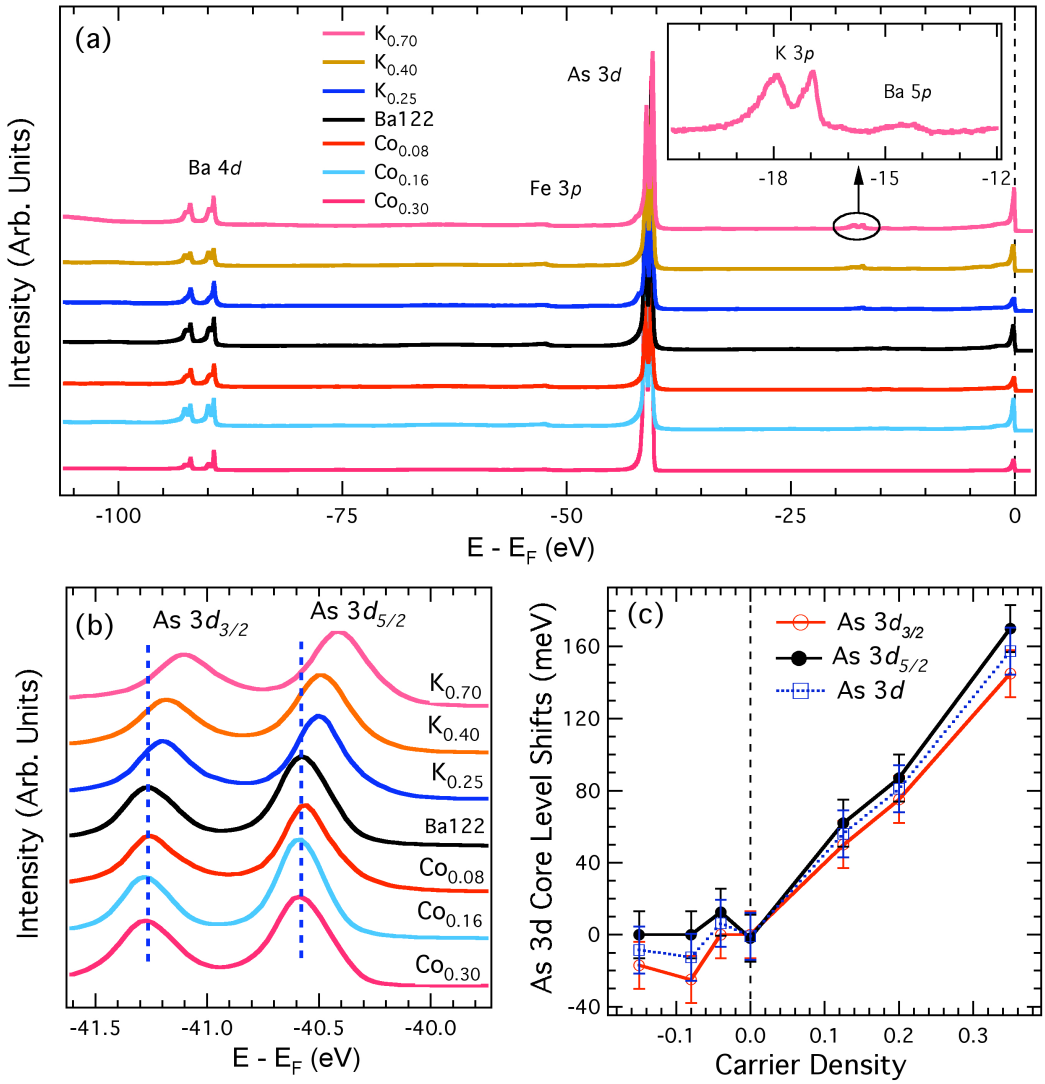

Figure 5.6: (a) Core levels of the Ba122 series recorded with a photon energy of 140 eV. The inset shows a zoom of the core levels of the $K_{0.70}$ sample in the 12-21 eV binding energy range. (b) Zoom of the As $3d$ core levels. (c) Doping dependence of the As $3d_{3/2}$ and As $3d_{5/2}$ core level energies as a function of carrier density (half of the x value). The average is represented by the blue dotted line.

and As $3d_{5/2}$ levels as a function of carrier density, which is half of the value x for both K and Co dopings. The blue dashed line in Fig. 5.6(c) gives the average of the As $3d$ peaks as a function of doping.

An alternative and more direct determination of the chemical potential shift is obtained by looking at the band dispersion near the Fermi level (E_F). In Figs. 5.7(a) and (b), we present ARPES intensity plots of the $Co_{0.16}$ and $K_{0.40}$ samples along a cut passing through M as indicated in Fig. 5.7(e). The corresponding second derivative intensity plots are displayed in Figs. 5.7(c)-(d). The blue dashed lines are guides to the eye indicating the bottom of the upper electron band (the γ band as defined in Ref. [20]). The bottom of this electron band at the M point moves down from E_F as the signed concentration decreases (more electrons), which is what we expect from simple band filling. In particular, this behavior supports the assumption that the Fe $\rightarrow$ Co substitution electron-dope the Fe layer, in contrast to a recent density functional theory calculation suggesting that Co and Ni only act as scattering centers in the Fe planes [21]. It is also consistent with the observation of a downshift of the Γ-centered holelike bands in the Co-doped side [9]. Fig. 5.7(f) summarizes our results of the seven differently doped samples and gives the position of the bottom of the electron band as a function of the carrier density.

At this point, it is instructive to compare LDA calculations to the core level shifts and the shift of the bottom of the electron band, which corresponds to the chemical potential shift in a rigid band picture. The results are summarized in Fig. 5.8. It is

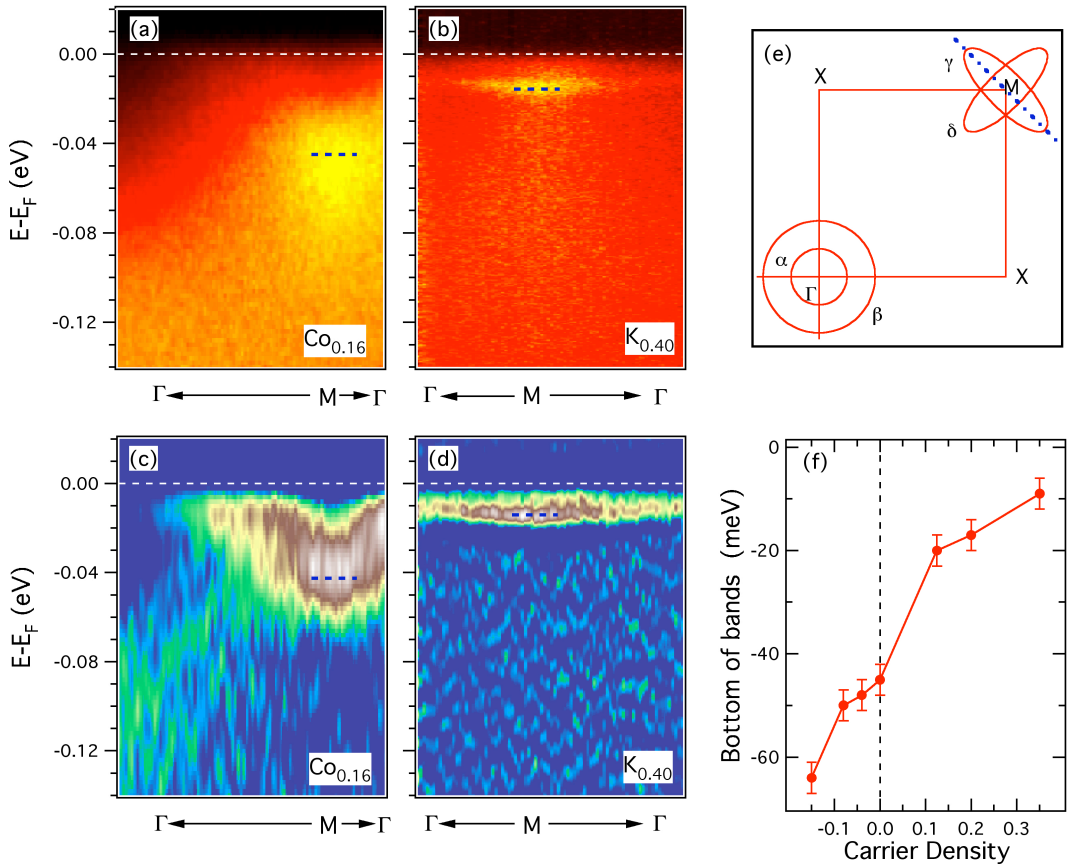

Figure 5.7: (a) and (b) ARPES intensity plots of the $Co_{0.16}$ and $K_{0.40}$ samples, respectively, along the cut passing through M indicated by a dashed line in panel (e). (c) and (d) Corresponding second derivative intensity plots. (f) Bottom of the electron bands versus carrier density.

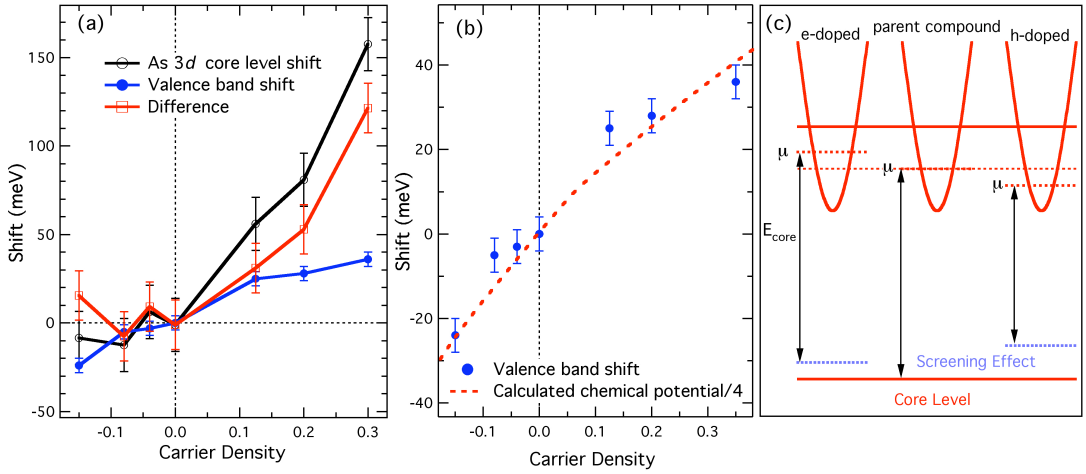

Figure 5.8: Valence band and core level shifts as a function of the carrier density. (a) The black line with open circles shows the core level shifts while the blue line with closed circles gives the valence band shifts measured from the band bottom. The red line with open squares gives the difference between the core level and chemical potential shifts. (b) The blue dots are the valence band shifts shown in panel a, and the red dash line is the LDA calculated values of the chemical potential divided by a factor of 4. (c) Pictorial representation of the explanation of the core level and the chemical potential shifts as a function of carrier density.

clear from Fig. 5.8(a) that the core level shift is not the same as the shift of the valence band, and the difference between them are larger on the hole-doped side, which will be discussed below. Interestingly, the theoretically calculated chemical potential shift is very much consistent with the observed valence band shift when theoretical values are divided by 4 as shown in Fig. 5.8(b), which is understood in terms of the band renormalization reported in previous ARPES studies [9, 10, 13, 20]. This indicates that the shift of the valence band corresponds to the chemical potential shift, and consequently, the rigid band picture derived from the renormalized band structure is valid.

The core level shift can be understood as follows. The core level shift ΔE is related to the chemical potential shift $\Delta\mu$ by the relation:

$$\Delta E = -\Delta\mu + K\Delta Q + \Delta V_M + \Delta E_R \tag{5.1}$$

where ΔQ is the change in valency, K is a constant, ΔV_M is a shift due to change in the Madelung potential, and ΔE_R is the change in the core-carrier screening [22]. Doping is not expected to change the As valency. This implies that the term $K\Delta Q$ can be neglected. Therefore, the difference between the core level and the chemical potential shift represented in Fig. 5.8(a) by the red line is only related to ΔV_M and ΔE_R. It is known that the screening term ΔE_R is proportional to the mobile carrier concentration, thus one expects that it has the same sign on the electron- and hole-doped sides and increases with doping. Such doping dependence of the screening term, as indicated in Fig. 5.8(c), will increase (reduce) the core level shift caused by

the chemical potential shift on the hole (electron)-doped side. This is consistent with our observation of different behaviors of the core level shift on hole- and electron-doped sides. We note that the change of the Madelung term ΔV_M may not be same on hole- and electron-doped sides, which can further enhance the difference of the core level shift on the two sides.

Electron-hole asymmetry The above analysis suggests that a rigid band picture constitutes a good first approximation of the evolution of the chemical potential in the 122 family of iron-pnictides. We now ask a simple but fundamental question: is FS near-nesting able to explain the electron-hole asymmetry of the superconducting domes shown in the phase diagram of the 122-pnictides of Fig. 5.9(a)? To answer this question, it is necessary to compute the spin susceptibility. It is especially important to understand how the susceptibility evolves at the near-nesting (or AF) wave vector. We use the band structure calculated by LDA to compute the doping dependence of the Lindhard spin susceptibility at the near-nesting wave vector [25, 26]. We limit our calculations to the elastic component of the spin susceptibility. The results are displayed in Fig. 5.9(b). Interestingly, the hole- and electron-doped sides exhibit a strong asymmetry: while the Lindhard function decreases monotonically on the electron-doped side (with a small shoulder around $\sim$0.12), it keeps a high value for a wide hole doping range before starting to decrease. Remarkably, the maximum value of the calculated susceptibility is obtained near the experimental optimal hole doping, and the Lindhard function using the FS nesting wave vector tracks the

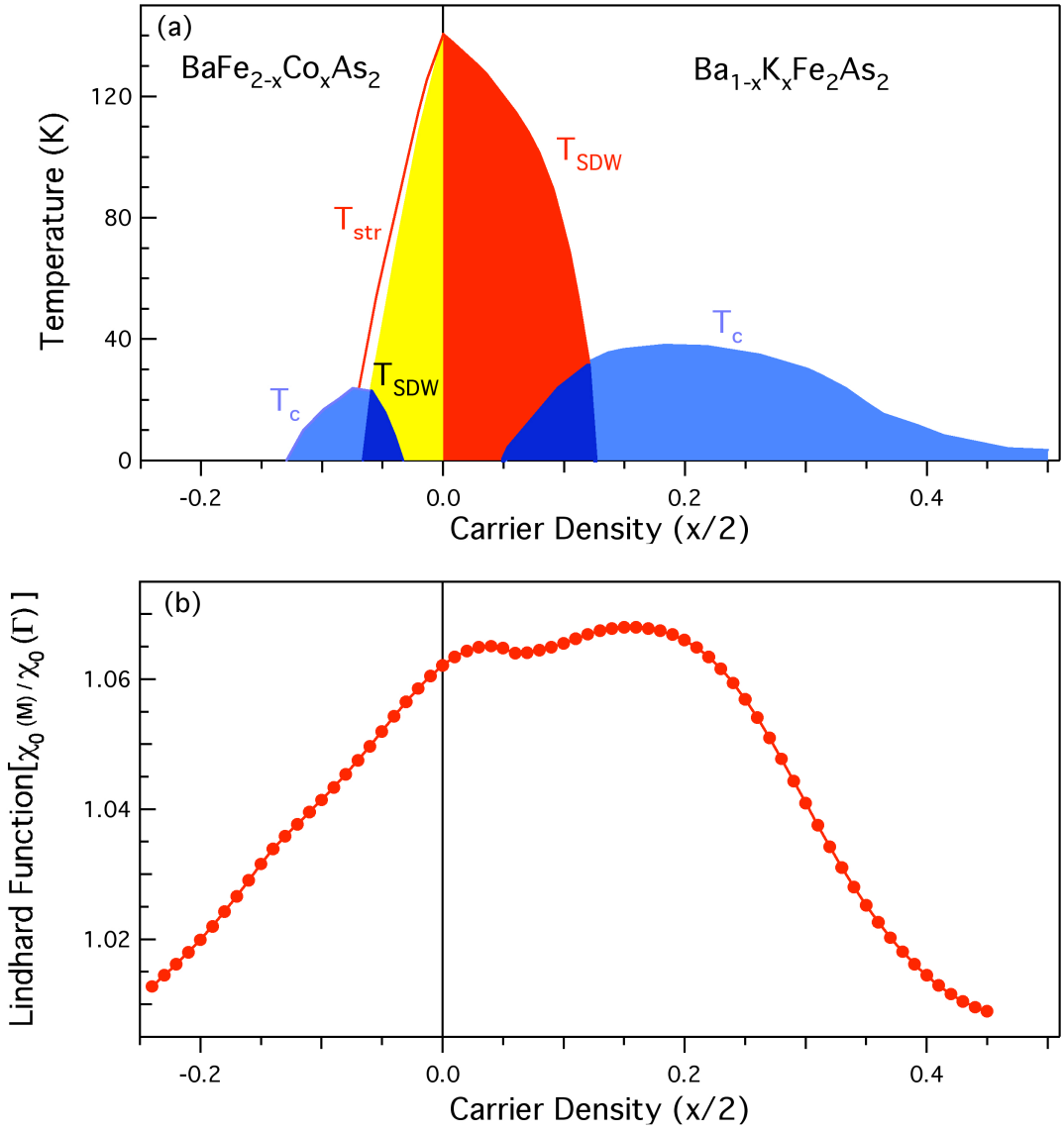

Figure 5.9: (a) Phase diagram of the hole- and electron-doped Ba-122 systems taken from references [23] and [24], respectively. T_c, T_{SDW} and T_{str} refer to the superconducting, the SDW and the tetragonal to orthorombic structural transitions, respectively. (b) Doping dependence of the Lindhard function at the M point (near-nesting wave vector) normalized by its value at the zone center. The Lindhard function was obtained by using LDA calculation.

superconducting transition qualitatively well. It is important to note that such an asymmetry in the Lindhard susceptibility would lead to a higher dielectric function and consequently to a larger screening effect on the hole-doped side. This is qualitatively consistent with the observed larger difference between the core level shift and the chemical potential shift on the hole-doped side shown in Fig. 5.8(a). We caution that the non-magnetic LDA calculations are no longer valid in the spin density wave (SDW) state because the band structure undergoes unconventional band folding that leads to the formation of Dirac cones [27].

The basic reason for electron-hole asymmetry in the calculated Lindhard function is as follows. The effective masses of the holelike bands, especially the β band, are larger than that of the electronlike bands at the M point, as observed by ARPES [20] and quantum oscillation experiments [28]. To satisfy the Luttinger theorem, their top of band at zero doping must thus be closer to E_F than the bottom of the electron bands. Indeed, even for optimally hole-doped samples, the top of the α band is located only 25 meV above E_F [11]. As a consequence, the holelike bands sink below E_F with electron doping much faster than the bottom of the electron bands are pushed above E_F with hole doping. Therefore, the FS near-nesting conditions are more robust in the hole-doped case. The built-in asymmetry regarding the FS near-nesting condition on the electron- and hole-doped sides offer a simple but powerful clue that the FS near-nesting with the AF wave vector triggers superconductivity in the pnictides.

Conclusion In conclusion, we have presented the doping dependence of the chemical potential in the 122 family of iron-pnictides. As a first approximation, our results are consistent with a rigid band shift and with renormalized LDA calculations. The doping dependence of the As $3d$ core levels does not follow that of the chemical potential, suggesting a non-negligible screening effect. Within the rigid band shift approximation, the calculated Lindhard function at the FS-nesting wave vector based on the LDA band structure reveals an electron-hole asymmetry in the iron pnictides, which matches well with the observed electron-hole asymmetry of the superconducting domes in the phase diagram. Our findings reveal the importance of FS near-nesting in the pairing mechanism of the iron-based superconductors.

5.4 Other projects on 122 and 11 systems

Fermi surface and k_z dispersion in 122 system

Fermi surface of 122 system: Fermi surface measurement of Co = 0.16, 0.08, Ba122 and K = 0.10 for the Ba122 systems have been performed, as is shown in Fig. 5.10. In all cases, hole like Fermi surfaces at the zone center and electron-like Fermi surfaces at the zone corners have been observed. Similarly, a cut at Γ and along the Γ-M direction for all four dopings and their energy second derivatives plots are shown in Fig. 5.11. Holelike and electronlike bands are clearly observed.

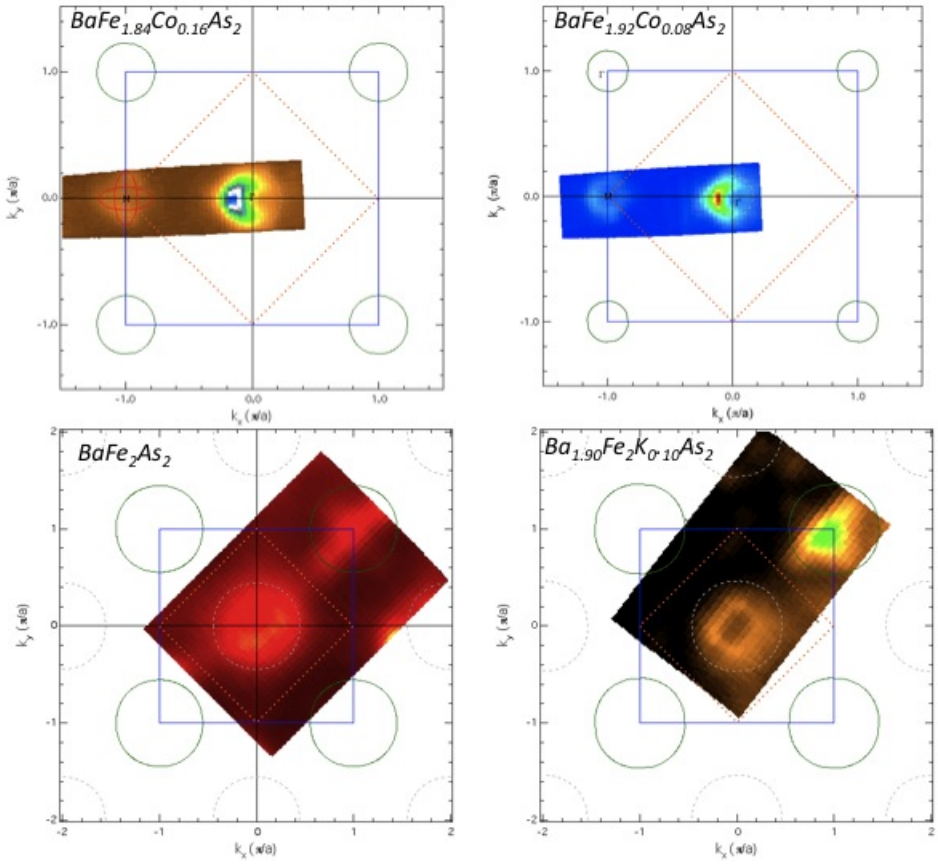

Figure 5.10: Fermi surface measurement of Co = 0.16, 0.08, Ba122 and K = 0.10 for the Ba122 systems. In all cases, hole and electron FSs are clearly seen.

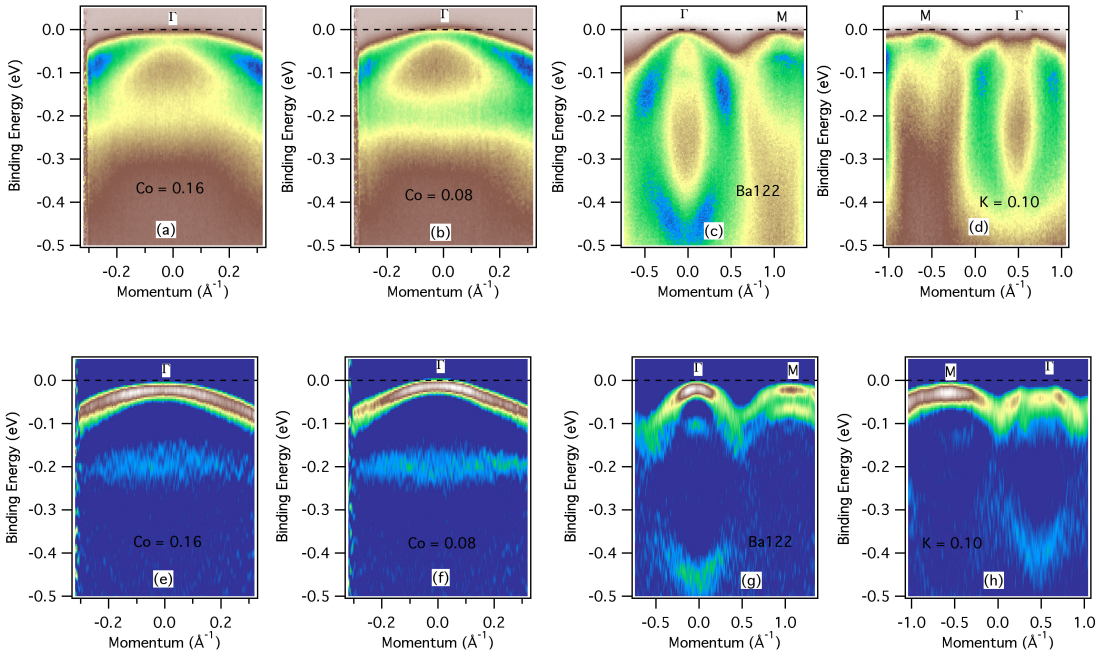

Figure 5.11: A cut and its 2^{nd} derivative at the Γ point along Γ-M for Co = 0.16, 0.08, 0 and K = 0.10 for the Ba 122 systems.

k_z dispersion: Some theoretical and ARPES studies suggest that unlike the copper oxide superconductors, the iron-based superconductors have a 3D Fermi surface. Actually, despite the fact that ARPES is a 2D measurement due to non-conservation of the perpendicular component of momentum at the surface, one can still access the 3D electronic structure by varying the probing photon energy ($h\nu$). Thus tuning the incident photon energy, the allowed direct transition will shift in energy and consequently in the momentum k_z perpendicular to the a-b plane, which helps to determine the electronic dispersion along the c-axis. In the free electron final state approximation, the conversion is given by

$$k_z = \frac{1}{\hbar}\sqrt{2m[(h\nu - \phi - E_B)cos^2\theta + V_0]} \tag{5.2}$$

where V_0 is an experimentally determined inner potential [22].

Fig. 5.12 shows the k_z dispersion for 4 different kinds of samples. For Co doped and parent compound samples, the k_z dispersion is strong for hole like bands. But there is a weaker k_z dispersion for the K = 0.10 sample. Also, it is interesting to note that the k_z dispersion is weaker at the M point in Ba122 and $Ba_{1.90}K_{0.10}Fe_2As_2$ samples.

The Co-doped side shows stronger k_z dispersion as compared to the K-doped side in the under-doping cases. The reasons may be the followings:

1. If you are in the hole-doped side, V_F becomes larger, so one would not expect big change in V_F. This means that the Fermi surface will vary slower along the z direction. This behavior is opposite in the Co-doped side.

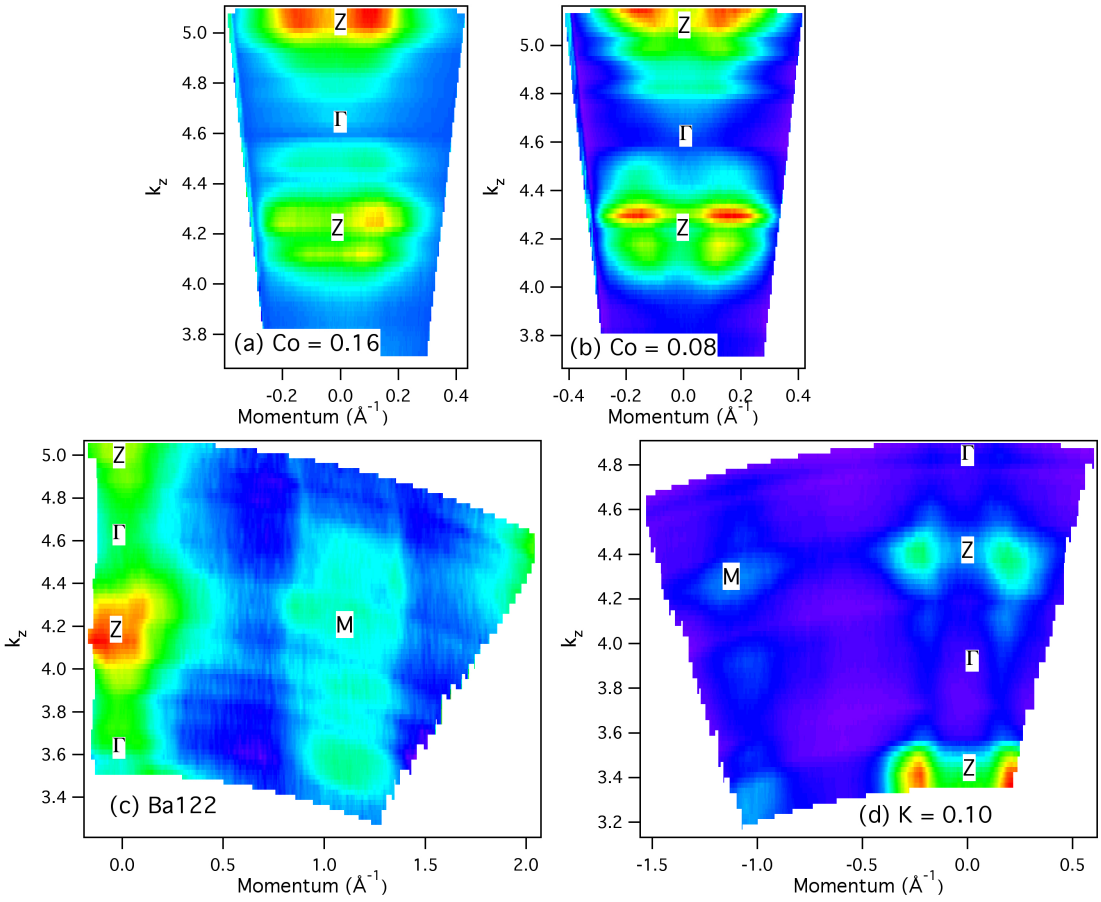

Figure 5.12: k_z dispersion for Co = 0.16, 0.08, Ba122 and K = 0.10 for the Ba 122 systems. The parent compound and the electron- doped side show stronger k_z dispersion as compared to the hole doped side.

2. AF is stronger on the electron-doped side which means that k_z will vary more and for a wider range of doping. The k_z variation is much stronger in the AF phase.

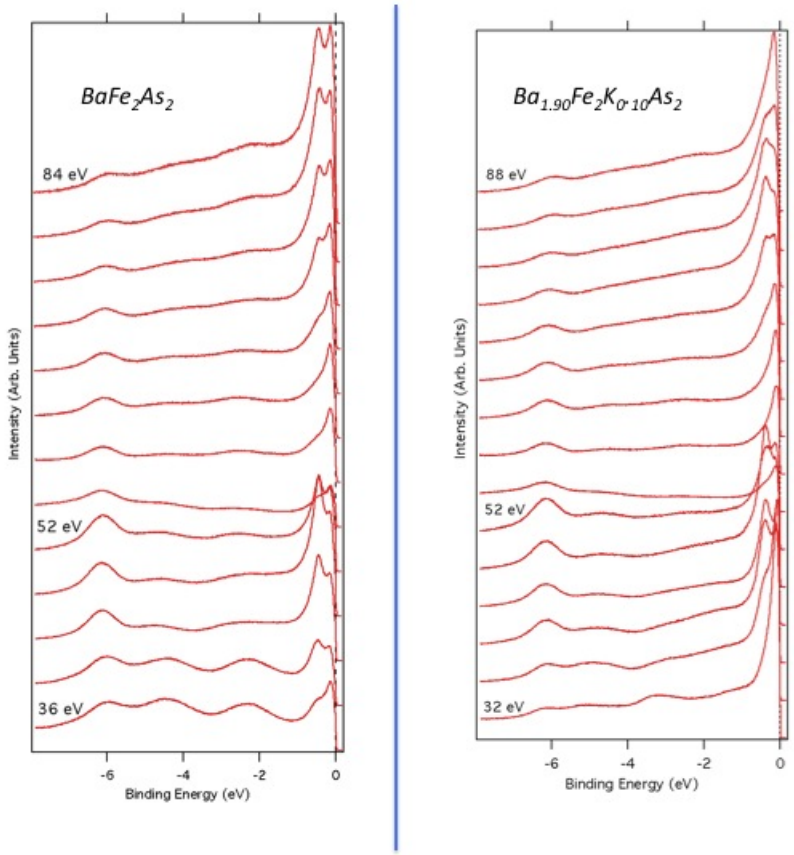

Figure 5.13: EDCs curves for different photon energies for the Ba122 systems: Ba122 and K = 0.10.

In Fig. 5.13, the valence band energy distribution curves (EDCs) for different photon energies are plotted. It is interesting to note that there are two peaks initially at low photon energy. But as we go to higher photon energy ($\sim$ 60 eV) these 2 peaks

are merged into a single one. As we increase photon energies further, the two peaks re-appear. This can be explained in term of k_z dispersion.

There is a strong k_z dispersion at the Z point. Thus, the single peak of EDC curves has been observed around the Z point. At this point, all hole bands (probably all 3 bands) cross E_F or are very near to E_F. Other than Z point or close to Z point, some hole-like bands are below E_F which indicates weaker k_z dispersion.

Core levels and FS study of the 11 system

The very recent observation of unusual superconductivity and magnetic order in structurally simpler compounds, such as $FeSe_x$ and $Fe_{1+y}Te_{1+x}Se_x$ is a high priority for current research in iron-based superconductors. Due to significantly simpler crystal structures, there is a high expectation for these compounds to give the key ingredients for superconductivity and the nature of the magnetically order state of their parent compounds. Superconductivity with T_c up to 15 K is achieved in the Fe_{1+x}(Se, Te) series and T_c increases up to 27 K under modest applied pressure. The T_c value of $FeSe_x$ is about 8 K. The electronic structure is very similar to the iron pnictides and magnetic order in FeTe originates from very strong Fermi surface nesting leading to the largest spin density wave gap in these series [29–33].

Core level study of $FeTe_{1-x}Se_x$: Core level studies have been done for x = 0.20, 0.30 and 0.40 of the $FeTe_{1-x}Se_x$ system. In all cases, the Se 3d level ($\sim$ 55.5 eV, 54.6 eV), Te 4d level ($\sim$ 41.9 eV, 40.4 eV), Fe 3p level ($\sim$ 52.7 eV) and Fe 3d level near E_F have been clearly seen. Fig. 5.14(a) shows the photon energy dependence

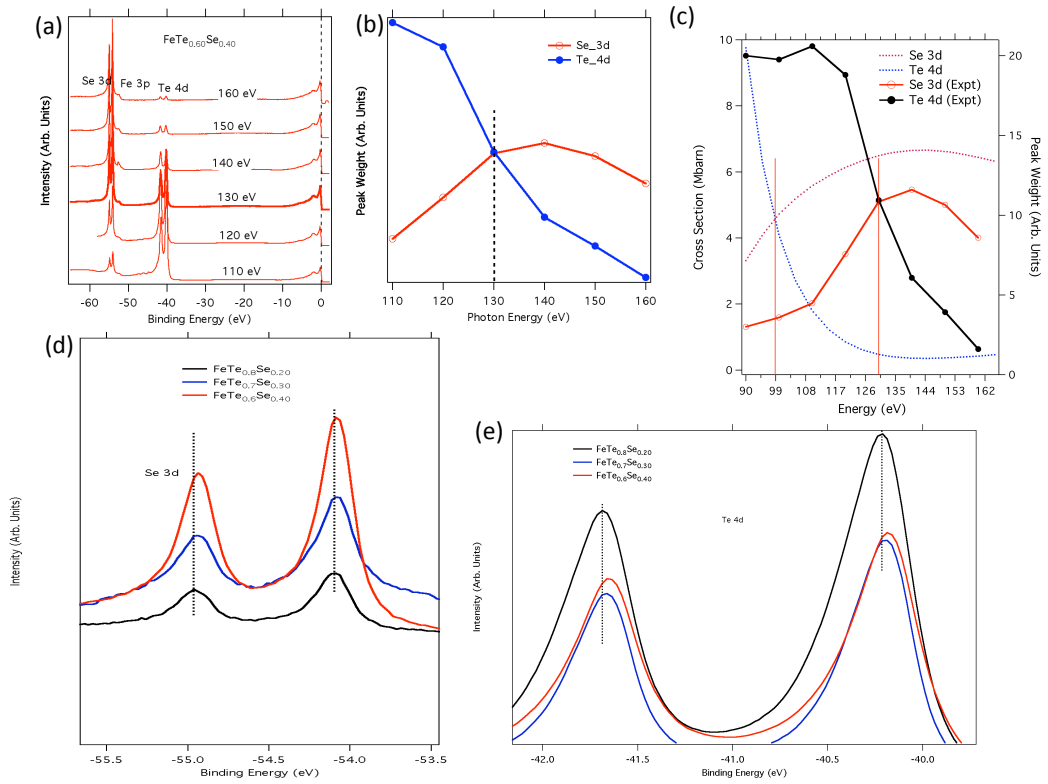

Figure 5.14: (a) Core level for $FeTe_{0.60}Se_{0.40}$ for different photon energies. (b) Experimentally determined peak weights for Se 3d and Te 4d as a function of photon energy. The crossing point is around 130 eV shown by black dash line. (c) Calculated cross-section for Se 3d and Te 4d, and experimentally determined peak weight as a function of photon energy. (d) Comparison of Se 3d core levels for $x = 0.40$, 0.30 and 0.20 (d) same as (c) for the Te 4d levels.

of the core levels for x = 0.40 system. It is clearly seen that the peak weight of Te 4d start to decrease when photon energy increases from 110 eV to 160 eV. However, the opposite effect has been observed for the Se 3d core levels. The peak weight for Se 3d and Te 4d versus photon energy are plotted in Fig. 5.14(b). Around 130 eV, the intersection of these curves has been observed. In Fig. 5.14(c), the calculated cross-section and the experimentally determined peak weight for Se 3d and Te 4d are plotted as a function of photon energy. The intersection points for theoretically calculated cross-section ($\sim$ 100 eV) and experimentally determined peak weight ($\sim$ 130 eV) are different. The different crossing points between the measurements and calculations can be due to several factors:

1. There are different percentages of Te and Se.

2. The chemical environments are different.

3. In principle, there should be both surface and bulk contributions to Se and Te core levels. However, there seems to be only one set of core levels. Either the surface and bulk are same, or we do not see the bulk.

The substitution of Te by Se gives no change of valency because they are isovalent. Thus the peak positions of Se 3d and Te 4d are not expected to change for different values of x. For $x = 0.20$, 0.30 and 0.40, there is no significant change of the peak position, as shown in Fig. 5.14(d) and (e) for Se 3d and Te 4d, respectively.

Core level study of $FeSe_x$: $FeSe_x$ is stable in the PbO type structure (α-phase) with x up to 8/7 and magnetization measurements indicate that both Fe deficient and Se deficient material are ferromagnetic near room temperature. α-$FeSe_x$ has a planar crystal sublattice consisting of edge sharing $FeSe_4$ tetrahedra, the same as the $FeAs_4$ tetrahedra layers found in oxypnictides [29]. The discovery of superconductivity in $FeSe_4$ is valuable in understanding the superconducting mechanism of Fe-based superconductors. Furthermore, $FeSe_x$ is much easier to handle and fabricate since it is a binary system and selenium is much less toxic than arsenic. Investigation of the superconductivity in $FeSe_x$ can shed light on the role of FeAs layers and magnetic interaction related with the occurrence of superconductivity in the recently discovered superconducting ferrous-oxypnictides.

Figure 5.15 (a) shows the core level comparison of the $FeSe_x$ system with x = 0.92, 0.99 and 1.04. For all three dopings, the strong Se 3d level has been observed. Similarly, Fe 3p and Fe 3d level near E_F are visible. Se deficiency provides carriers in this system. The zoom of Se 3d levels is shown in Fig. 5.15(b). A small peak shift can be seen, which is negligible because the change of carrier (the deficiency of the Se concentration) is less than 10 %, and it is coupled with the resolution of the measurement.

Fermi surface study of $FeSe_x$: A plot of Fermi surface is shown in Fig. 5.15 (c) for $FeSe_{0.99}$. The hole like Fermi surface at the Γ point (zone centre) and the electron like Fermi surface at the M point (zone corner) are observed. In Fig. 5.10(d), a cut

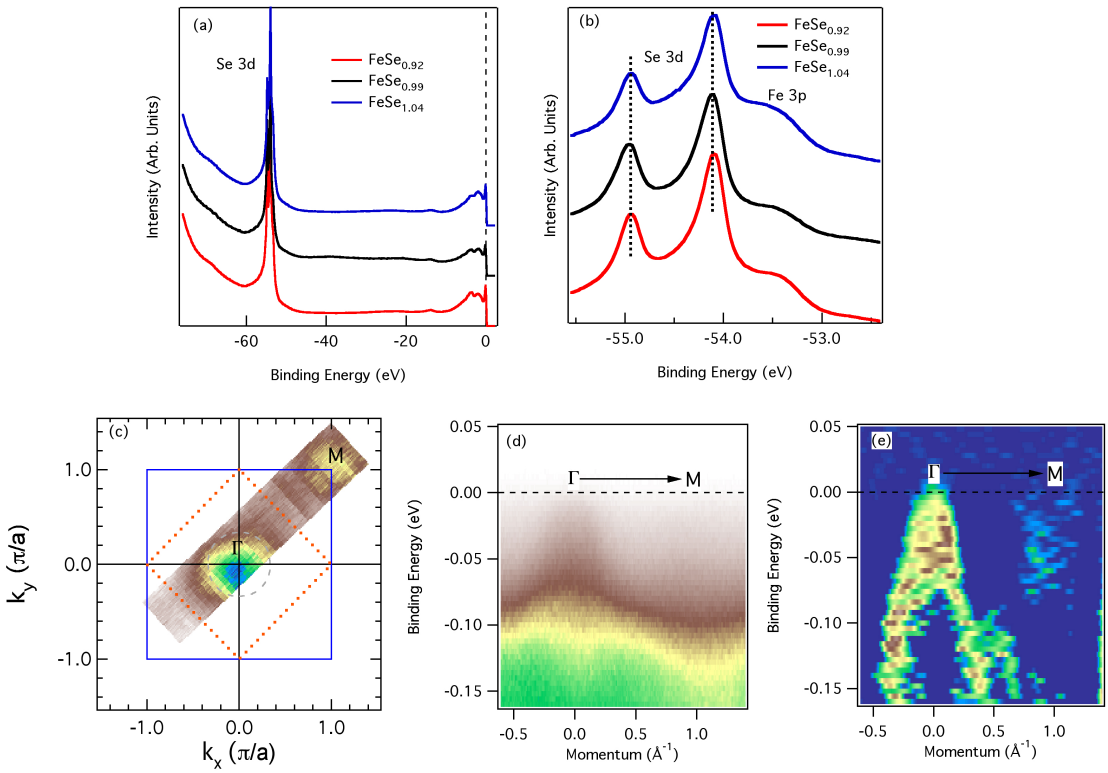

Figure 5.15: (a) Core levels of the $FeSe_x$ system with $x = 0.92$, 0.99 and 1.04. (b) zoom of the Se 3d levels from (a). (c) Fermi surface plot for $FeSe_{0.99}$. (d) ARPES intensity plot of a cut at Γ and along the Γ-M direction, and (e) its 2^{nd} derivative intensity plot for $FeSe_{0.99}$.

at the Γ point along the Γ -M direction is plotted. The intensity near the Fermi level (E_F) is weak. The 2^{nd} derivative intensity plot is shown in Fig. 5.15(d), where a hole band is seen clearly.

Bibliography

[1] M. Neupane *et al.,* arXiv:1005.2966.

[2] I. I. Mazin *et al.,* Phys. Rev. Lett. **101**, 057003 (2008).

[3] K. Kuroki *et al.,* Phys. Rev. Lett. **101**, 087004 (2008).

[4] F. Wang *et al.,* Phys. Rev. Lett. **102**, 047005 (2009).

[5] K. Seo *et al.,* Phys. Rev. Lett. **101**, 206404 (2008).

[6] V. Cvetkovic *et al.,* Europhys. Lett. **85**, 37002 (2009).

[7] H. Ding *et al.,* Europhys. Lett. **83**, 47001 (2008).

[8] A. D. Christianson *et al.,* Nature (London) **456**, 930 (2008).

[9] Y. Sekiba *et al.,* New J. Phys. **11**, 025020 (2009).

[10] K. Terashima *et al.,* P. Natl. Acad. Sci., USA **106**, 7330 (2009).

[11] P. Richard *et al.,* Phys. Rev. Lett. **102**, 047003 (2009).

[12] K. Nakayama *et al.,* Europhys. Lett. **85**, 67002 (2009).

[13] T. Sato *et al.,* Phys. Rev. Lett. **103**, 047002 (2009).

[14] A. Cho, Science **327**, 1320 (2010).

[15] G. F. Chen *et al.,* Phys. Rev. B **78**, 224512 (2008).

[16] K. Maiti *et al.,* Phys. Rev. B **80**, 165132 (2009).

[17] H. Yagi *et al.,* Phys. Rev. B **73**, 172503 (2006).

[18] N. Harima *et al.,* Phys. Rev. B **67**, 172501 (2003).

[19] S. de Jong *et al.,* Phys. Rev. B **79**, 115125 (2009).

[20] H. Ding *et al.,* arXiv:0812.0534.

[21] H. Wadati *et al.,* Phys. Rev. Lett. **105**, 157004 (2010).

[22] S. Hüfner, *Photoelectron Spectroscopy* (Springer-Verlag, Berlin, 1995).

[23] M. Rotter *et al.,* Angew. Chem. Int. Ed. **47**, 7947 (2008).

[24] D. K. Pratt *et al.,* Phys. Rev. Lett. **103**, 087001 (2009).

[25] G. Xu *et al.,* Europhys. Lett. **84**, 67015 (2008).

[26] G. T. Wang *et al.,* Phys. Rev. Lett. **104**, 047002 (2010).

[27] P. Richard *et al.,* Phys. Rev. Lett. **104**, 137001 (2010).

[28] J. G. Analytis *et al.,* arXiv:1002.1304.

[29] F. C. Hsu *et al.,* Proc. Natl. Acad. Sci. U.S.A. **105**, 14262 (2008).

[30] M. H. Fang *et al.,* Phys. Rev. B **78**, (2008).

[31] Y. Mizuguchi *et al.,* Apl. Phys. Lett. **93**, 152505 (2008).

[32] G. F. Chen *et al.,* Phys. Rev. B **79**, 140509(R) (2009).

[33] C. Xu and S. Sachdev, Nature Phys. **4**, 898 (2008).